SUSPENDED GALLIUM PHOSPHIDE THIN FILM PLATFORM FOR NONLINEAR PHOTONICS AND OPTOMECHANICS

WANG YIFAN

PhD

The Hong Kong Polytechnic University

2026

The Hong Kong Polytechnic University

Department of Applied Physics

Suspended Gallium Phosphide Thin Film Platform for Nonlinear Photonics and Optomechanics

WANG Yifan

A thesis submitted in partial fulfilment of the requirements for the degree of Doctor of Philosophy

August 2025

CERTIFICATE OF ORIGINALITY

I hereby declare that this thesis is my own work and that, to the best of my knowledge and belief, it reproduces no material previously published or written, nor material that has been accepted for the award of any other degree or diploma, except where due acknowledgement has been made in the text.

_____(Signed)

WANG Yifan (Name of student)

Abstract

This thesis focuses on the design, fabrication, characterization, and application of high-performance suspended gallium phosphide (GaP) thin-film photonic and acoustic devices, with emphasis on Bound States in the Continuum (BIC) waveguides, nonlinear optical properties, ultrafast all-optical modulation, and GHz photoacoustic vibration modulation.

First, in terms of waveguide design, a hybrid waveguide structure based on a low-refractive index polymer/high-refractive index GaP single-crystal substrate is proposed and realized, which utilizes the BIC principle to realize the complete decoupling of the TM modes from the TE continuum spectrum, thus obtaining zero radiation loss in the continuum spectrum band. Theoretical and finite element simulation analyses show that by precisely controlling the waveguide geometrical parameters (especially the width), phase-canceling interference can be achieved in both straight and curved waveguides with significant suppression of propagation loss and high fabrication tolerance. The method avoids direct etching of brittle or expensive single-crystal materials, expanding the freedom of material and structure design.

In terms of materials and processes, GaP/AlGaInP/GaAs trilayer structures were epitaxially grown on GaAs substrates by metal organic chemical vapor deposition (MOCVD), and suspended GaP films were prepared by removing the sacrificial layer using wet etching. The thickness uniformity and low surface roughness of the films were confirmed by atomic force microscopy (AFM) and

scanning electron microscopy (SEM). Combining photolithography and inductively coupled plasma (ICP) etching, suspended waveguide arrays were successfully constructed. Process optimization shows that precise control of etching rate and morphology can be achieved while maintaining sidewall perpendicularity and low roughness.

In terms of waveguide propagation performance, the propagation losses of BIC waveguides with different widths were measured at 1550 nm and 775 nm wavelengths, respectively. The results show that the experiments and simulations are highly consistent with each other in terms of the width-dependent trend, but the experimental values are overall high, which is mainly attributed to the non-ideal factors such as material absorption and sidewall scattering. At 1550 nm, the TM fundamental mode loss is about 24.35 dB/cm; at 775 nm, the loss is reduced to 11.83 dB/cm, reflecting the smaller area of the short-wavelength modes and their lower sensitivity to defects.

In the nonlinear optical research, the third-order nonlinear optical response of GaP in the range of 650-850 nm, including two-photon absorption (TPA) and nonlinear refraction, was systematically measured using the Z-scan technique. The results show that GaP exhibits anti-saturation absorption characteristics and self-focusing effect at 800 nm, and TPA coefficients and nonlinear refractive indices similar to those in the literature are obtained. The theoretical model combines the measured spot size, pulse width and linear absorption coefficient to realize the quantitative fitting of the nonlinear coefficients.

For all-optical modulation, the transient reflectance changes of different suspended GaP device structures (grating, waveguide, homogeneous film, bare

film, and glass substrate film) are compared using femtosecond pump-probe technique. The results show that the grating and waveguide structures achieve up to 2.3% transient reflectance change under 775 nm pumping/600 nm probing, much higher than the bare and glass base films due to field localization and mode modulation effects. All structures exhibit sub-picosecond fast rise and picosecond decay processes, where the slow decay component of the localized structures is significantly attenuated, favoring high-speed modulation applications. Comparative performance analysis shows that the suspended GaP films can achieve a 387 fs response with a 16.4 dB switching ratio without the introduction of a sub-wavelength resonant structure, but there is room for further reduction of the switching energy (509.7 J/m^2), which can be achieved by the introduction of a high-Q resonant cavity or a photonic crystal structure.

In the GHz photoacoustic research, a suspended GaP fishnet membrane structure is proposed and compared with the conventional nanodisk structure in finite element simulations and ultrafast pump-probe experiments. The fishnet membrane consists of a periodic array of circular holes with a thickness of 550 nm and a period of 4 μm. It is found that the fishnet membrane exhibits significantly different vibrational mode distributions and boundary-condition effects in photoacoustic interactions compared to the disc structure, and can support long-lived higher-order singular modes with an order-of-magnitude enhancement of the quality factor (Q) of up to more than 90. This reveals the difference between the behavior of geometrically complementary structures in the photoacoustic and electromagnetic domains, and provides new ideas for the design of high-Q optomechanical devices.

In summary, this thesis systematically investigates suspended GaP thin-film devices in terms of device design principle, fabrication process, linear and nonlinear optical properties, all-optical modulation performance, and photoacoustic vibration modulation. The results not only verify the feasibility of BIC waveguides for low-loss propagation, but also demonstrate the potential of GaP materials in the field of high-speed, low-power all-optical switching and high-Q optomechanical resonators. In the future, the combination of sub-wavelength resonant structure and local field enhancement is expected to further reduce the energy consumption, enhance the modulation depth and device integration, and promote its application in the direction of on-chip optical computing, quantum optics and high-speed optical communication.

List of Publications

1. **Yifan Wang**, Ziyu Pan, Yongxian Yan, YataoYang, Wenhua Zhao, Ning Ding, Xingyu Tang, Pengzhuo Wu, Qiancheng Zhao, and Yi Li, A review of gallium phosphide nanophotonics towards omnipotent nonlinear devices, *Nanophotonics*, 2024, 13(18), 3207–3252.

2. **Yifan Wang**, Ziyu Pan, Yuhang Cai, Yongxian Yan Yatao Yang, Xiang Zhang, Yangyang Yu, Weiren Cheng, Ning Ding, Liang Zhang, Qiancheng Zhao, Liang Guo, Yi Li, Babinet-Inverted GaP Suspended Metasurface Enables Long-lasting Unshifted Gigahertz Hypersonic Waves Generation, *Nano Lett.,* 2025, 25(36), 13468-13475

3. Yatao Yang, **Yifan Wang**, Yongxian Yan, Weiren Cheng, Qiancheng Zhao, and Yi Li, On-Chip Single-Molecule Fluorescence Enhancement via Slotted Gallium Phosphide Nanodisks at Anapole States, *Adv. Opt. Mater.*, 2024, 12(1), 2301444.

4. Pengzhuo Wu, Xingyu Tang, Yatao Yang, **YifanWang**, Yongxian Yan, Ziyu Pan, Xucheng Zhang, Mingjian You, Zhenyu Liu, Changjing Bao, Xingchen Ji, Yi Li, and Qiancheng Zhao, Asymmetric $\chi(2)$-translated optical frequency combs

assistedby avoided mode crossing in concentric ring resonators, *Opt. Express*., 2024 32(19), 32924–32938.

5. Weiren Cheng, Ning Ding, Xucheng Zhang, ZhenyuLiu, Xingyu Tang, Wenfu Lin, **Yifan Wang**, Ziyu Pan, Naiqin Bu, Mingjian You, Xingchen Ji, Yi Li, and Qiancheng Zhao, Characterizing thethermo-optic coefficient of gallium phosphide-on-insulator platform using high-quality ring resonators, *Appl. Phys. Lett.*, 2025 126(16), 1622052025.

6. Weiren Cheng, Zhaoting Geng, Zhuoyu Yu, Yihan Liu, Yatao Yang, Pengzhuo Wu, Houling Ji, Xiaolun Yu, **Yifan Wang**, Changjing Bao, Yi Li, and Qiancheng Zhao, Wafer-scale inverted gallium phosphide-on-insulator rib waveguides for nonlinear photonics, *Opt. Lett.*, 2023, 48(14), 3781–3784.

Acknowledgements

As I write these words, my four-year doctoral journey is nearing its end. Looking back, this journey - filled with sweat, confusion, and growth - has been illuminated by the support of countless individuals. Here, please allow me to express my deepest gratitude to the supervisors, friends, and family who have illuminated my academic and personal paths.

First of all, I would like to express my deepest respect to my two supervisors. I would like to thank Prof. Chai Yang and Prof. Li Yi. It was you who opened up a new world of research for me with your profound knowledge and open international perspective. Prof. Chai provided me with help in my studies and daily life, allowing me to quickly integrate into my doctoral studies. Prof. Li accompanied me through the most difficult stages of my experiments with persistence and dedication. This spirit will always be with me and benefit me for the rest of my life.

Secondly, I would like to thank the fellow people who helped me throughout my doctoral studies. In Prof. Li's group: Dr. Liu Ronghui, Dr. Lin Wenfu, Mr. Yang Yatao, Mr. Pan Ziyu, Mr. Yan Yongxian, Mr. Zhang Xiang, Mr. Zhao Wenhua, Mr. Muhammad Awais, Mr. Fu Wei, Mr. Fan Qingyuan, Mr. Zhu Tao, Mr. Ji Qiang, Ms. Lin Qingqing, Mr. Zhang Xi, Mr. Ma Chenyu, Mr. Hu Yuhang, Mr. Yu Yiming, Mr. Wu Xu, Mr. Zhao Xuyang, Mr. Li Junyao and Mr. Deng Tao. The weekly group meetings have broadened my knowledge of scientific research and allowed me to gain new perspectives and ideas through communication. In

Prof. Chai's group: Dr. Chen Hongye, Dr. Lu Gaofei, Ms. Jiang Bi Yi and Mr. Liu Yulong. They helped me and offered me a lot of advice on life and studies. In Prof. Zhao's group: Mr. Cheng Weiren, Mr. Ding Ning, Mr. Tang Xingyu, Mr. Ji Houling, Mr. Wu Pengzhuo, Mr. Geng Zhaoting, Mr. You Mingjian and Mr. Liu Zhenyu. In Prof. Guo's group: Dr. Zhang Liang, Mr. Cai Yuhang, Mr. He Yi, Ms. Ning Sang and Mr. Zhou Shuo. When I was unfamiliar with the experimental procedures, they provided me with guidance and helped the experiment proceed smoothly. Thank you all for your help and experimental support for my research. Thanks to my cats, Xixi and Jiujiu.

Finally, I would like to thank my dear family. My parents often cared about my life during my doctoral studies and provided me with a solid material foundation. My deepest thanks go to my girlfriend Wang Yueqi, whose patience, love, and belief in me have been the warmest light guiding me through challenges and doubts.

Table of Contents

List of Figures

List of Tables

Chapter 1 Introduction

1.1 Background

Following the technological breakthroughs achieved in silicon and germanium photonic devices, III-V compound semiconductors have gradually emerged as a new frontier in the miniaturization and high integration of photonics.[1]–[9] III-V compounds refer to semiconductors formed by elements from Group III and Group V, which typically exhibit superior optical properties compared to traditional silicon materials. Group V materials include arsenides, phosphides, and nitrides, which can operate efficiently across the visible to near-infrared (NIR) wavelength range. Historically, phosphides have received significantly less research attention compared to arsenides and nitrides, but indium phosphide (InP) is a notable exception due to its direct bandgap, making it critically important for fiber-optic communications. However, in recent years, gallium phosphide (GaP) has gradually attracted increasing research interest. This is primarily due to GaP's unique physical properties and nonlinear optical characteristics, particularly in the field of nanophotonics, where GaP demonstrates exceptional performance.[10]–[19]

Among III-V compound materials, GaP has emerged as the preferred material for nanophotonics applications due to four significant advantages. First, GaP has a refractive index exceeding 3.0 in the visible and near-infrared spectral ranges.[20] This high refractive index enables strong confinement of light at

material interfaces, leading to highly efficient light field localization. GaP's high refractive index contrast not only enhances light field localization but also significantly improves spatial resolution, enabling optical devices to achieve more precise control.

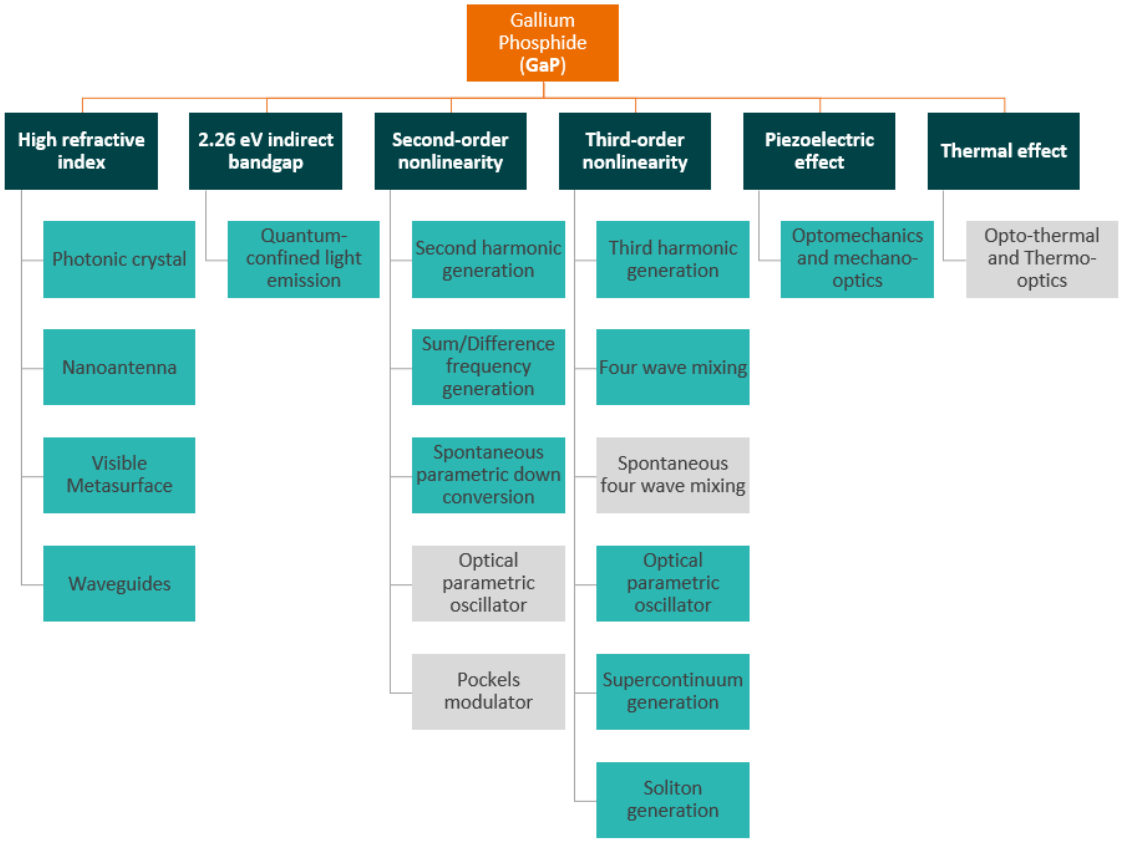

Figure 1.1 Overview of GaP-based nanodevices. The orange, dark green and cyan labels in the figure represent materials, key properties and functional devices, respectively; the gray labels indicate potential but not yet realized functions.

Second, GaP has an indirect bandgap of 2.26 eV in its normal cubic crystal structure.[21] This means it exhibits extremely high transmittance in the wavelength range above blue light, making it suitable for broadband photonic systems and visible light quantum emitters. In the form of small quantum dots

(around 3–4 nm), the strong quantum confinement effect allows GaP to overcome the limitations of its indirect bandgap. This modification enables efficient light emission with quantum yields reaching 35-40%, making it suitable for use in quantum-confined light-emitting applications.[22] Furthermore, GaP serves as an excellent platform for nanophotonics due to its high refractive index and low light loss. It can be used to create nanostructures, such as cavities and antennas, that effectively enhance the emission of other materials, including diamond color centers and two-dimensional layers.[23]–[29] Due to its bandgap characteristics, GaP exhibits a wide range of optical transparency, making it an ideal material for nonlinear frequency conversion processes and highly suitable for optoelectronic integration applications in the visible to near-infrared spectrum.

The third advantage stems from GaP's non-centrosymmetric crystal structure, which endows it with significant second- and third-order nonlinear optical effects. Specifically, GaP's second-order nonlinearity d_{14} is approximately 60 pm/V,[30] while its third-order Kerr nonlinearity is estimated to be up to 200 times higher than that of commonly used silicon nitride (Si_3N_4).

The fourth advantage lies in GaP's lattice constant (5.451 Å), which is highly matched with silicon (5.431 Å). This matching enables low-defect heterointegration with silicon photonic platforms.[31] In contrast, other III-V materials, such as GaAs (5.635 Å) and InP (5.869 Å), exhibit significant lattice mismatch with silicon, leading to increased integration challenges.[32] The high compatibility between GaP and silicon paves the way for scalable hybrid integrated photonic technologies, particularly in the form of GaP-on-insulator (GaP-OI) waveguide systems. Such systems not only retain GaP's nonlinear

advantages but also seamlessly integrate into mature CMOS-compatible photonic process flows, thereby enabling the potential for large-scale manufacturing.

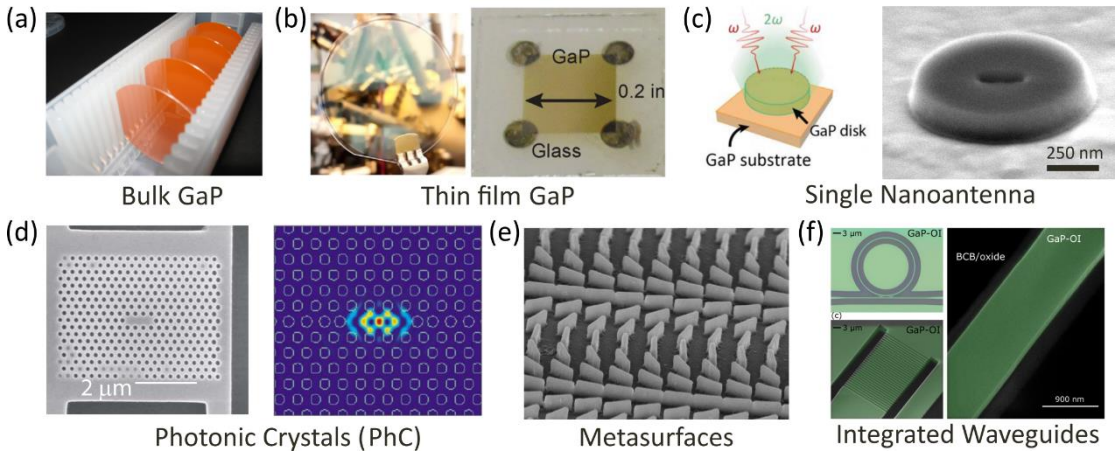

Figure 1.2 Sample devices with different structures (a) Bulk GaP, (b) Thin film GaP[33], (c) Single Nanoantenna[34], (d) Photonic Crystals (PhCs)[35], (e) Metasurface[36], and (f) Integrated Waveguides[12].

Direct monolithic integration on silicon is currently limited by significant lattice mismatch. Conventional methodologies rely on heteroepitaxy of GaP on sacrificial GaAs or AlGaP substrates, followed by subsequent membrane transfer and wafer bonding. By incorporating approximately 2.8% boron content, the BGaP heterostructure achieves precise lattice matching with 12-inch silicon wafers.[37] This approach effectively suppresses interfacial defects and eliminates the need for post-growth transfer, providing a scalable platform for integrated acousto-optics.

In addition to its optical performance advantages, GaP also demonstrates practical advantages in manufacturing. First, the manufacturing cost of GaP is relatively low because its raw materials—gallium and phosphorus—are relatively

easy to obtain and are not as expensive as indium or as toxic as arsenic.[38] Additionally, GaP exhibits high thermal and chemical stability, enabling it to operate reliably under various environmental conditions for extended periods, thereby prolonging device lifespan. These characteristics make GaP not only suitable for nonlinear optical applications but also highly suitable for use in optomechanical modulators and thermo-optic modulators, which rely on changes in thermal refractive index and piezoelectric effects to function.

Table 1.1 Material property of GaP for nanodevices.

Property	Typical values	Year	Reference
Refractive index	2.964 (10 μm), 3.209 (775 nm), 3.590 (500 nm), 5.05 (354 nm)	2016	[20]
Bandgap	2.26 eV (indirect, 300 K)	1996	[39]
Nonlinear index	1.1(3) $\times 10^{-17}$ m^2/W	2020	[40]
Second-order nonlinear susceptibility	d_{14}=60 pm/V	2023	[30]
Waveguide loss	1.2 dB/cm (1550 nm) 6 dB/cm (1550 nm)	2021 2023	[40] [41]
Young's modulus	$Y_o = 10.3\times10^{11}$ dyn/cm^2 (300 K,[100])	1990	[42]
Poisson's ratio	σ_o = 0.31(300 K,[100])	1990	[42]
Piezoelectric coefficient	-0.1 $C\cdot m^{-2}$	1996	[39]
Electro-optic coefficient	-0.97×10^{-12} m/V (623.8 nm)	1968	[43]
Thermal conductivity	1.1 W/(cm·K) (300 K)	1996	[39]
Thermal-optic coefficient	3.4 $\times 10^{-5}$ K^{-1}	2022	[44]

Despite the many advantages of GaP mentioned above, GaP-based

nanodevices are still susceptible to performance degradation under high optical power or prolonged environmental exposure. The main reasons for this include surface oxidation and damage caused by thermal effects, which are particularly prominent in nanostructures with high surface area to volume ratios. To address these challenges, researchers have developed various surface passivation strategies. For example, electrochemical growth of an oxide layer in GaP nanowires can effectively inhibit further oxidation[45], while covering GaP waveguides with a protective silica layer can significantly improve their resistance to environmental damage[46]. At the same time, the researchers also conducted a systematic research on the intensity-dependent third-order nonlinear behavior of GaP to evaluate its damage threshold under high luminous flux. These studies provide valuable design references to ensure the reliable operation of the devices under high power conditions.[47]

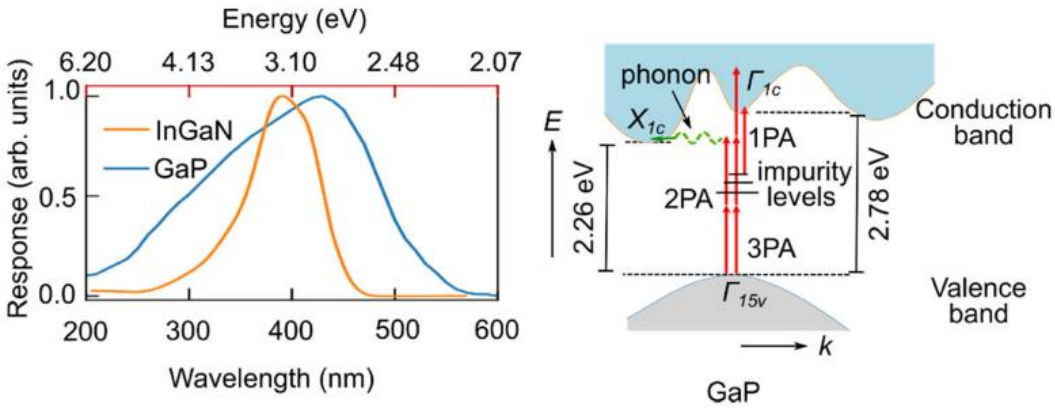

Figure 1.3 Spectral Response and Electronic Structure of GaP. During indirect transition, two-photon absorption (2PA) is required for electron transition from the valence band Γ valley (Γ_{15v} point) to the conduction band X valley (X_{1c} point). The lowest direct jump energy is 2.78 eV, which corresponds to the Γ_{15v} to Γ_{1c}

jump and requires three-photon absorption (3PA). In contrast, impurity energy level electrons located near the band gap can enter the conduction band by single photon absorption (1PA).[21]

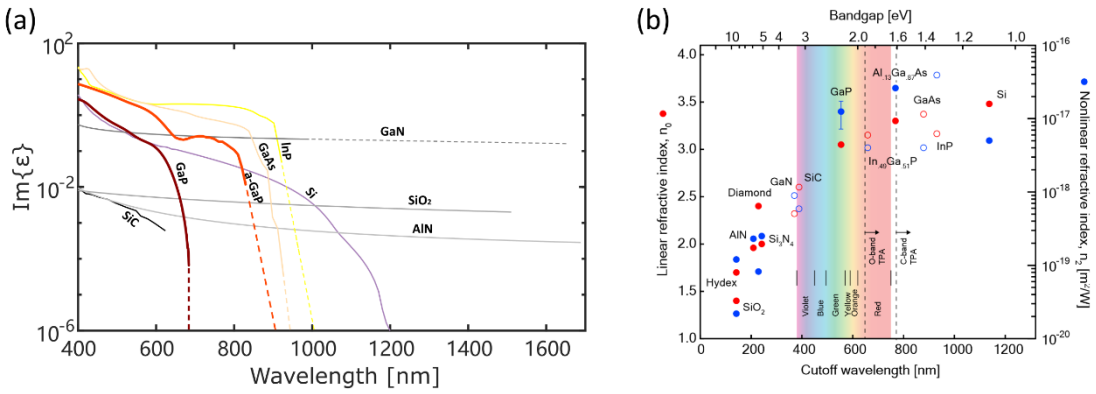

Figure 1.4 Optical losses (**a**) linear and nonlinear indices (**b**) as a function of wavelengths.[40]

The researchers compared the performance of GaP with other materials in terms of optical loss and second-order nonlinearity. As shown in Figure 1.3, the energy band structure of GaP indicates that its indirect band gap of 2.26 eV (corresponding to 548.6 nm) versus its direct band gap of 2.78 eV (corresponding to 446.0 nm) sets two important thresholds for optical absorption. The material loss increases significantly for wavelengths shorter than 446.0 nm, while it decreases sharply for wavelengths longer than 548.6 nm. It is noteworthy that the optical loss of crystalline GaP (c-GaP) is much lower than that of amorphous GaP (a-GaP), which is mainly attributed to the fact that the former possesses a more ordered lattice structure and less defect density.

GaP has a piezoelectric constant e_{14} of about -0.1 C m^{-2}.[39] Typically, GaP

is not considered a piezoelectric material. However, with the advancement of nanoscale studies, GaP exhibits a remarkable piezoelectric response in nanostructures. This new discovery opens the door for its application in opto-mechanical quantum systems, showing great potential in emerging fields such as precision sensing and quantum manipulation.

GaP has a high melting point of 1457 °C, below which it exhibits excellent thermal stability, making it suitable for applications and fabrication in high-temperature environments. At room temperature (about 300 K), GaP has a thermal conductivity of about 110 W/(m K) [39], a value comparable to silicon (130 W/(m K)) but lower than copper or diamond[48]. This indicates that GaP is in the middle of the pack in terms of thermal performance and is suitable for use in electronic and photonic devices.

Table 1.2 Nonlinear optical materials and their optical coefficients at 1550 nm unless stated otherwise*

Material	n_0	Bandgap (eV)	$\chi^{(2)}$ (pm/V)	n_2 ($10^{-18}m^2/W$)	Year	Ref
Si	3.5	1.1	-	4	2003	[49]
$Al_{0.17}Ga_{0.83}As$	3.3	1.63	210	26	2016	[50]
GaP	3.05	2.26	60	11(5)	2020 2023	[40] [30]
Diamond	2.4	5.5	-	0.082	2014	[51]
GaN	2.3	3.4	16	3.4	2011 2018	[52] [53]
Si_3N_4	2	5	-	0.25	2017	[54]
SiO_2	1.45	9	-	0.022	2012	[55]
Doped silica	1.44	0	-	0.022	2008	[56]
AlN	2.12	6.2	4.7	0.23	2013 2012	[57] [58]

4H-SiC	2.6	3.26	11.7 @1064nm	0.6	2023 2019	[59] [60]
Lithium Niobate	2.2	3.78	-27 @1064nm	0.18	2021	[61]
Lithium Tantalate	n_e = 2.123 n_o = 2.117	3.93	-21 @1064nm	0.3 ± 0.06 @e-wave 800nm 0.17 ± 0.03 @o-wave 800nm	2024 2003	[62] [63]
GaAs	3.4	1.42	238 @1533nm	20	1997 2007	[64] [65]
As_2S_3	2.38	2.4	-	2.92	2007	[66]

To facilitate a comprehensive comparison, we have compiled a table of GaP with other prevalent nonlinear optical materials across these metrics in Table 1.2. Notably, GaP exhibits relatively high values for both linear and nonlinear refractive indices as well as a second-order nonlinear coefficient. The unique positioning of GaP in the nanophotonic landscape stems from its synergistic combination of optical, mechanical, and thermal properties. Compared to Silicon (Si), GaP's wider bandgap of 2.26 eV effectively suppresses two-photon absorption (TPA) in the telecom band, enabling stable, high-intensity nonlinear applications such as frequency comb generation. Unlike centrosymmetric materials like Si_3N_4, GaP possesses a strong second-order nonlinearity for efficient frequency conversion. Furthermore, GaP acts as a critical interface for quantum networking, its simultaneous piezoelectricity and high refractive index allow for bidirectional microwave-to-optical conversion with coupling rates significantly exceeding those of $LiNbO_3$ or AlN. From an integration standpoint, GaP is uniquely advantageous due to its near-perfect lattice match with Silicon

(0.37% mismatch), facilitating high-quality monolithic growth on Si substrates. Combined with a thermal conductivity nearly 20 times higher than $LiNbO_3$, GaP ensures robust thermal management for high-density, integrated photonic circuits.

1.2 Linear GaP optical nanodevices

GaP is noted for the refractive index and broad transparency in the visible to infrared wavelength band (0.55-11 μm). This means that it not only enables strong optical field confinement in optical devices, but also covers a wide spectral interval including the visible and near-infrared bands commonly used for communication.[12], [67]–[75] This property makes GaP very attractive for applications such as optical transmission, optical communication and nonlinear optics. However, challenges remain in the actual fabrication process. For example, when the film's composition favors gallium (Ga-rich), the material tends to take on a metallic sheen and results in enhanced absorption in the visible region, while when the film's composition favors phosphorus (P-rich), it tends to take on a darker brown color, suggesting a similarly high optical loss. All these phenomena weaken the performance of the materials for photonics applications. Therefore, how to accurately control the stoichiometric ratio of Ga to P during the fabrication process has become the key to determining the optical properties of GaP films.

1.2.1 High quality GaP films

In recent years, researchers have made significant progress in improving the fabrication process of GaP films. Gao et al. used RF sputtering to deposit GaP films in an argon environment, and subsequent high-temperature annealing to restore the ideal stoichiometric ratio and reduce the absorption loss.[76] In their experiments, they found that the refractive index and extinction coefficient of the films decreased significantly if lower RF power was used in the deposition process, thus increasing the transmittance. However, the ideal state could not be fully achieved by low power deposition alone. Therefore, the team introduced high-temperature annealing to further optimize the film structure and optical properties.

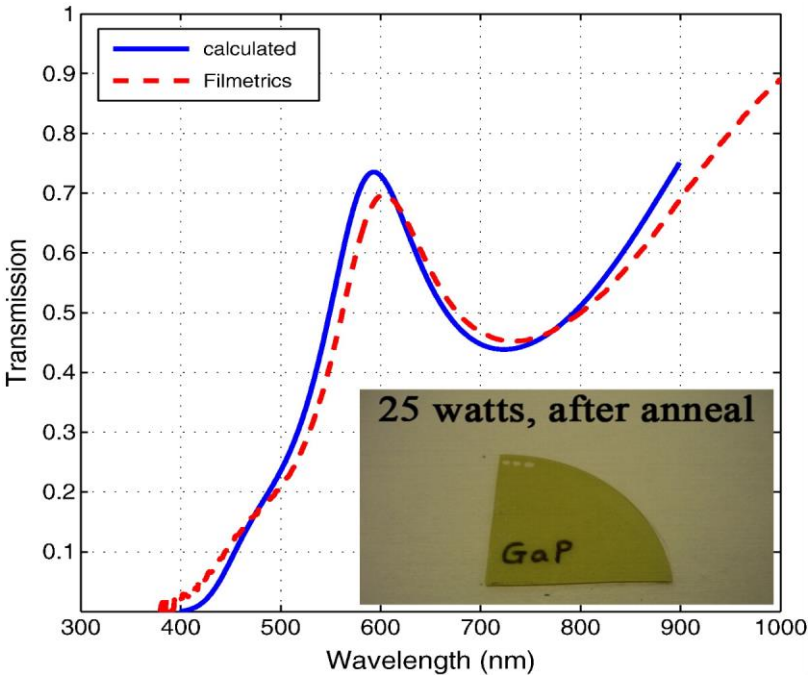

Figure 1.5 Transmission spectra of GaP films prepared by RF magnetron sputtering and subsequent annealing. The blue solid line is the calculated

transmittance based on ellipsometry data, and the red dashed line is the result from a Filmetrics spectrometer, which are in high agreement in the 400-1000 nm band. The inset is a photograph of the GaP film after deposition and annealing at 25 W RF power.[76]

By annealing the films at 700 °C for 30 minutes, they succeeded in obtaining excellent results with a refractive index n = 3.23 and an extinction coefficient k = 0.029 at a wavelength of 633 nm. The experimental sample comprises an 87-nm-thick GaP film deposited on a fused silica substrate. While the lateral dimensions of the sample are macroscopic and do not influence the localized experimental results. This indicates that the optimized GaP film not only has a high refractive index close to that of crystalline GaP, but also has a significantly suppressed absorption in the visible region, which can almost be regarded as a low-loss transparent material. This result lays a solid foundation for the development of future high-performance photonic devices, especially photonic crystals, microcavity resonators, and high-efficiency coupling devices.

1.2.2 Nanodisks and nanoantennas

Fedorov's team utilized molecular beam epitaxy (MBE) in combination with Domain Matching Epitaxy (DME) to directly prepare GaP epitaxial layers of high optical quality on sapphire wafers.[34] The two-step growth process, in which a low-temperature nucleation layer is deposited followed by high-temperature growth, effectively improves the crystal quality and surface flatness of the films. Ellipsometry tests further verified that the refractive indices and absorption

coefficients of these epitaxial layers are highly similar to those of bulk-phase GaP crystals, indicating that their optical properties are capable of supporting low-loss transmission and strong-field localization in the visible range. This achievement is a significant breakthrough from the problems of high roughness and redshift of absorption edges, which are common in conventional RF magnetron sputtered films.

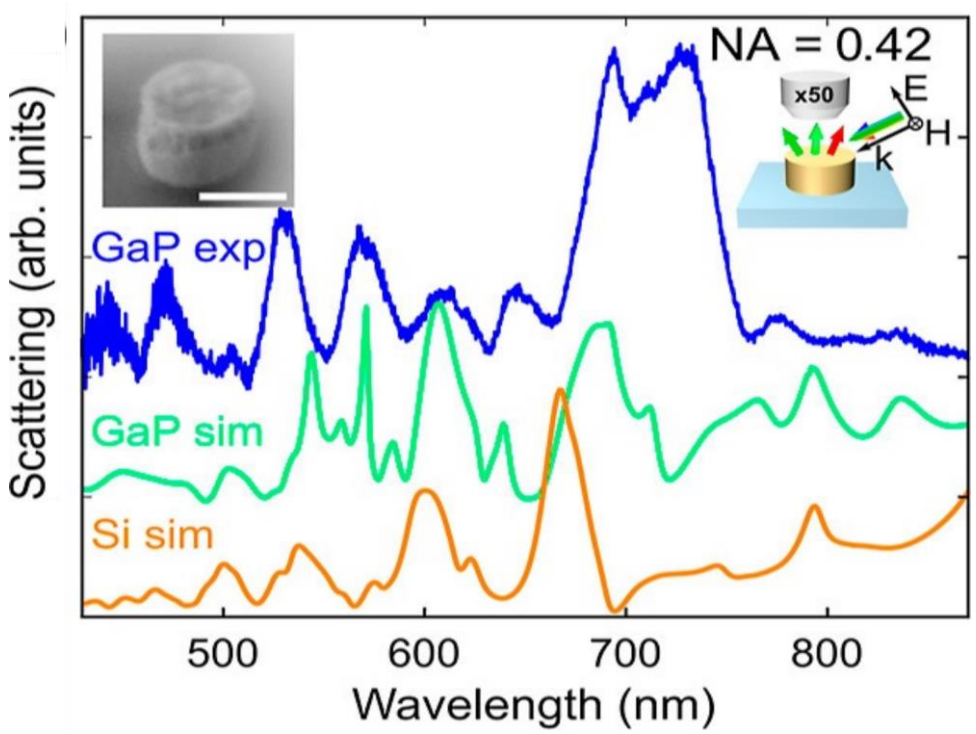

Figure 1.6 Comparison of scattering spectra. The blue curve is the experimental result (GaP exp.), the green curve is the numerical simulation (GaP sim.), and the orange curve is the simulation result (Si sim.) of the silicon nanoantenna. The inset shows the SEM image of the nanoantenna on the top left and the schematic of the experimental configuration (numerical aperture NA = 0.42) on the top right.[34]

As shown in Figure 1.6, when the scattering spectra are compared experimentally (blue curve) and simulated (green curve), it can be seen that the GaP supports both high-order and low-order resonances, while the corresponding silicon nanoantenna (orange curve) exhibits a weaker scattering response. This coexistence of higher-order and lower-order modes makes GaP nanoantennas exhibit unique advantages in enhancing electromagnetic field localization and improving radiation efficiency. In particular, under p-polarized excitation, its near-field electric field is highly concentrated inside the antenna, which enhances the far-field scattering intensity.

Further studies show that GaP nanostructures are not limited to single-particle properties. Light-matter interactions can be significantly enhanced by building dimers and more complex array structures. Rectangular arrays of amorphous GaP (a-GaP) nanodisks were systematically investigated by Hüttenhofer et al.[77] When the array period was tuned to a suitable range (e.g., 400 nm), the collective effect overlapped spectrally with the single-particle resonance, resulting in an increase in absorption of about 300% compared to a single disk.

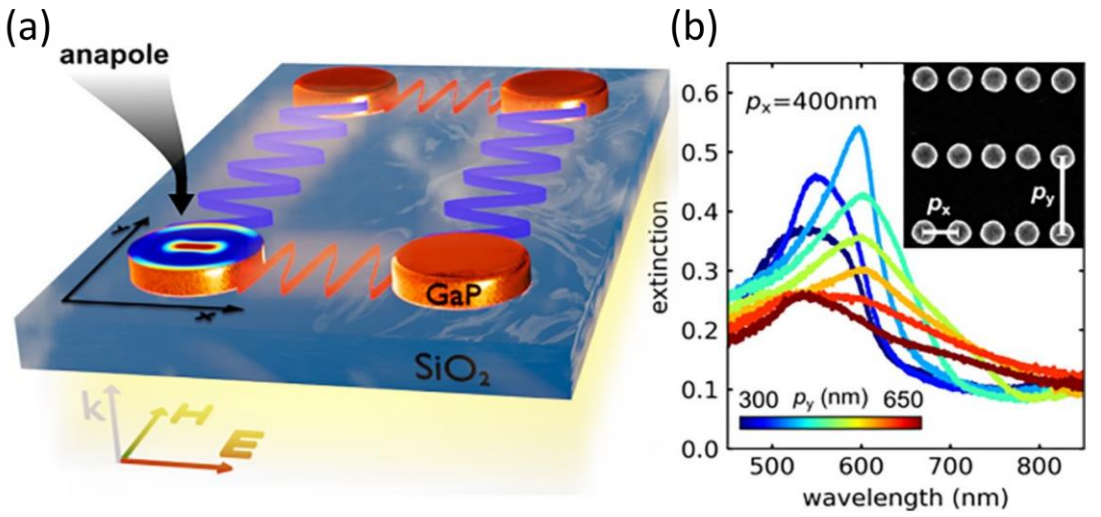

Figure 1.7 Anapole resonance and extinction enhancement mechanism in a two-dimensional array of amorphous GaP nanodisks. (a) Schematic of the coupling mechanism. The anapole modes are excited in individual nanodisks and, through synergistic interactions with the lattice resonances of the arrays, a strong localization of the electric field and a significant enhancement of the absorption are achieved. (b) Experimentally measured extinction spectra. The color of the curve indicates the variation of the array period (p_y) in the y-direction. The inset is an SEM image of a 2D nanodisk array, demonstrating its regular geometrical arrangement.[77]

This phenomenon is illustrated in Figure 1.7, where a two-dimensional array of a-GaP nanodisks on a SiO_2 substrate irradiated by a broadband light source exhibits an orientation-dependent coupling effect. By adjusting the period of the arrays in the x- and y-directions, the researchers found that the enhancement of extinction and absorption is closely linked to the polarization. This array-induced

grating effect and Rayleigh anomaly resulted in a significant amplification of the local electric field and matched the anapole excitation of the single disk in spectral position. Ultimately, such arrays are able to achieve solar absorption efficiencies as high as 34% in the 400-700 nm band (at a thickness of only 50 nm), which is of great interest for photocatalytic and photovoltaic energy conversion applications.

1.2.3 GaP metasurface

In recent years, metasurfaces based on high refractive index semiconductor materials have received much attention in nanophotonics, especially in the visible and near-infrared wavelength bands, and their potentials are mainly reflected in the ability to achieve strong localization and efficient modulation of optical fields.[78]–[84] Among many candidate materials, GaP, with its wide optical transparency window, low intrinsic absorption loss, and mature nanofabrication process, has gradually become one of the key materials to drive the performance improvement of nonlinear and linear optical devices. In particular, by introducing bound states in the continuum (BIC) and their symmetry-breaking derived quasi-BIC, researchers have successfully realized optical resonance with high quality factor, which provides a new means to enhance nonlinear processes.

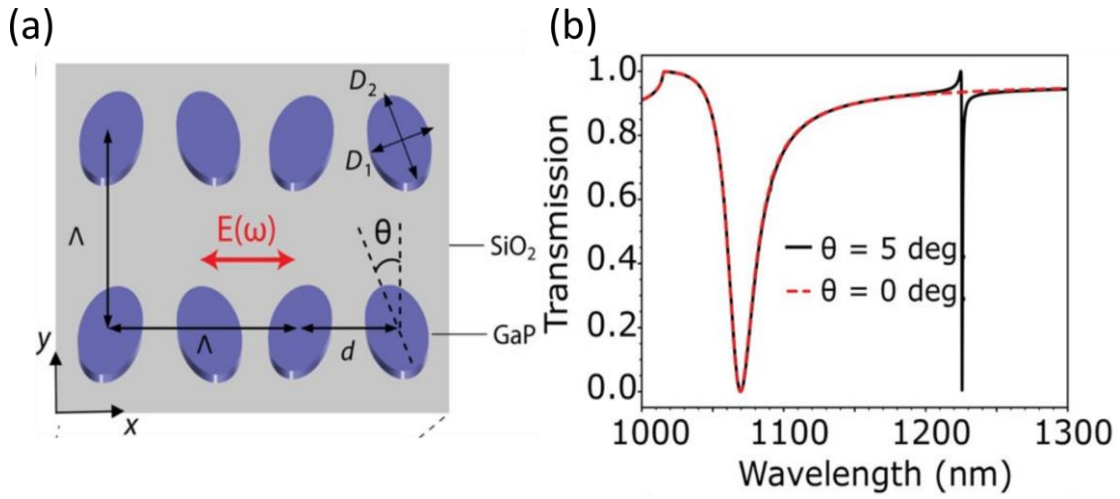

Figure 1.8 Excitation and transmission spectra of quasi-bound states (quasi-BIC) based on GaP dimer metasurfaces. (a) Schematic structure of the dimer array consisting of elliptical cross-section GaP cylinders. Breaking the symmetry by a slight tilt angle θ effectively opens the radiation leakage channel. (b) Simulated transmission spectra show a narrow-band resonance.[85]

Kuznetsov's team made a breakthrough in this direction. They utilized an array of dimer units consisting of elliptical cross-section GaP cylinders as a super-surface platform, and systematically investigated its transmission properties in BIC and quasi-BIC modes.[85] As shown in Figure 1.8, when the dimers are aligned parallel to the main axis, the system supports a quasi-BIC mode with a high quality factor near 1225 nm, and the experimentally extracted *Q*-factor is as high as 4000. The formation of this mode originates from the synergistic effect of the electric quadrupole and magnetic dipole moments, and the introduction of slight asymmetries in the structure (e.g., tilting the ellipses relative to each other with θ = 5°) effectively opens up the radiation leakage

channel to the external incidence wave, allowing the external incidence wave to be separated from the high BIC mode and to be transmitted to the high *Q*-factor. allowing external incident waves to couple to this high *Q* mode. It is this controllable asymmetry that transforms the infinite *Q*-factor of an ideal BIC into a practically excitable quasi-BIC, thus realizing a strong local field enhancement.

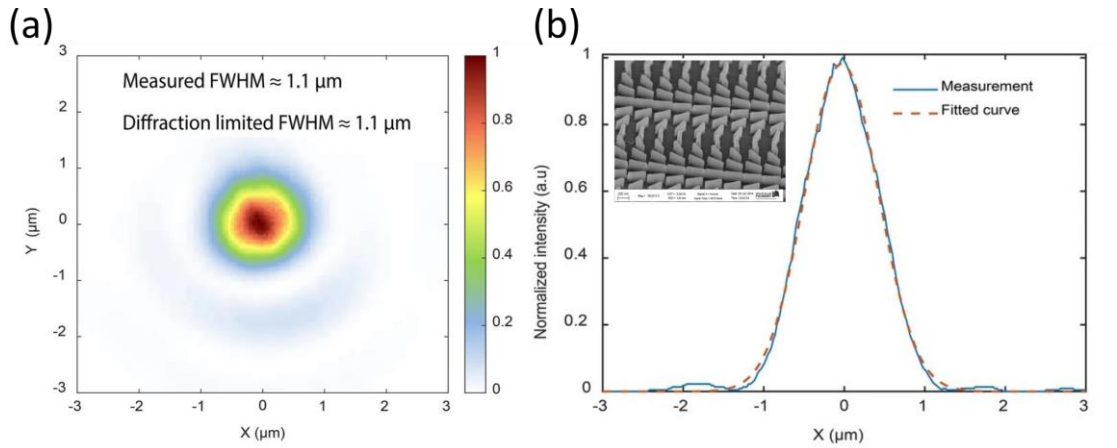

Figure 1.9 Experimental results of visible metal lenses based on GaP films. (a) 2D spot at the focal position measured at 450 nm. (b) Comparison of the normalized intensity at the focal position with the fitted curves. The inset is an SEM image of the lens structure.[12]

Meanwhile, Melli et al. verified the feasibility of GaP films in metal lens design from the perspective of visible light applications.[12] They used RF magnetron sputtering to deposit a-GaP films on transparent substrates (e.g., glass and sapphire), and combined fine electron beam exposure with reactive ion etching to successfully prepare a metal lens. As shown in Figure 1.9, the lens produces a spot close to the diffraction limit at the focal point, and the measured full width at half maximum (FWHM) is about 1.1 μm, which is basically

consistent with the theoretical diffraction limit. This result directly demonstrates that GaP films can not only support high refractive index-guided phase modulation, but also realize high-resolution imaging in practical optical devices.

More importantly, Melli's experiments also show that by optimizing the deposition and annealing conditions of GaP films, the extinction coefficient can be suppressed to almost zero in the 450-800 nm range, which significantly improves the efficiency of the device. This lays the foundation for further improvements in lens diffraction efficiency and imaging quality in the future. Although the measured transmission efficiencies are still lower than the theoretical values, this performance demonstrates the potential of GaP for visible light applications, considering the limitations of the substrate used under high-temperature annealing.

In summary, GaP-based metasurface and nano-optical devices exhibit excellent performance. Its high refractive index, wide transparent window, and low loss inherent properties enable GaP to support diverse optical resonances from low-order electric dipoles to high-order multipolar modes, and thus achieve strong optical field localization and energy conversion efficiency. By introducing symmetry tuning and fine geometrical parameter optimization in the structural design, GaP can effectively excite high-quality factor modes such as quasi-BIC. These results indicate that GaP has great potential in the future development of photonics, especially in metasurface imaging, efficient optical modulation, low-power nonlinear optics, and emerging quantum optics platforms, all of which are expected to play a key role. With the further maturation of the fabrication process and design methodology, GaP will likely become the core material for realizing

the next generation of high-performance photonic devices, driving the development of optical technology towards higher efficiency, smaller scale and wider application areas.

1.2.4 Waveguide and micro-ring resonator

In recent years, GaP-on-insulator (GaP-OI) platforms have emerged as emerging frontier choices in integrated photonics. With its high refractive index, wide transparent window, and excellent nonlinear coefficient, GaP-OI shows great potential in quantum optics, nonlinear optics, and high-sensitivity sensing. However, whether the devices can really be put into practical applications depends largely on the ability to realize extremely low propagation loss at the sub-wavelength scale. Low loss not only implies higher signal fidelity and energy utilization, but also significantly improves the device's utility in communication and quantum information processing, thus becoming a core focus of current research.

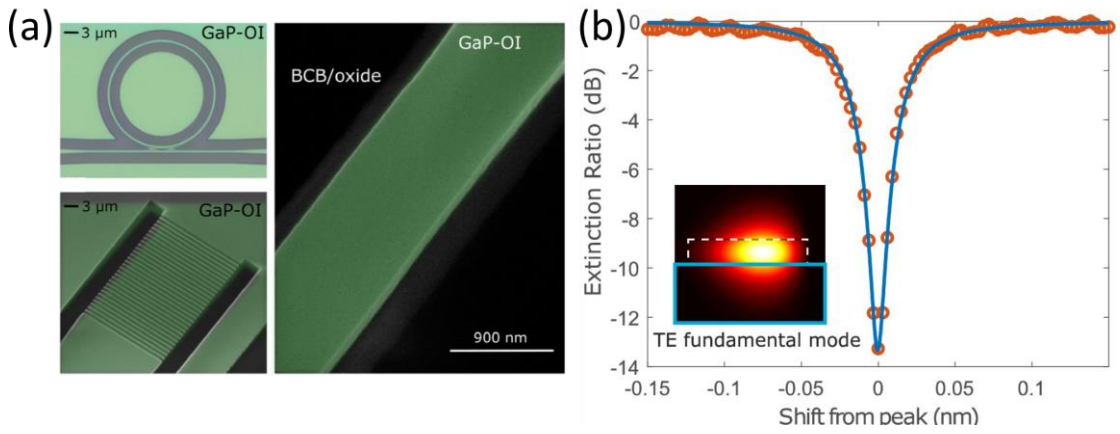

Figure 1.10 SEM image of the GaP-OI platform and its device performance characterization. (a) The fabricated structure of the ring and grating-coupled waveguide. (b) The extinction ratio spectrum of the TE fundamental mode.[41]

In terms of process path, Billet et al. explored micro-transfer printing (μTP) to transfer high-quality GaP films onto insulating substrates to produce highly integrated photonic structures.[41] Compared to conventional wafer bonding, μTP offers significant savings in source material consumption while maintaining high device performance and providing flexibility for compatibility with different substrates as shown in Figure 1.10. The GaP-OI micro-ring resonators prepared in this method achieve an average Q factor of about 35,000, which is not yet the limit of the wafer bonding process, but demonstrates the utility in the construction of waveguides and resonant cavities.

The SEM image shown in Figure 1.10(a) clearly reveals the μTP-processed micro-ring, straight waveguide, and grating-coupled structures, with neat edges, indicating that the interface quality is sufficiently high to support low scattering loss. Further spectroscopic tests show that the devices maintain stable propagation performance in both the visible and near-infrared wavelength bands. This indicates that the μTP process not only provides a scalable fabrication path, but also guarantees the fundamental performance of the devices for optical communication and on-chip photonics applications.

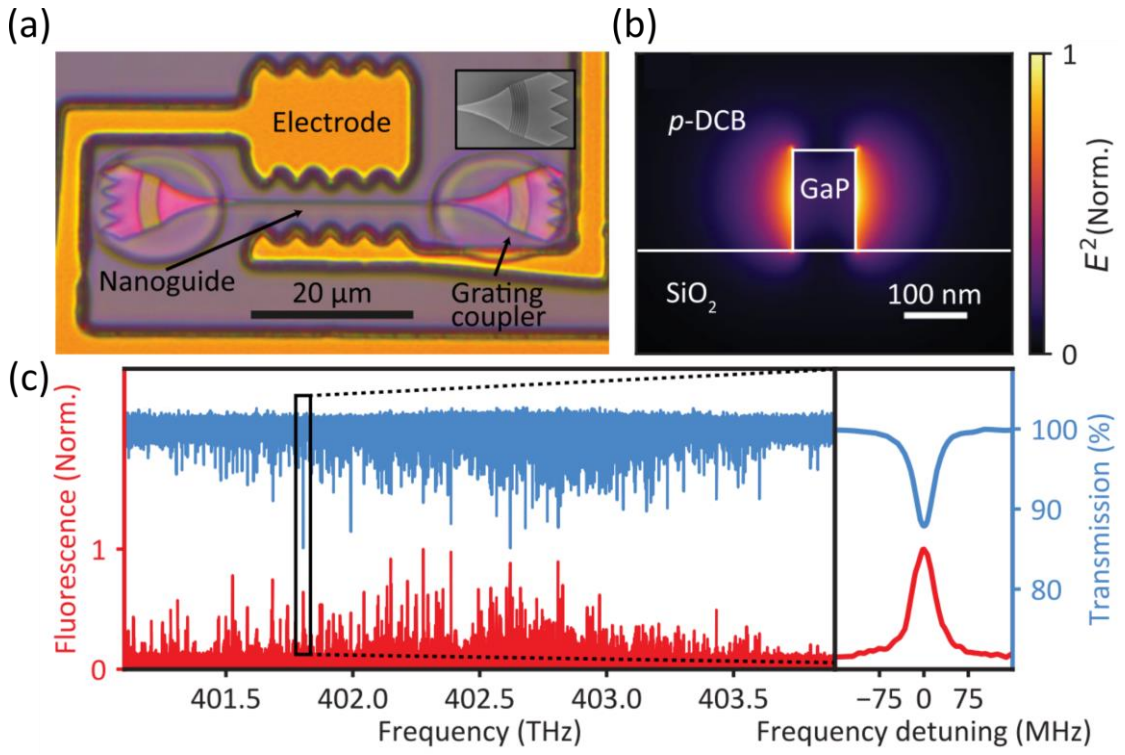

Figure 1.11 GaP nanowaveguide and single-molecule experimental platform. (a) A microscope image of the nanowaveguide. (b) The simulated electric field of the TE mode. (c) Molecular fluorescence and transmission spectra.[86]

In contrast, Shkarin et al. take a different path that is more oriented towards the research of physical mechanisms.[86] They combined GaP waveguides with a single-molecule Stark displacement monitoring technique for direct observation of charge rise and fall at the nanoscale. This approach allowed the researchers to accurately characterize the effect of local charge noise on optical performance in their experiments. By designing a nanowaveguide with a cross-section of about 100 × 160 nm^2 and arranging grating couplers at both ends, they achieved a propagation loss as low as 0.5 dB/cm at 740 nm.

Figure 1.11 shows an optical microscope view of the nanowaveguide and

simulations of the TE-mode electric field distribution, while fluorescence and transmission spectra further reveal the small perturbations caused by charge rise and fall. The research estimates the charge density to be about 2.5×10^{22} m^{-3}. Although this localized noise may lead to a slight drift in the emission spectrum, it does not significantly increase the loss, indicating that the GaP waveguide remains highly reliable while maintaining strong optical confinement.

More importantly, the experiments of Shkarin et al. also reveal that the amplitude of charge rise and fall can be partially controlled by modulating the incident light intensity and electrode structure. This result implies that the GaP-OI platform is not only suitable for low-loss optical transmission, but also serves as an ideal substrate for the integration of quantum emitters with highly sensitive probes. The combination of low loss and local noise controllability gives it outstanding potential for applications in quantum communication and quantum sensing.

For their part, Wilson et al. successfully prepared low-loss GaP-OI micro-ring resonators using a direct wafer bonding process.[40] They achieved a propagation loss of 1.2 dB/cm with a *Q*-factor of more than 10^5 in the telecom C-band test as shown in Figure 1.12. Such a high *Q*-factor not only enables strong localization of the optical field in the cavity, but also ensures a narrow linewidth and high-contrast resonant response, which lays the foundation for further exploration of nonlinear effects and frequency control.

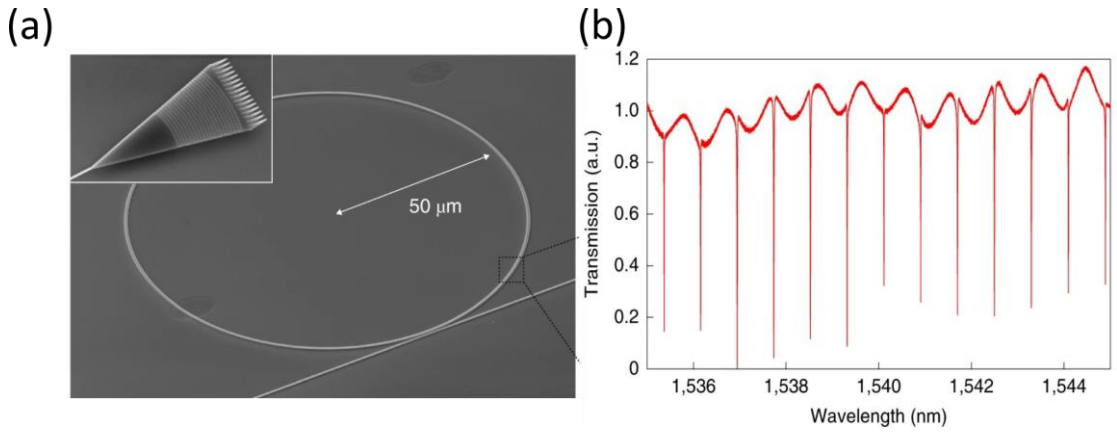

Figure 1.12 GaP-OI micro-ring resonator fabricated using a direct wafer bonding process. (a) The SEM image of the device. (b) The transmission spectrum in the telecom C-band, demonstrating high *Q*-value resonance peaks and low-loss propagation characteristics.[40]

The SEM plots and transmission spectra clearly demonstrate the performance of this high-*Q* micro-ring, with multiple narrow-band resonance peaks successfully observed in the 1536-1544 nm band. This performance highlights the superiority of GaP-OI in the telecom band, allowing it to be seamlessly compatible with existing fiber-optic communication systems while significantly reducing energy loss. It is worth noting that the high performance of this platform is mainly attributed to the low interfacial scattering and material uniformity enhancement brought about by wafer bonding.

In summary, from the flexibility of the μTP process, to the local charge mechanism revealed by single-molecule probes, to the ultra-high *Q* micro-ring realized by wafer bonding, the GaP-OI platform is gradually demonstrating a full range of advantages in low-loss integrated photonics. In the future, with further optimization of process and design, GaP-OI is expected to become a core support

platform to promote high-efficiency photonic integration.

1.3 Second-order nonlinear optical nanodevices

1.3.1 Second-harmonic generation

SHG (second harmonic generation) is a coherent nonlinear process that converts two photons of frequency ω into one photon of frequency 2ω. At the macroscopic scale, SHG as a second-order process requires a non-centrosymmetric crystal symmetry of the excited structure to produce a non-zero SHG signal. In nonlinear optics research, the selection of materials and the design of structures are always the key to determine the performance. Traditional nonlinear crystals such as lithium niobate ($LiNbO_3$) have been used for a long time in the field of frequency conversion, but they often suffer from problems such as limited bandwidth, high loss, or difficult to integrate. With the rapid development of nanofabrication technology, high refractive index semiconductors are becoming candidates for a new generation of nonlinear photonic platforms, especially GaP, which has a wide bandwidth and very low absorption in the visible to near-infrared wavelength bands, and is both capable of supporting strong electromagnetic field localization and highly compatible with CMOS processes. Especially under continuous wave and pulsed conditions, GaP exhibits SHG efficiency in micro- and nanoscale structures that far exceeds that of bulk materials, which makes it an important breakthrough for integrated photonics, quantum information, and the development of new light sources. In recent years, researchers have been pushing the boundary of GaP applications in

nonlinear photonics through different geometrical configurations and material processes, and a series of representative results have emerged, providing a solid experimental and theoretical foundation for understanding and utilizing the nonlinear properties of GaP.

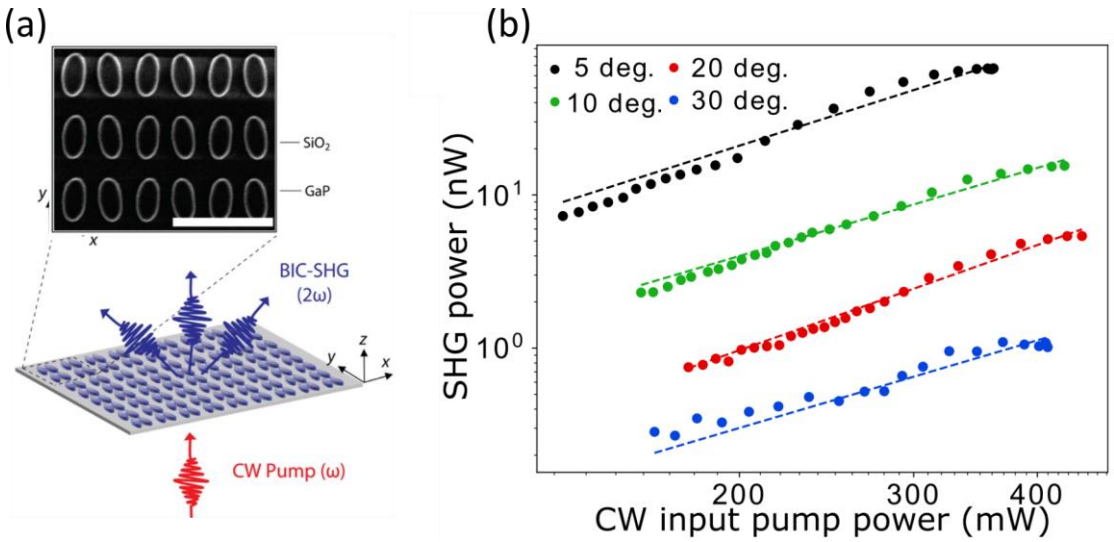

Figure 1.13 GaP quasi-BIC metasurface. (a) Schematic structure and SEM image of the metasurface, consisting of elliptical nanopillar pairs (dimers). (b) SHG power versus input power at 1225 nm continuous wave pumping.[85]

The research of Anthur et al. focused on significantly improving the SHG efficiency by constructing quasi-BIC.[85] They designed a two-dimensional periodic metasurface consisting of GaP elliptical nanopillar pairs (dimers) to achieve a strong localization of the optical field by exploiting a slight symmetry breaking of the geometry. In this design, the main axes of the two elliptical nanopillars are perfectly parallel at $\theta = 0^\circ$, when the system supports an ideal BIC mode, and due to its symmetry, the external light field cannot be effectively coupled into the cavity mode. In order to introduce the coupling channel, they

rotate the elliptical main axes in the structure by $\pm\theta$, which breaks the symmetry and transforms the mode into a quasi-BIC. Numerical simulations show that the structure supports a resonance quality factor of $Q \approx 4000$ at $\theta = 5°$.

Figure 1.13 shows the SEM image and transmission spectrum of the metasurface. The experimental results show that the local electric field is enhanced by more than 50 times and the intensity is enhanced by more than 2500 times under continuous wave pumping at $\lambda \approx 1225$ nm. This extremely high field enhancement enables a SHG conversion efficiency of about 5×10^{-5} W^{-1} to be obtained at low pumping intensity (1 kW/cm^2). Further experiments also show that under pulsed excitation conditions, the SHG efficiency of this metasurface is as high as 0.1% W^{-1}, which is two orders of magnitude higher than that of previously reported dielectric metasurfaces. Notably, this paper takes into account the crystal orientation of GaP during the optimization process to take full advantage of its d_{36} nonlinear tensor element. Through electron beam exposure and reactive ion etching, the team achieved high-quality nanostructures, making the experimentally measured spectra highly consistent with numerical simulations.

Logan et al. reported a GaP-on-oxide-based micro-ring resonator that realizes efficient SHG.[67] A dual resonance design with a quasi-phase matching mechanism is used to obtain conversion efficiencies of up to 400% W^{-1} in an on-chip structure. The team prepared a 427 nm-thick GaP film on a GaP-on-oxide platform, utilizing the rotational symmetry of the micro-ring structure to support TE mode (fundamental) and TM mode (second harmonic). Through numerical simulations, they chose the geometrical parameters of the ring width of about 840

nm and radius of about 7.14 μm to satisfy the quasi-phase-matching condition. The experimental devices were designed with independent coupled waveguides to achieve critical coupling to the 1550 nm and 775 nm modes, respectively, to avoid the common undercoupling or overcoupling problems in the shared coupling region, and the SEM images (Figure 1.14) show the finely-machined micro-ring and coupled waveguide structures.

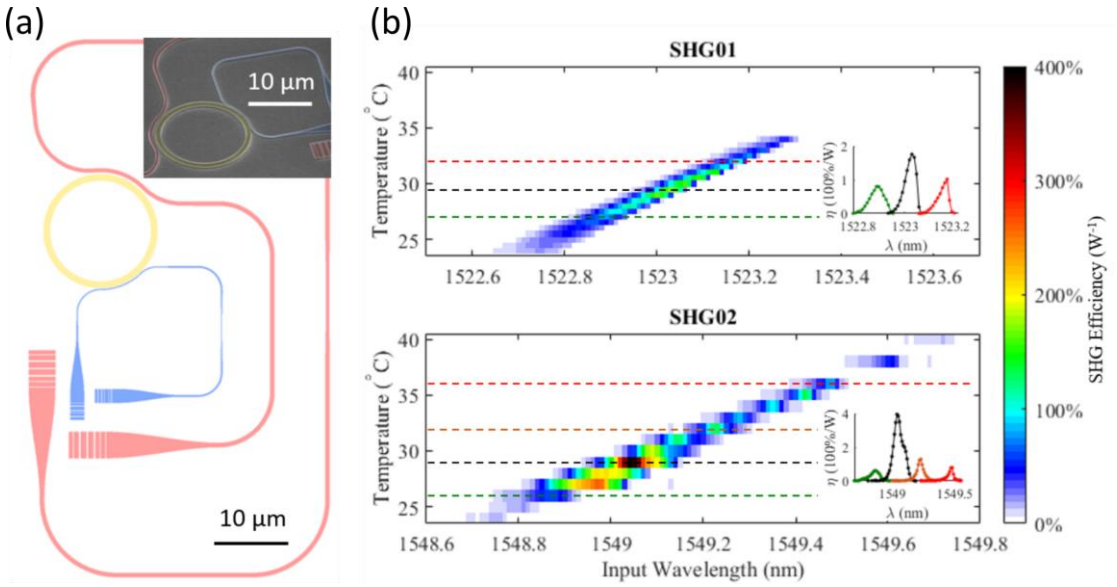

Figure 1.14 GaP-on-oxide micro-ring resonator. (a) Schematic of the chip layout and SEM image of the micro-ring and coupled waveguide with a ring diameter of ~14 μm. (b) Conversion efficiency comparison results, showing SHG efficiencies as high as 400% W^{-1}.[67]

In the experiments, the quality factors of two typical samples (SHG01 and SHG02) reach $Q_1 \approx 26{,}500$ and 40,700, respectively, which correspond to the second harmonic modes Q_2 of about 13,600 and 16,800, and the conversion efficiencies of 400% W^{-1} are achieved at 1550 nm continuous wave pumping,

which are much higher than the levels of the previously reported GaP devices. This finding provides an important direction for the design of more efficient GaP integrated photonic devices in the future.

Tilmann et al. presented the first systematic research of a-GaP thin films based on RF sputtering deposition for second-order nonlinear processes.[13] Unlike conventional epitaxial crystalline films, this method is low-cost, has a low temperature requirement (~250 °C), and is easy to deposit on low-refractive-index substrates (e.g. glass). Spectroscopic ellipsometry results show that a-GaP maintains low-loss transparency in the $\lambda > 650$ nm range, and its real refractive index is very similar to that of c-GaP, reaching $n \approx 3$. XRD measurements show that a-GaP samples do not possess obvious crystal diffraction peaks, verifying its amorphous structure. In the SHG experiments, the team used laser pumping at $\lambda = 1120$ nm and found that the amorphous films still exhibited a sizable second-harmonic response that was close to the level of c-GaP films as shown in Figure 1.15. Even more dramatically, when the films were processed into nanopatches by electron beam exposure and dry etching, the SHG response increased by two orders of magnitude. Numerical simulations show that these nanostructures support anapole-like resonance modes, resulting in very strong local field enhancement. They also observed ultrafast reflectivity modulation of more than 5% accompanied by free-carrier contributions using sub-10 fs pump-detect experiments, demonstrating the potential of a-GaP for ultrafast nonlinear optics applications.

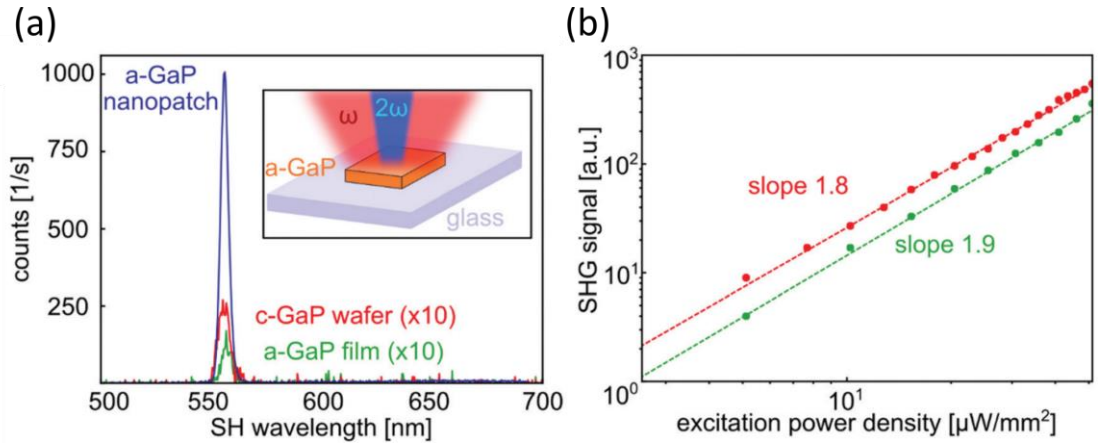

Figure 1.15 Amorphous GaP thin films with nanostructures. (a) SHG spectra under 1120 nm excitation comparing unstructured film, c-GaP and nanopatch. (b) Power dependence curve, the SHG response of the nanopatch is enhanced by two orders compared to the unstructured film.[13]

The work of Pantzas et al. focuses on the fabrication and SHG realization of orientationally patterned GaP (OP-GaP) waveguides.[87] They utilized the MOVPE technique to grow GaP films on GaAs substrates and achieved polarity reversal through direct bonding and selective etching to obtain high-fidelity OP-GaP crystals. The SEM image demonstrates the suspended shallow trench waveguide they prepared as shown in Figure 1.16. This structure achieves a SHG conversion efficiency of 200% W^{-1} with a bandwidth of about 2.67 nm under continuous wave pumping at 1596 nm and 70 mW. The experimental results are in accordance with the theoretically expected squared sinc function, which verifies a high degree of homogeneity of the domain period. In the fabrication process, they used a SiN mask with ICP etching to build the orientation reversal cycle, and then reduced the surface roughness to ~1 nm by chemical-mechanical

polishing. high-resolution transmission electron microscopy images confirmed that the domain boundaries of the OP-GaP were nearly perfectly parallel with a fidelity of more than 95%.

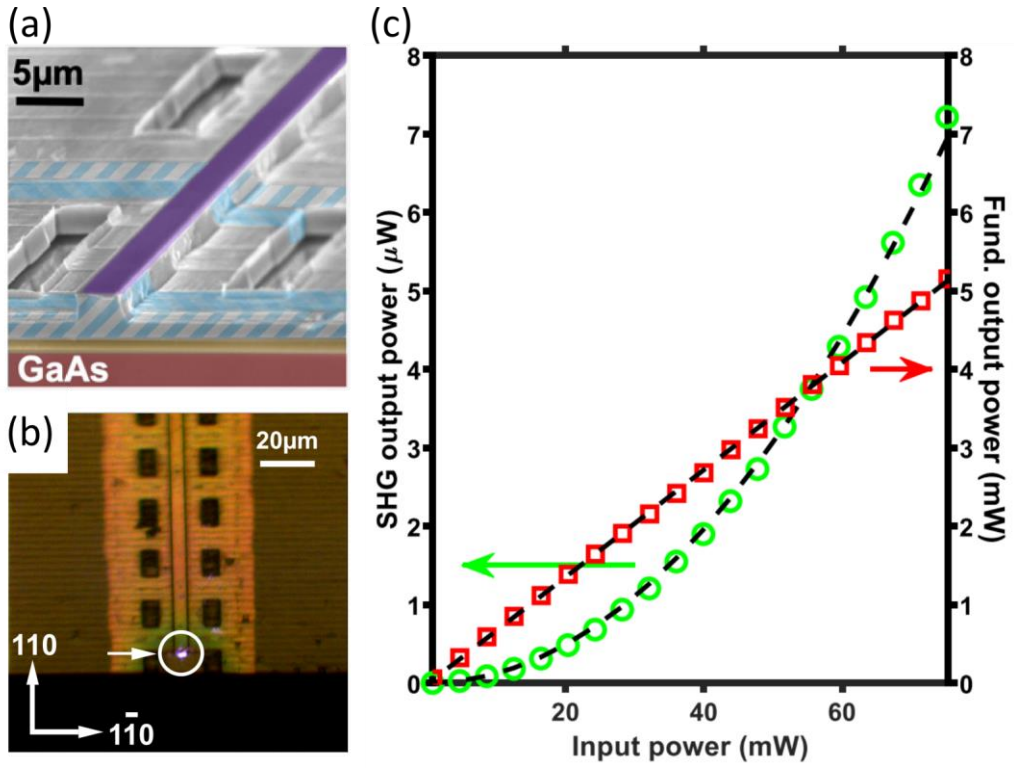

Figure 1.16 Suspended oriented patterned GaP (OP-GaP) waveguide. (a) Aerial SEM view of a suspended shallow trench OP-GaP waveguide. (b) Optical micrograph of the output second harmonic at 1596 nm with 70 mW continuous wave pumping. (c) Measured conversion efficiency versus wavelength curve with a bandwidth of about 2.67 nm and good agreement with the theoretical squared sinc function.[87]

In addition, the team tested the robustness of the device in different polarization states and demonstrated that the waveguide achieves high SHG

efficiency in both Type-I and Type-II configurations. its high thermal conductivity (~110 W $m^{-1}K^{-1}$) allows the waveguide to maintain stable operation at higher input powers, providing an important opportunity for future applications of integrated nonlinearities in the telecom band. The high thermal conductivity enables the waveguide to maintain stable operation at higher input power, providing an important platform for future telecom band integrated nonlinear applications.

From the current experimental progress, the exploration of GaP in the field of nonlinear nanophotonics has gone far beyond the improvement of a single structure or a single process, and has gradually developed into a comprehensive direction that takes into account material fabrication, optical mode engineering and device integration. Whether relying on strong-field enhancement of high-quality factored modes, geometrical design for quasi-phase matching, or the introduction of novel thin films using low-cost processes, researchers have continued to expand the applicability of GaP. These advances have not only set new records in performance metrics, but also gradually resolved key bottlenecks in practical applications, such as efficient frequency conversion under low-power driving conditions, device scalability in communication bands, and compatibility with silicon-based platforms. It is foreseeable that, with the continuous maturation of fabrication technology and design method, GaP will play an increasingly important role in the development of future nonlinear optical devices.

1.3.2 Sum frequency generation

Compared to SHGs, SFGs no longer depend on the identities of the input photons, resulting in more flexibility in polarization freedom and frequency tuning. Especially in sub-wavelength structures, nonlinear effects can be greatly enhanced by structural design, resulting in highly efficient frequency conversion under low power pumping conditions. This not only broadens the output spectral range, but also provides a basis for applications such as multicolor modulation, frequency conversion, and quantum frequency interfacing.

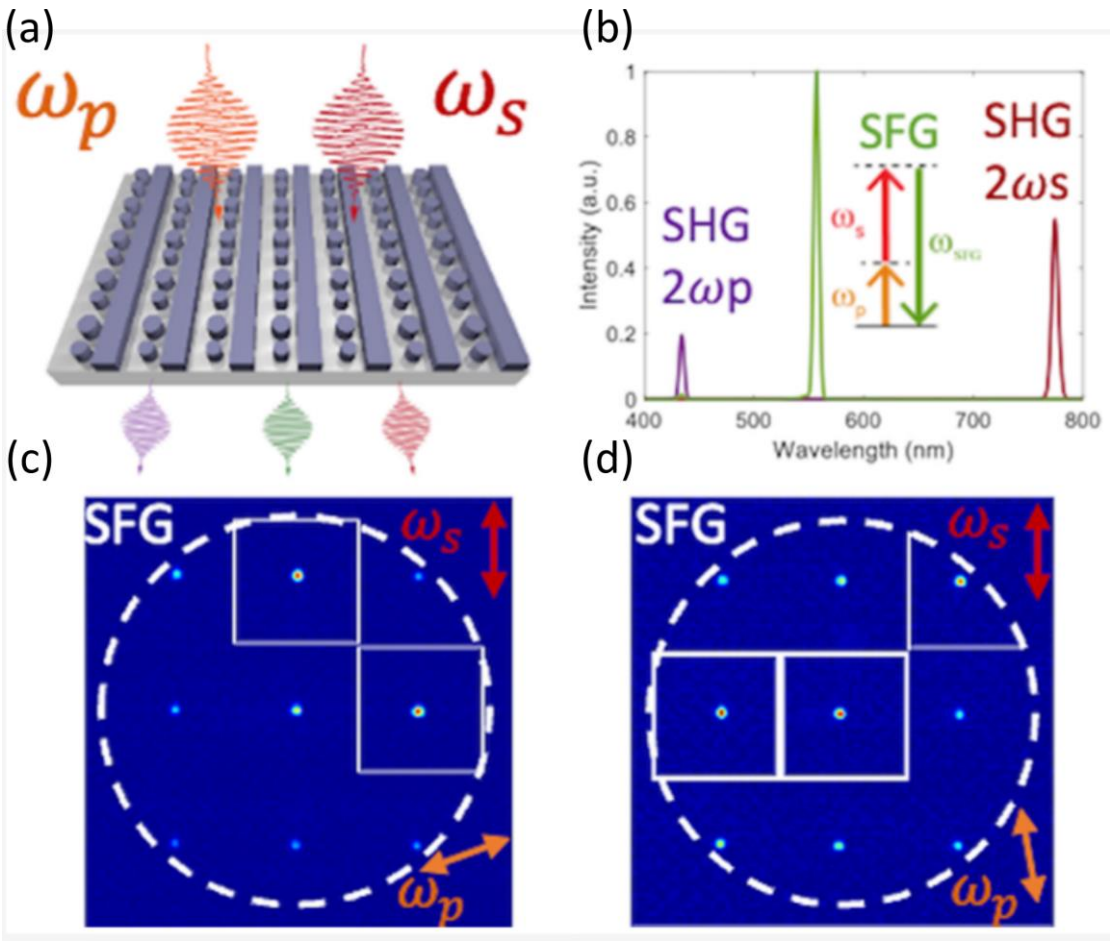

Figure 1.17 Experimental results of efficient SFG based on GaP metasurfaces. (a) Schematic of a GaP nanostructured metasurface with two pumping light

beams of different frequencies. (b) Experimentally obtained output spectra corresponding to the SHG of ω_p, the SHG of ω_s, and the SFG signals of both. Fourier surface imaging under (c) cross-polarization and (d) parallel polarization conditions, verifying the strong dependence of the SFG on the polarization state.[88]

Camacho-Morales et al. successfully realized high-efficiency SFG using a class of GaP metasurfaces supporting leaky-wave BIC.[88] The metasurfaces are composed of periodically aligned GaP nanopillars as shown in Figure 1.17(a), which simultaneously support two high-quality factors (Q~400) modes at the same time. The researchers observed significant SFG signals (~615 nm) under continuous-wave excitation conditions of 1390 nm and 1550 nm for ω_p and ω_s, respectively, as shown in Figure 1.17(b), with conversion efficiencies as high as 2.5×10^{-4} W^{-1}. More significantly, the SFG signal of this metasurface under orthogonally polarized pumping is significantly enhanced, proving its polarization control ability, see Figure 1.17(c)/(d). This property breaks through the limitations of conventional Mie-type structures, which typically rely on low Q modes with more than two orders of magnitude lower conversion efficiency.

In summary, GaP metasurfaces based on high-Q BIC modes provide a powerful technological platform for integrated nonlinear light sources. Not only does it achieve high efficiency SFG, but also further enhances the device tuning freedom through polarization control. This type of structure has great potential for building multi-channel, low-power, and on-chip integrated frequency conversion units, paving the way for photon modulation between the visible and

near-infrared. Future combinations of phase-matching strategies, waveguide coupling, and material optimization are expected to drive the utility of SFGs and other multi-wavelength nonlinear processes in integrated quantum optics and communication systems.

1.3.3 Spontaneous parametric down-conversion

Spontaneous parametric down-conversion (SPDC) is one of the most fundamental and widely used χ^2 nonlinear processes in quantum optics, capable of spontaneously fissioning a high-energy pump photon into a pair of energy-conserving but longer-wavelength signal photons and idler photons. Conventional SPDCs rely on periodically polarized crystals and phase-matched conditions to maintain momentum conservation, but "phase-matched SPDCs" without momentum conservation have also been observed in ultrathin or nanoscale structures, marking a new breakthrough in the controllability of quantum light sources.

Sultanov et al. constructed a simple Fabry-Pérot resonant cavity using a GaP film with a thickness of 400 nm, and achieved continuous regulation from unpolarized entanglement to maximally polarized entangled states by adjusting the polarization of the incident pump light.[89] The laminar reconstruction of the two-photon density matrix clearly demonstrates the significant difference between Re(ρ) and Im(ρ) under different pump polarizations. Figure 1.18(b) shows the photon pair correlation counting under the polarization basis vectors such as H/V, D/A, and so on, and the interferometric pattern is strongly dependent on the polarization of the incident light, which suggests that the entangled state

is highly tunable. Compared with SPDC sources in conventional bulk materials, this polarization dependence provides a new degree of freedom for realizing tunable quantum state modulation, and makes the platform suitable for cutting-edge experimental scenarios such as quantum logic gates and quantum interference.

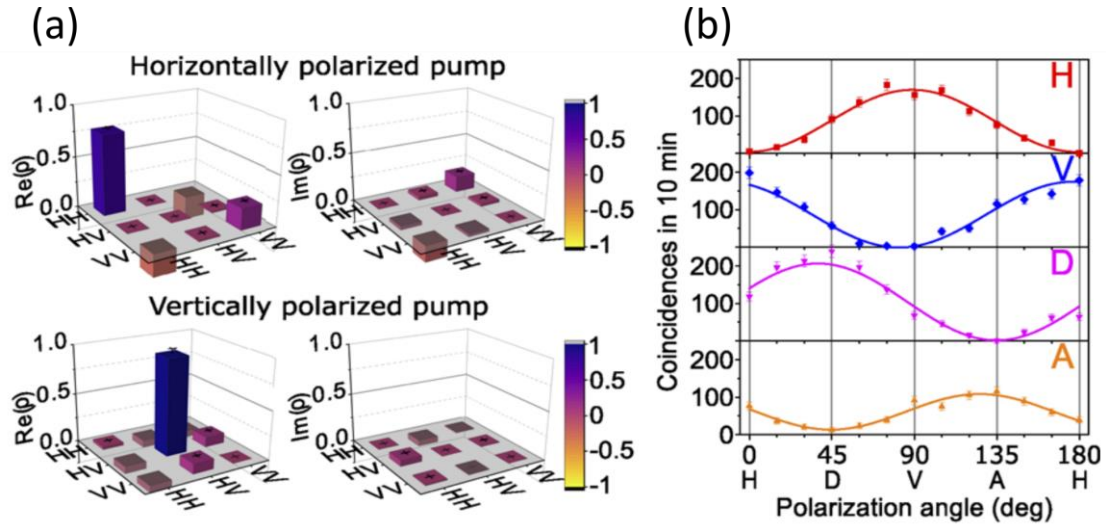

Figure 1.18 Experimental results of polarization-tunable SPDC based on GaP thin films. (a) 3D visualization of the real (Re) and imaginary (Im) parts of the two-photon state density matrix at different pump polarizations. (b) Two-photon correlation counting at different polarization basis vectors, the curves are in accordance with the quantum interference expectation.[89]

Meanwhile, the high-bandwidth property of the thin-film structure is also verified. Due to the thickness of the structure, the intracavity modes have significant frequency selectivity, resulting in an output spectral width of 40 nm at the pump wavelength of 590 nm, which corresponds to an inter-photon time-correlation width of about 12 fs in the Hong-Ou-Mandel (HOM) interferograms,

which is far superior to that of the thick-crystal source. This compression in temporal resolution leads to enhanced interferometric contrast and facilitates the construction of time-energy double entanglement systems. In addition, the structural design does not require periodic polarization or optical waveguide patterning, is easy to fabricate and has high on-chip integration, and provides a practical path for the design of tunable photon sources in quantum chips.

Santiago-Cruz et al. further extend the potential of planar optical structures in the field of quantum light sources by constructing GaP metasurfaces based on quasi-BIC resonances.[90] They used a series of periodically arranged elliptical nanoholes to construct the metasurface structure. These hole arrays are arranged along a one-dimensional period, and by adjusting the direction of the long axis of the ellipses and the period parameter, the suppression of radiative loss is realized, which leads to the induction of quasi-BIC modes with a high Q at specific pumping wavelengths. It is this precise design of structural symmetry breaking that enables the metasurface to simultaneously support two coupled high-quality factor modes, each forming a localized electromagnetic field enhancement at adjacent wavelengths, as shown in Figure 1.19(a).

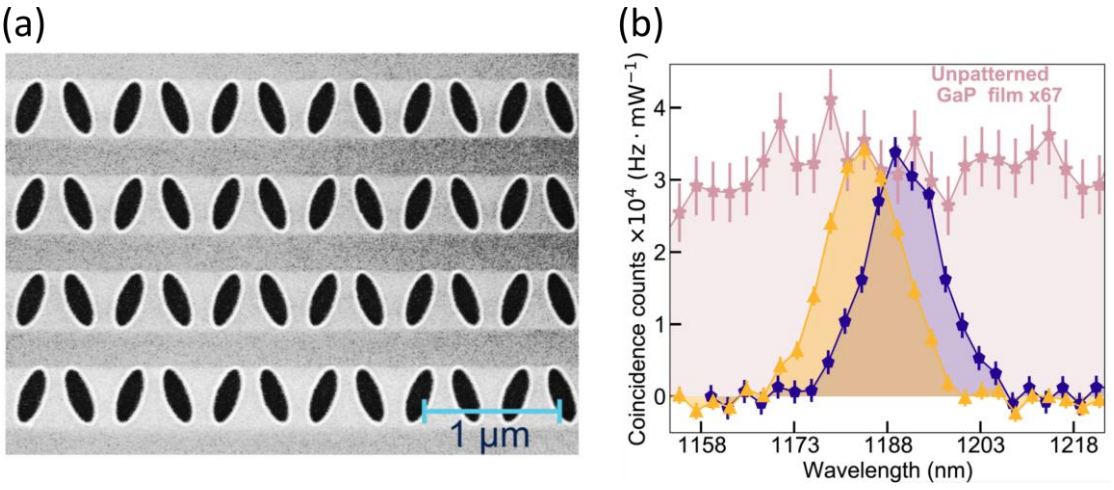

Figure 1.19 Quasi-BIC resonance-enhanced SPDC experiment based on GaP metasurfaces. (a) SEM image showing elliptical nanostructures periodically aligned to form a metasurface with precisely controlled spacing and resonance conditions. (b) Experimentally measured photon pair generation spectra, showing a 67-fold increase in generation efficiency at the resonance wavelength compared to the unstructured film (pink background).[90]

It is worth noting that near the quasi-BIC resonance wavelength (~785 nm), the source strength is dramatically increased due to the significant enhancement of the local field strength, which brings about a jump in the photon pair generation efficiency. As shown in Figure 1.19(b), the photon pair generation efficiency of the quasi-BIC supersurface near the resonance wavelength is improved by a factor of ~67 to an unstructured GaP film.

In addition, the research reveals a unique advantage of the metasurface structure in the spectral domain: the wavelengths of the two photon pairs (signal and idler) each deviate from the quasi-BIC center wavelength by about ±8 nm, suggesting that the resonance coupling excites a bimodal process with complementary frequencies but spatially separated directions. Specifically, the experimental observation that the signal photons are emitted mainly backward while their companion photons are emitted forward reflects the direction-splitting property of non-simple harmonic SPDCs. This spectral-spatial decoupling behavior not only enables efficient collection on-chip, but also helps photon pairs to achieve path-programmable or heterogeneous integration operation in integrated circuits, providing a new dimension for the design of multi-channel

quantum information systems.

In summary, GaP exhibits extraordinary material and structural advantages in the field of SPDC. Its high second-order nonlinear coefficient, low linear absorption, and broadband transparent window enable efficient photon pair generation from the visible to the near-infrared. GaP planar optical platforms exhibit excellent coherence control and on-chip integration potential, whether it is the broadband, tunable polarization entanglement through ultrathin films or the quasi-BIC modes in nanoscale metasurfaces that dramatically enhance the photon pair generation efficiency. In particular, the ultra-compact structure that can maintain strong two-photon correlations without the need for conventional phase matching provides a solid foundation for the construction of high-brightness, low-power on-chip quantum light sources.

1.4 Third-order nonlinear optical nanodevices

1.4.1 Third-harmonic generation

Third-harmonic generation (THG) is an important third-order process in nonlinear optics in which three photons of frequency ω combine to form a new photon of frequency 3ω. This process is widely used in UV source generation, frequency upconversion, nonlinear imaging and construction of quantum light sources. However, realizing efficient THG is often limited by phase-matching conditions. For conventional bulk materials, this challenge requires complex periodic polarization or temperature modulation techniques. However, in micro- and nano-optical structures, the strong localization of the optical field and the

modulation of the structural dispersion allow for the relaxation of the phase-matching conditions, thus making it possible to realize nonlinear processes on more compact platforms.

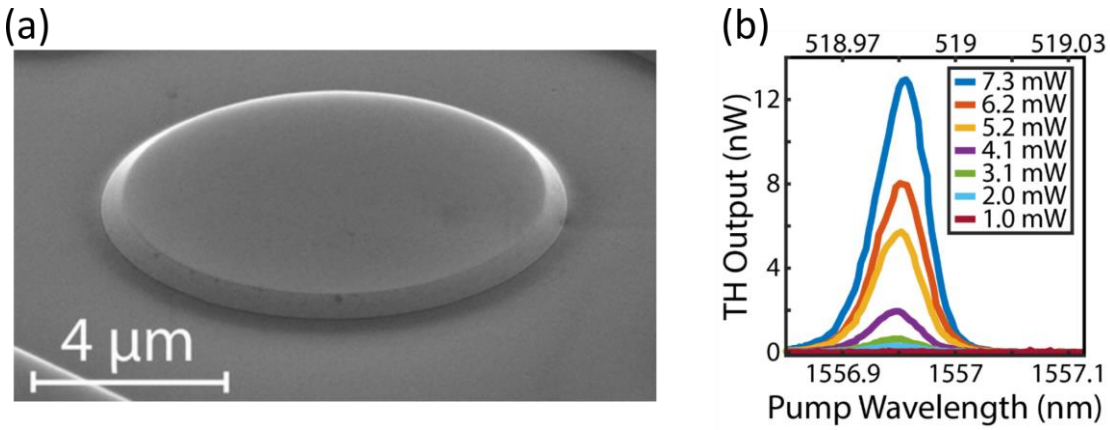

Figure 1.20 (a) SEM of the GaP microdisk structure. (b) Spectral response curves of THG output power versus pump wavelength recorded at different pump powers, with the peak located at ~519 nm.[73]

A systematic research of a-GaP materials by Tillmann et al. reveals that the materials still have significant third-order nonlinear responses in the absence of lattice structure.[73] They constructed GaP disk structures at the micrometer scale and observed significant third-harmonic output at a pump wavelength of about 1557 nm. At pump inputs ranging from 1 mW to 7.3 mW, the THG signal is significantly enhanced with increasing power and shows a clear peak at specific resonance wavelengths, indicating that the optical mode resonance plays a decisive role in the nonlinear enhancement. It is noteworthy that the THG efficiency of GaP still exhibits good power response characteristics despite some material absorption in the green light (~519 nm) region.

Further theoretical and experimental analyses show that the THG signal in

GaP can originate from both the direct third-order process (DTHG) and the cascade sum-frequency process (CSFG) Using power scaling and coupled-mode theory calculations, they found that at low pump powers, the contributions of the two mechanisms are similar, while at high powers, the CSFG process saturates the SH signal due to its energy depletion of the SH modes, which in turn affects the THG efficiency. This mechanism explains why the power response curves of SH and TH signals do not follow a strict quadratic and cubic law under certain conditions.

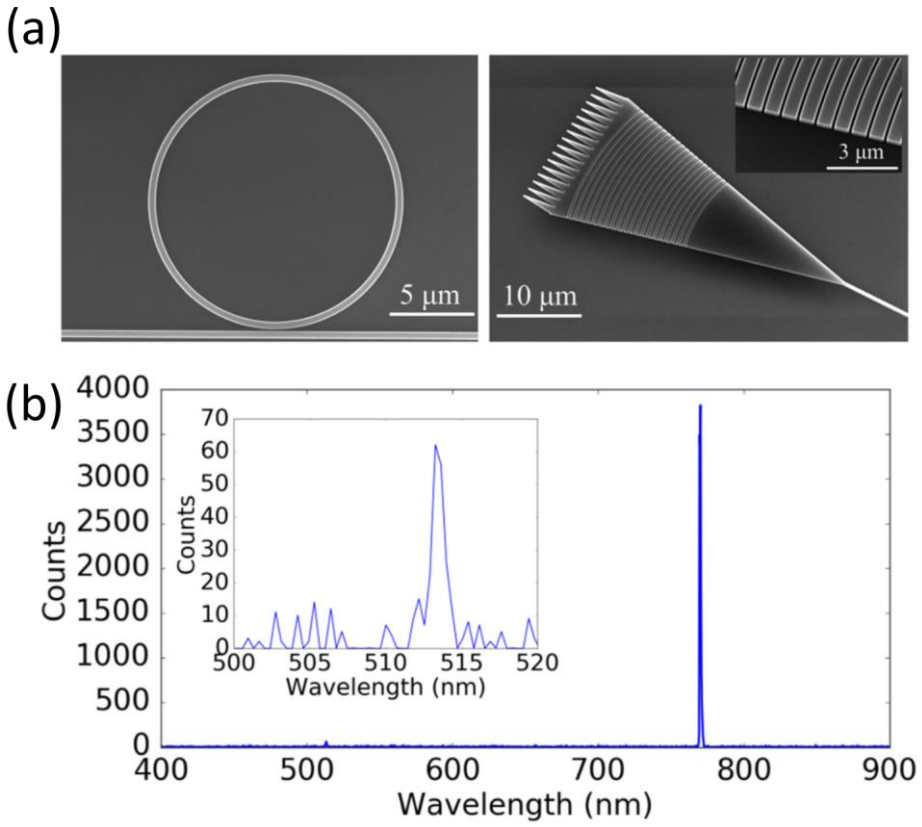

Figure 1.21 (a) Ring resonator structure on GaP-on-SiO_2 platform (left) and its coupling device with a tapered waveguide (right) for the realization of high-Q nonlinear processes, the inset shows a magnified view of the coupled waveguide.

(b) Recorded spectral response curve with a clear third harmonic peak observed at 513 nm, the inset shows its amplified spectral features in the 500-520 nm range.[91]

Schneider et al., on the other hand, realized a photonics integrated device on a GaP-on-SiO_2 platform and demonstrated a ring resonator structure with waveguide excitation (Figure 1.21(a)).[91] The device structure utilizes the coupling between the waveguide and the ring cavity to achieve a quality factor of up to 20000, and the third harmonic output at 513 nm is observed at a pump power of 3.7 mW (Figure 1.21(b)). In contrast, the THG process in this system is mainly limited by the absorption of the material in the visible wavelength band, but effective energy conversion and output are still realized by fine tuning the structural parameters and pumping mode of the device. This integrated structure demonstrates the great potential of GaP on CMOS-compatible photonic platforms, and provides technical support for further integration of multi-order nonlinear devices.

In summary, these studies fully demonstrate the dual advantages of GaP materials in third-harmonic generation: on the one hand, its strong third-order nonlinear intrinsic properties make direct THG possible; on the other hand, its excellent second-order nonlinear response supports the cascade frequency conversion process, which further improves the efficiency. By introducing a high-Q cavity structure and sophisticated modal engineering, the researchers have successfully realized efficient THG outputs in a compact photonic structure. These results not only lay the foundation for the realization of on-chip frequency

converters, but also open up a new path for the construction of multiwavelength integrated quantum light sources.

1.4.2 High harmonic generation

In nonlinear optics, High-Harmonic Generation (HHG) represents one of the most extreme frequency conversion mechanisms, transforming incident mid-infrared light into higher-order harmonics in the visible and even extreme ultraviolet (XUV) bands. This process was originally confined to gases or bulk crystals, but the recent rise of nanophotonic structures has significantly advanced the development of solid-state HHG. In this context, Shcherbakov et al. demonstrated a scheme to realize multi-order high-harmonic emission using ultrathin GaP metasurfaces as a platform, significantly expanding the boundaries of GaP materials for nonlinear applications.[92]

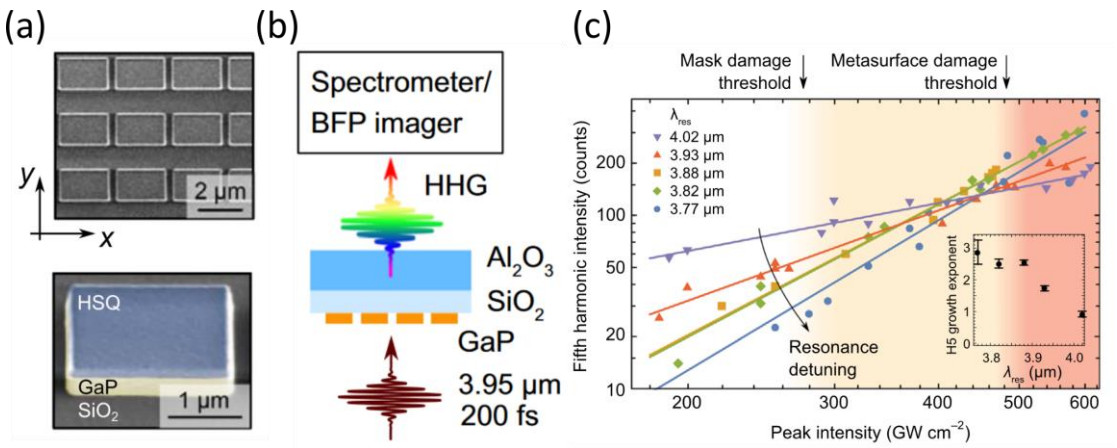

Figure 1.22 (a) Top-view and cross-sectional SEM images of GaP metasurface structures demonstrating periodic rectangular nanopillars. (b) Schematic of the HHG experimental setup. (c) Growth curves of the fifth harmonic intensity with

the peak laser power for different resonance wavelengths λ_{res}, and the inset shows the growth exponent versus λ_{res}.[92]

Figure 1.22(a) shows a SEM of the GaP nanostructure used, where rectangular nanopillars are periodically arranged on a 550 nm thick GaP film to form a dielectric metasurface supporting localized Mie resonance coupled to waveguide modes. The structure is covered with a protective aluminum oxide layer of about 120 nm to prevent laser damage. The laser incidence conditions are shown in Figure 1.22(b), where an intense mid-infrared pulse with a center wavelength of 3.95 μm and a duration of 200 fs is used and focused on the sample in a near-normal direction. The high harmonic signals ranging from the second to the fifth order were successfully detected by back-focal plane (BFP) imaging and spectrometer analysis, and their intensities showed a power-law relationship with the peak intensity of the incident pulse.

Figure 1.22(c) gives the curve of the fifth harmonic (H5) intensity versus the laser intensity. The geometrical parameters of the nanostructures were adjusted to achieve different resonance wavelengths (λ_{res}) in order to explore the effect of resonance detuning on the HHG. The results show that the closer to the resonance ($\lambda_{res} \approx 3.88$ μm), the higher the H5 intensity is and the growth exponent is steeper; when deviating from the resonance, the efficiency of the HHG decreases sharply, indicating that the quasi-resonant modes play a decisive role in the nonlinear enhancement. The inset shows the growth exponent of the fifth harmonic intensity for different λ_{res} conditions, further supporting the conclusion.

1.4.3 All-optical switching using the Kerr effect

The performance of all-optical modulators, as key units for building photonic computing and high-speed information processing systems, is highly dependent on the nonlinear response rate and modulation depth of the material. GaP has become an important material for the research of all-optical switching devices due to its low absorption loss and strong third-order nonlinearity in the visible to near-infrared wavelength band. In particular, driven by the optical Kerr effect (OKE), GaP exhibits femtosecond response times and remarkable transmission/reflection modulation capabilities, making it a candidate for ultrafast photonics applications.

Under intense light pumping, OKE is capable of inducing reversible changes in the optical properties of the material in a very short period of time, thus modulating the propagation behavior of the incident probe light. Grinblat et al. observed in femtosecond pump-probe experiments that GaP films in the 600-1000 nm band, a maximum transmittance modulation close to 70% can be achieved with a modulation duration of less than 30 fs as seen in Figure 1.23.[16] This modulation stems from the synergistic action of OKE and two-photon absorption (TPA), and due to the extremely low linear absorption of GaP in this band, the free-carrier process can be virtually ignored, resulting in modulation bandwidths of up to 20 THz.

Figure 1.23 shows the transient transmittance evolution under two different pumping conditions: (a) with short-wavelength pumping and (b) with long-wavelength pumping. Both show significant negative differential transmission

changes (-Δ*T*/*T*) at delays close to 0 fs, reaching ~60% and 70%, respectively. This very fast and strong response clearly demonstrates the effectiveness of the nonlinear refractive index change and nonlinear absorption mechanism of GaP at different combinations of wavelengths.

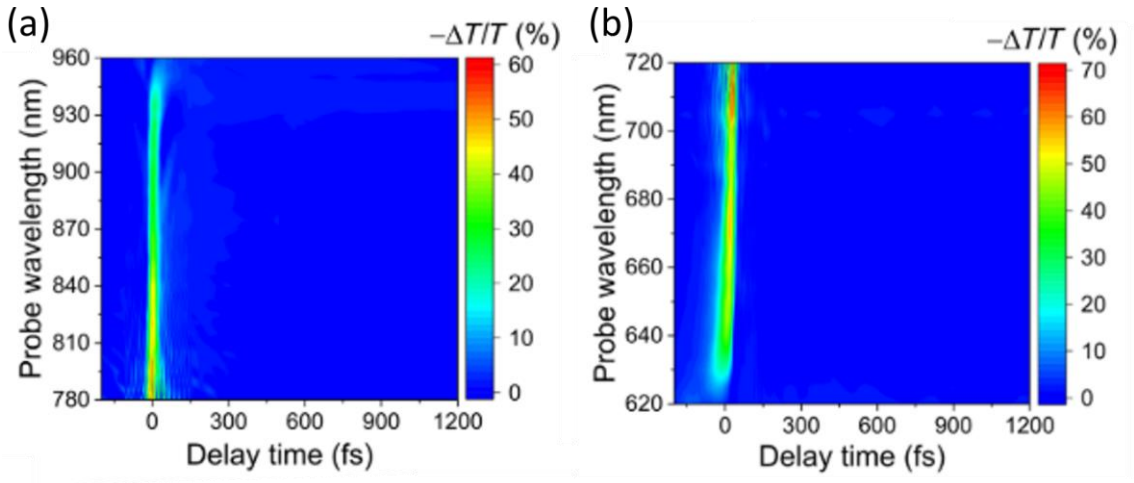

Figure 1.23 All-optical switching in bulk GaP. (a) Pump-detection delay time versus differential transmittance spectrum under short-wave pumping. (b) Differential transmittance spectra under the same conditions with long-wave pumping.[16]

In addition to thin-film structures, Grinblat et al. further investigated the OKE response based on GaP nanodisk structures, demonstrating a strong size dependence as well as modulation properties at sub-20 fs levels.[15] The experiments were carried out using unpolarized axis (anapole) excitation to achieve differential reflectivity (Δ*R*/*R*) modulation in the NIR band by selecting individual GaP nanodisks with different diameters. The SEM images of the nanodisks are shown in Figure 1.24(a), and the transient reflectance spectra of

the samples with different diameters (D = 560, 600, and 640 nm) are demonstrated in (b-d), respectively.

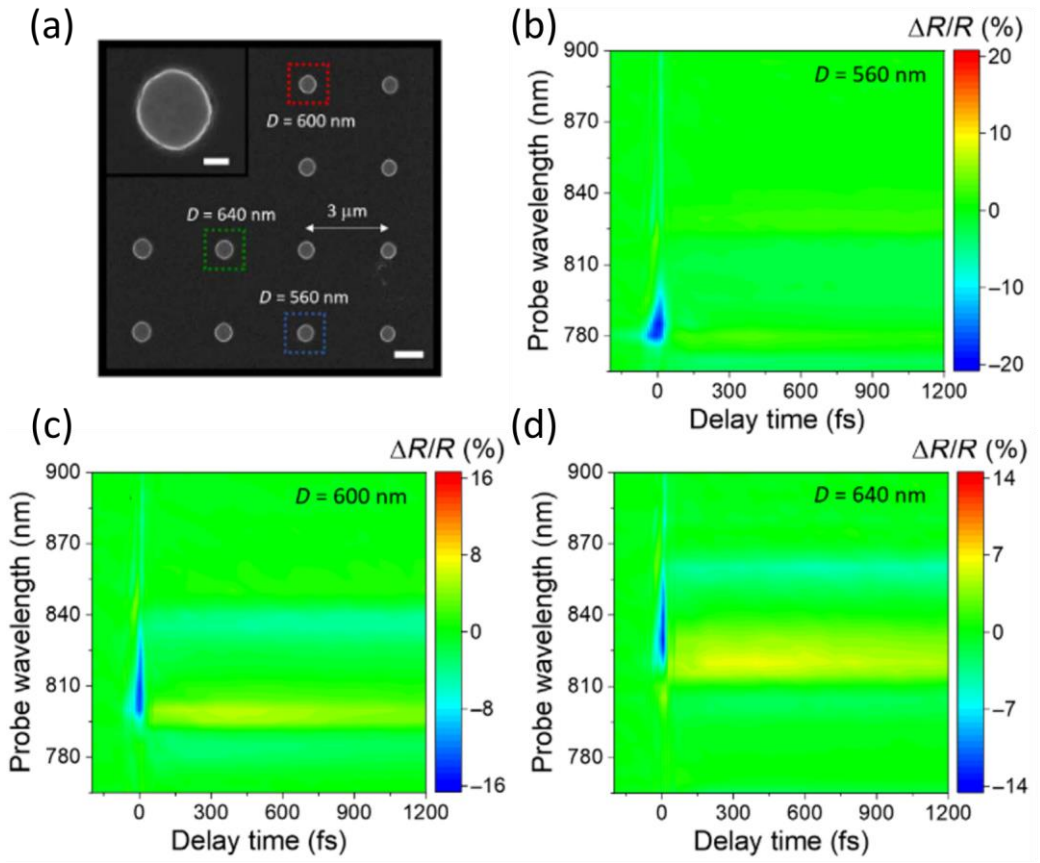

Figure 1.24 All-optical switching of GaP nanodisks. (a) SEM image, inset shows a zoomed-in view of a single 600 nm diameter nanodisk. Scale bars are 1 μm (main image) and 200 nm (embedded image), respectively. (b-d) Differential reflectivity spectra of individual nanodisks with diameters D = 560, 600, and 640 nm at a pump energy density P = 10 pJ/μm² and a pump-probe ratio of 5:1, respectively.[15]

These reflection spectrograms reveal that the smaller size (e.g., D = 560 nm) nanodisks exhibit higher reflection modulation intensities up to about -20% at

probe wavelengths close to the resonance condition. Meanwhile, all samples complete the main modulation in the delay time range of less than 100 fs, further confirming the effectiveness of the synergy between OKE and TPA in GaP nanostructures in ultrafast optical field modulation. In addition, compared with the traditional resonant cavity modulator, this nanostructure-based device without *Q*-factor dependence can avoid the limitation of the resonance lifetime on the response speed, which provides a feasible solution to realize real-time photon control at the nanoscale.

In summary, GaP shows significant advantages in the field of all-optical modulation by virtue of its excellent nonlinear optical properties. Whether it is up to 70% transmission modulation in thin-film structures or sub-20 fs reflection response in nanodisk structures, its performance far exceeds that of previous devices based on oxides or conventional semiconductors. With continued advances in nanofabrication technology, GaP is expected to play a key role as a core material in the next generation of ultrafast photonic chips.

1.5 Research objectives

1.5.1 BIC waveguide optimization

It aims to construct a low-loss bound-state waveguide by realizing the complete decoupling of the continuous spectra of the TM and TE modes in the suspended GaP hybrid waveguide structure using the geometrically-driven multichannel phase-expansion interferometry principle. The waveguide pattern is designed to be etched on a low-refractive index polymer layer and combined with

a high-refractive index GaP film, which retains the excellent optical properties of the single-crystal material and avoids the difficulty of the process of direct etching of the high-refractive index material. Through finite element simulation and experimental measurements, we systematically analyze the influence of geometrical parameters such as waveguide width and bending radius on propagation loss and field distribution, and explore the change rule of loss and fabrication tolerance at different wavelengths (e.g., 1550 nm and 775 nm), so that we can provide high-performance and low-loss propagation waveguides for the integrated photonics circuits.

The third-order nonlinear response of GaP will be quantitatively characterized by combining with the Z-scan technique to measure the two-photon absorption coefficients, nonlinear refractive index, and enhancement of the Kerr effect by the localization of the optical field. By comparing the transient reflectivity modulation depth and response time of different structures, the advantages of structural design in ultrafast all-optical switching are evaluated, and strategies are proposed to further reduce the modulation energy consumption through high-Q resonant cavities or strongly localized subwavelength photonic crystal structures. The ultimate goal is to realize low-power, high-contrast all-optical modulation device design while maintaining picosecond or even femtosecond high-speed response.

1.5.2 Acoustic resonance in Fishnet Structures

This topic is centered around the fishnet membrane structure of suspended GaP films, focusing on exploring its potential for coherent phonon excitation and

mode modulation at the GHz level. By introducing periodic hole arrays on a high-quality GaP film and combining the geometrically complementary (disk-array vs. hole-array) design, we investigate the effects of different aperture diameters and film thicknesses on the frequency of vibration modes, the distribution of mode orders, and the energy leakage paths. The FEM is used to systematically simulate the acoustic field distribution and modal characteristics under optical excitation, and to find the structural conditions to achieve specific mode frequency fixation and high Q retention, so as to inhibit the acoustic wave radiation loss to the substrate and surrounding medium.

In the experimental aspect, the transient reflectance changes under different structural parameters will be measured by ultrafast pump-probe technique, carrier relaxation process and coherent phonon oscillation signals will be separated. The focus is on analyzing the dependence of the mode frequency on the film thickness and its tuning law to verify the numerical simulation predictions. Combining experiments and simulations, we reveal the physical mechanism of decoupling optical excitation and acoustic response, and clarify the modulation of energy dissipation by boundary conditions, membrane suspension form, and aperture array layout. The ultimate goal is to realize localized hypersonic modes with controllable frequency, slow attenuation, and high Q value without sacrificing mode stability, and to provide low-loss and high-performance design solutions.

1.6 Structure of Thesis

Chapter 1: Introduction. This chapter first introduces the research

background and describes the advantages and application prospects of GaP materials in the field of nanophotonics. Then, relevant research progress and key technologies are reviewed from three aspects: linear optical devices, second-order nonlinear devices and third-order nonlinear devices, including high-quality GaP thin films, nano-disks, nanoantennas, metasurfaces, waveguides, and micro-ring resonant cavities. Subsequently, nonlinear effects such as SHG, SFG, and SPDC, as well as THG, HHG, and all-optical switching based on the Kerr effect are briefly described. Finally, the objectives of this thesis: optimization of the BIC waveguide structure and research of acoustic resonance in fishnet structures are clarified, and the structural arrangement of the full paper is outlined.

Chapter 2: Suspended GaP Thin Films for Nonlinear Photonics. This chapter focuses on the design, fabrication and performance testing of suspended GaP thin films. The research motivation and material characterization are first introduced, followed by a detailed description of the methods of numerical calculations, Z-scan measurements and pump-probe experiments. The experimental part demonstrates the optical modulation properties based on optically BIC and quantitatively analyzes the nonlinear optical properties, including the measurements of third-order nonlinear coefficient. Further, picosecond all-optical modulation is realized using ultrafast pump-probe means. The chapter concludes by summarizing the potential of the structure for highly efficient nonlinear photonic devices.

Chapter 3: Suspended GaP Thin Films for Optomechanics. This chapter investigates the design and realization of suspended GaP thin films in the direction of optomechanics. Firstly, the advantages of combining photomechanics

with GaP materials are introduced, and the flow of sample fabrication, numerical simulations, reflection measurements and pump-probe experiments are described in detail. In the result analysis section, a suspended GaP design scheme based on a fishnet structure is proposed, and its mode distribution and quality factor enhancement mechanism are analyzed. The structure is experimentally verified to have excellent performance in excitation and modulation of acoustic modes, which provides a feasible path to realize high-Q optomechanical resonance. Finally, the research results are summarized and future optimization directions are pointed out.

Chapter 4: Summary and outlook. This chapter summarizes the full work. The outlook section suggests possible future research directions, including optimizing the structural design to further enhance the nonlinear response and acoustic mode control accuracy, as well as exploring the prospect of its application in integrated photonic chips.

Chapter 2 Suspended GaP Thin Films for Nonlinear Photonics

2.1 Introduction

Optical communication is a kind of communication mode that uses light as the carrier of information transmission. Because the light used in the communication band itself has a very high frequency (~100 THz), it has a very high information capacity. With the advent of the first double heterojunction semiconductor laser working continuously at room temperature in 1962, people began to obtain a high-quality light source that is highly monochromatic and directional.[93] Corning announced the progress of optical fiber with a loss of 20 dB/km in 1970, and long-distance transmission of light became possible.[94] The development of the optical communication system mainly goes through four stages: in the first stage, 850 nm wavelength light was used as the information carrier, multi-mode fiber was used as the transmission medium[95]; In the second stage, 1310 nm light was used as the carrier, and single-mode fiber was used instead of multi-mode fiber as the medium for transmission.

In the third stage, the light of 1550 nm wavelength began to be used as a carrier for transmission.[96] Beginning in the 1990s, with the advent of Wavelength Division Multiplexing (WDM) technology, the capacity of single-mode fiber began to explode, which greatly reduces the cost of long-distance optical transmission and increases the relay distance.[97] Since then, the fourth-

generation optical communication system has developed rapidly. Thereafter, in order to further expand its transmission capacity and improve its spectrum utilization efficiency, multiplex technologies have been proposed and developed. In addition to that, Differential Binary Phase Shift Keying (DPSK)[98] and N-Quadrature Amplified Modulation (N-QAM)[99] also continue to emerge, further increasing the transmission capacity of the system. With the continuous increase of the information system capacity, it puts forward higher requirements for the information processing capacity of each network node. The emergence of the Optical Add-drop Multiplexer (OADM)[100], Optical Cross Connection (OXC) and wavelength conversion[101], [102] all provide good technical solutions, making the entire optical network more flexible and intelligent.

In order to solve the problem of mismatch between transmission and processing rates in current optical communication networks, while avoiding frequent optic-electrical and electric-optical conversion processes, all-optical signal processing technology[103] has become one of the best choices, the signal is processed directly on the optical domain. The multi-mechanism is reflected in all-optical signal processing, including both linear signal processing, such as using the linear filtering effect of micro-ring to achieve code conversion[104], and nonlinear signal processing[105]. The Four-wave Mixing (FWM) effect is used in highly nonlinear fiber or silicon waveguide[106], and the Free Carrier Effect (FCE) in photonic crystal microcavities is used to realize all-optical switching[107]. It is precisely because the light field itself has multidimensional physical characteristics, while the mechanism between the light field and diverse materials or structures is different, and there are rich optical devices as hardware

support, the current all-optical technology has been able to achieve many key functions. Such as all-optical regeneration[108], all-optical code conversion[109], all-optical sampling[110], all-optical decision[111], etc. On-chip switches and modulators are essential devices for optical communication. In order to achieve these goals, early researchers mainly used a variety of discrete devices to carry out some original exploration, such as fiber Sagnac ring[112], [113], fiber Bragg grating[114], [115], long-period fiber grating[116], [117], fiber ring cavity[118] and so on to realize the time domain all-optical switch.

In the past, due to the wafer architecture and technology of III/V on silicon, high nonlinear coefficient semiconductor photonic devices were unable to realize the full potential of the material. However, the recent birth of the III/V on insulator on-chip integration technology on the whole wafer scale has completely opened the possibility of preparing fully optical modulated optical waveguide structure switches and modulators on the whole wafer scale. Higher refractive index contrast and smoother waveguide interface processing, combined with the excellent nonlinear characteristics of the material, will promote the development of all-optical photonic chips to a new level.

2.2 Methods

2.2.1 Sample fabrication

In this chapter, we fabricated two distinct types of samples: suspended GaP thin films and GaP on glass substrates. For the suspended structures, the GaP layer was first thinned to 300 nm via ICP etching, followed by photolithographic

patterning. The AlGaInP sacrificial layer and GaAs substrate were then selectively removed using buffered oxide and acidic etchants, respectively, to yield a fully released, suspended film. Conversely, the GaP-on-glass samples were realized through a bonding-and-etching approach. A PECVD-grown SiO_2 layer served as the interface for bonding the epitaxial wafer to a glass substrate using a UV-curable adhesive. Following bonding, the GaAs substrate and AlGaInP layer were sequentially removed via selective wet etching to transfer the high-quality GaP film onto the glass. Further technical details are provided in the main text.

2.2.2 Numerical calculations

The mode simulation in chapter 2 is carried out using the FEM software Lumerical MODE v.7.16.2387), aiming to analyze the mode distribution and propagation loss of the suspended GaP thin film waveguide under different geometrical parameters. A 3D model containing a GaP layer, a low refractive index polymer waveguide layer and an air-isolated layer is firstly established, and the corresponding thickness, refractive index and boundary conditions are set. The input wavelengths are selected as 1550 nm and 775 nm, and the TM and TE polarization modes are excited to scan the parameters of waveguide width and bending radius to calculate the effective refractive index and radiation loss. For the bent waveguide, the effect of curvature on mode coupling and loss is further analyzed. The simulation results can determine the structure that satisfy the BIC conditions and are compared with experimental measurements to verify the design accuracy and fabrication tolerance.

2.2.3 Z-scan measurements

In chapter 2.3.2, the third-order nonlinear absorption coefficient and nonlinear refractive index of GaP were characterized using the Z-scan technique. The experimental light source was a femtosecond laser with a pulse width of about 290 fs with a repetition frequency of 50 kHz, and the output wavelength was adjusted to the range of 650-850 nm by an optical parametric amplifier (OPA). The open aperture Z-scan was used to analyze the nonlinear absorption properties, while the closed aperture Z-scan was used to measure the nonlinear refraction effects. During the experiment, the sample was moved back and forth across the focusing spot along the optical axis and a curve of the transmitted power versus position was recorded. By fitting this curve with a theoretical model, the two-photon absorption coefficient (β) and the nonlinear refractive index (n_2) can be obtained simultaneously, and their sign and magnitude can be determined, so that they can be compared and analyzed under different wavelength conditions.

2.2.4 Pump-probe experiments

The light source used in the pump-detection experiments was a femtosecond laser (PHAROS-10W, Light Conversion). The laser has a center wavelength of 1030 nm, a pulse width of about 290 fs, and a repetition frequency of 50 kHz, and the wavelengths of the pump and probe light were adjusted to 775 nm and 600 nm, respectively, by two optical parametric amplifiers (OPA, ORPHEUS-N and ORPHEUS-F, Light Conversion). To suppress the noise at other frequencies, a lock-in amplifier (SR860, Stanford Research Systems) was utilized to extract

the signal at the modulation frequency. The pump and probe light were focused onto the sample surface through the same objective lens (NA = 0.6) with spot radii (e^{-2}) of 1.8 μm (pump) and 1.1 μm (probe), respectively. The average power density of the pump light at the sample was 509.7 J/m². A time-delay stage was set up in the probe optical path, and its position could be adjusted to change the optical range difference between the pump light and the probe light.

2.3 Results and discussion

2.3.1 Photonic Bound States in the Continuum

In the framework of fluctuation theory, a bound state in the continuum (BIC) is a special mode whose energy location lies within the continuum spectrum of a radiating state, yet maintains strict spatial localization without radiating outward. Such states are spatially square-producible, unlike bound states that are usually below the forbidden band. The formation of BICs relies on mechanisms such as phase conditions, symmetry constraints, or multi-channel interference, allowing them to be fully decoupled from the radiative state.

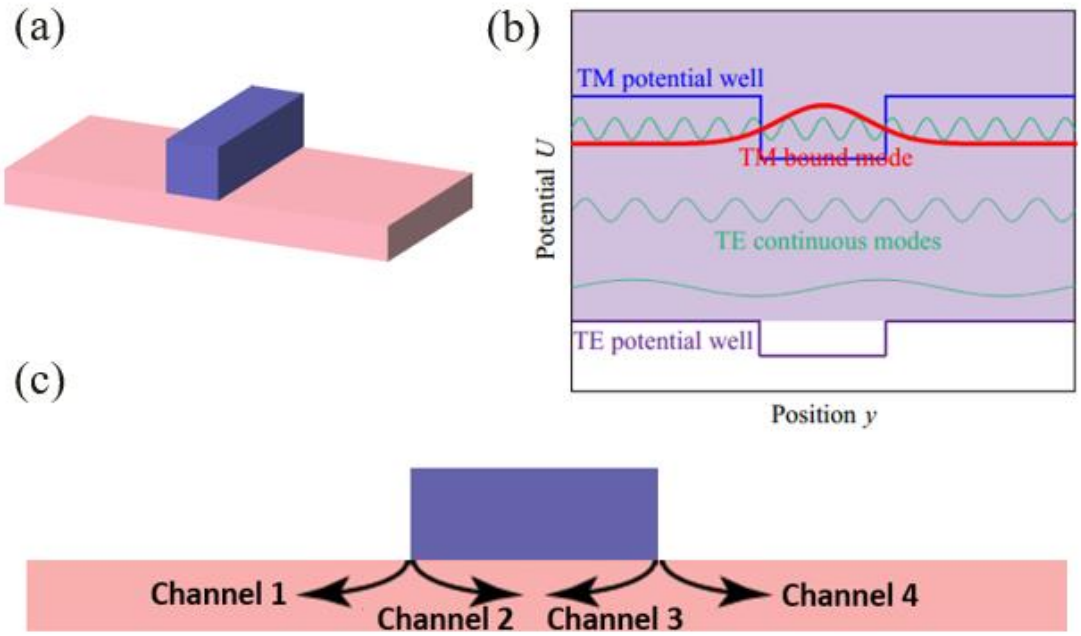

Figure 2.1 BIC waveguide and its modal characteristics. (a) Schematic of a straight waveguide with BIC. (b) Photon potential distribution of the hybrid waveguide structure. (c) TM-bound modes with TE continuum spectrum of the radiation channel.[119]

Figure 2.1(a) illustrates the basic configuration of the straight waveguide we used. The pink area represents a suspended GaP thin film, and the top blue area is polymer waveguide that has been patterned. Unlike etching the waveguide directly on the high refractive index material, we achieve lateral optical field confinement by depositing a low refractive index layer and etching the waveguide pattern on it. This hybrid waveguide structure can utilize the excellent optical properties of high refractive index single crystals while simplifying the fabrication.

Figure 2.1(b) gives a schematic of the optical potential distribution of this

hybrid waveguide. For TM polarization, the waveguide forms a high effective refractive index channel in the transverse direction, forming a “potential well” for the TM modes, which corresponds to the TM potential well shown by the blue curve. corresponding to this, the red curve represents the TM bound modes, whose intrinsic frequencies are located in the continuum spectrum of the TE modes (green waveforms). The red curve corresponds to the TM bound mode, whose eigenfrequency lies in the continuous spectrum of the TE mode (green waveform). The TM modes will radiate into the TE mode and generate losses without special design.

Figure 2.1(c) explains the loss mechanism and suppression method of TM mode visually with a channel model. On both sides of the waveguide, there are TE radiation channels propagating to the left and to the right, labeled as Channels 1~4, respectively, and the radiation loss of the TM modes originates from their coupling with these TE radiation channels. When the geometrical parameters (especially the width of the waveguide) are adjusted to the appropriate values, the radiation between the different channels can interfere with each other so that the total loss is zero, which is the condition for the realization of BIC.

In the design of this structure, a GaP single-crystal film with a thickness of 300 nm was used as the core material, with an air-isolating layer at the bottom and an organic polymer layer with a thickness of 1100 nm covering the top. Figure 2.2(a) shows the propagation loss of the TM mode in a straight waveguide with respect to the width of the waveguide (working wavelength of 1550 nm). From the results, it can be observed that the loss profile shows obvious periodic fluctuations and approaches zero at a particular width position (shown by the red

arrow). This position is exactly the condition where the TM modes are completely decoupled from the TE modes, thus forming a BIC.

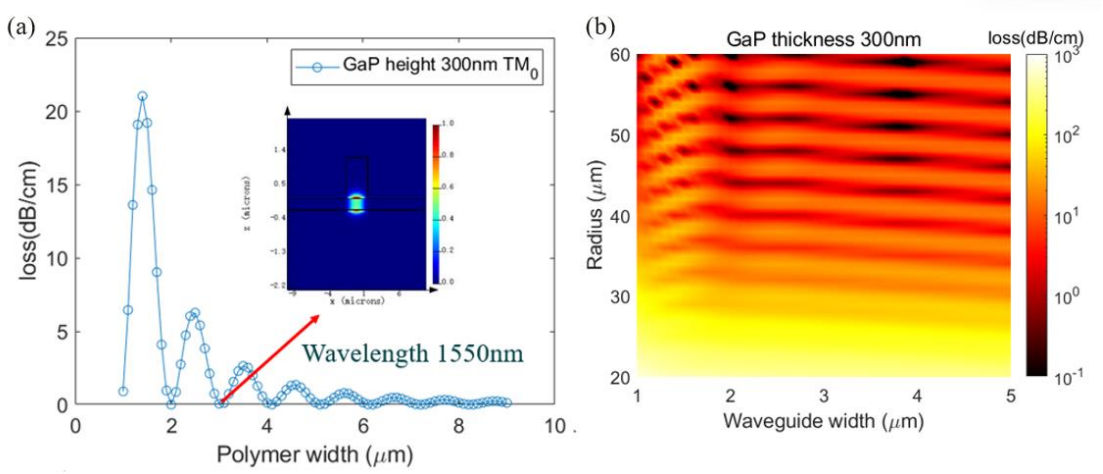

Figure 2.2 Theoretical and numerical results for the BIC waveguide. (a) Propagation loss of TM-bound modes in a straight waveguide versus waveguide width; the inset displays the electric field strength distribution in the waveguide for a waveguide width of 3 μm. (b) Bending waveguide loss versus waveguide width and radius.

This phenomenon is further verified by the mode distribution given in the inset of Figure 2.2(a). In the non-BIC condition, the electric field distribution of the TM modes extends to the outside of the waveguide and radiates toward the substrate, while in the BIC condition, the electric field localization is significantly enhanced and the energy is firmly confined within the GaP layer. It is noteworthy that the loss can still be maintained below 1 dB/cm in the ± 200 nm range around the ideal BIC width, which indicates that the design has a very high fabrication tolerance.

In addition to straight waveguides, bent waveguides are needed in integrated photonic circuits to connect different devices. Figure 2.2(b) gives a two-dimensional plot of TM mode loss as a function of waveguide width w_b and bend radius R_b. The color bars indicate the magnitude of the loss. With some specific combinations of parameters (black areas), it is possible to realize BIC in a bent waveguide so that the bending loss is close to zero.

Similar to straight waveguides, BIC in curved waveguides also relies on a multi-channel phase cancellation interference mechanism. However, due to the waveguide curvature, the electric field distribution at different edges changes asymmetrically, so the coupling strength depends not only on w_b and R_b, but also on the two-side electric field strength ratios are related. This additional degree of freedom makes the BIC conditions for curved waveguides more complex compared to straight waveguides, but at the same time provides a richer optimization space.

In terms of physical nature, the formation of such BICs is different from the symmetry-preserving BICs in photonic crystals. Instead of relying on a strict periodic structure, our design realizes phase-canceling interference between radiation channels by controlling the geometrical phase difference. Therefore, as long as the geometrical parameters satisfy the phase condition $k_y w = 2m\pi$ (m is an integer), the TM modes can be fully decoupled from the TE continuum spectrum, thereby realizing the ideal BIC.

This geometry-driven BIC mechanism is very flexible in terms of material selection. For example, the deposition of polymer waveguides on high refractive index single-crystal GaP is not only simple to fabricate, but also avoids the

fabrication challenges associated with directly etching microstructures on brittle or expensive single-crystal materials. This is especially important when integrating high-performance functional materials such as lithium niobate, diamond, magneto-optical crystals, etc.

We prepared GaP thin-film device materials with multilayer structures on GaAs substrates using MOCVD technology. First, a layer of aluminum gallium indium phosphorus (AlGaInP) with a thickness of about 200 nm was epitaxially grown on the surface of the GaAs substrate as a sacrificial layer, which could be removed by selective wet etching in a subsequent process to release the GaP film above. A GaP epitaxial layer with a thickness of about 600 ± 20 nm is subsequently deposited on its surface. This GaP layer has a (100) biased (011) 15° crystallographic orientation, which facilitates the reduction of the epitaxial defect density and optimizes the optical properties. Figure 2.3 shows a schematic diagram of the GaP/AlGaInP/GaAs three-layer structure and a photograph of an actual wafer, with the GaP layer, the AlGaInP sacrificial layer, and the GaAs substrate in order from top to bottom. The prepared wafers were diced and divided into small pieces of 10 × 10 mm^2 for subsequent micro-nano fabrication and characterization.

The GaP heterostructures used in this work are commercially available. However, the non-negligible density of point defects defects contribute to sub-bandgap transitions and parasitic optical absorption, particularly in the visible spectrum. Consequently, there remains significant scope for optimizing the growth process, such as through the incorporation of buffer layers or refined boron content control, to achieve higher quality crystals with reduced defect

densities in future iterations.

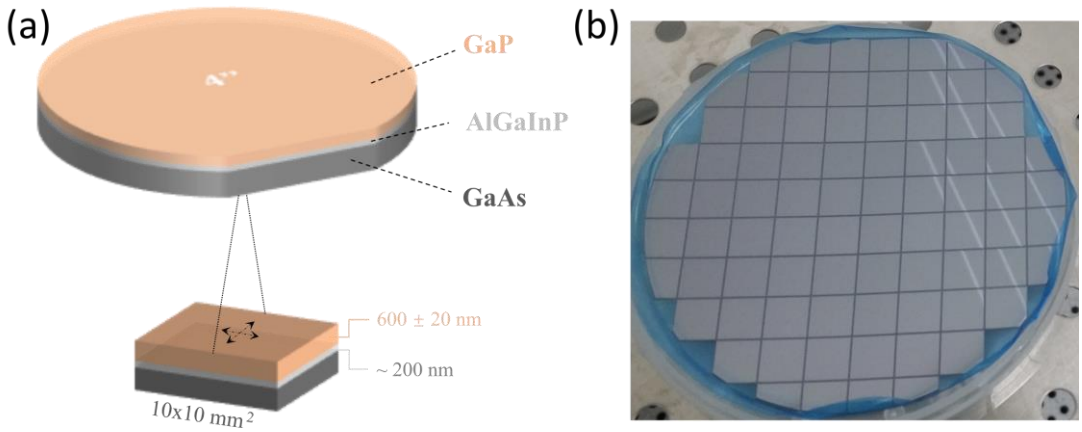

Figure 2.3 Schematic diagram of GaP/AlGaInP/GaAs three-layer structure and photo of actual wafer. The top layer is 600 ± 20 nm thick GaP, the middle layer is about 200 nm thick AlGaInP sacrificial layer, and the bottom layer is GaAs substrate.

In order to confirm the uniformity and interlayer of the epitaxial growth, we utilized SEM to observe the cross-section of the samples after selective etching with BOE buffered oxide etchant. The etching removes part of the AlGaInP layer, revealing the interface between GaP and AlGaInP. Typical cross-sectional SEM images are given in Figure 2.4, where the green marker lines correspond to the thickness of the GaP layer, with the measured values of 600.1 nm, 597.3 nm, and 591.7 nm, and the average thickness of about 596.4 nm, respectively; the red marker lines correspond to the thickness of the AlGaInP layer, with the measured values of 187.0 nm, 173.1 nm, and 167.5 nm, and the average thickness of about 175.9 nm, respectively. 175.9 nm. These results demonstrate that the epitaxial process yields GaP layers with excellent thickness uniformity; the final target

thickness is subsequently achieved with high precision through a calibrated dry etching process. The interface of the three-layer structure is clear and the delamination is obvious, and there is no serious interface roughness or mixed-layer phenomenon.

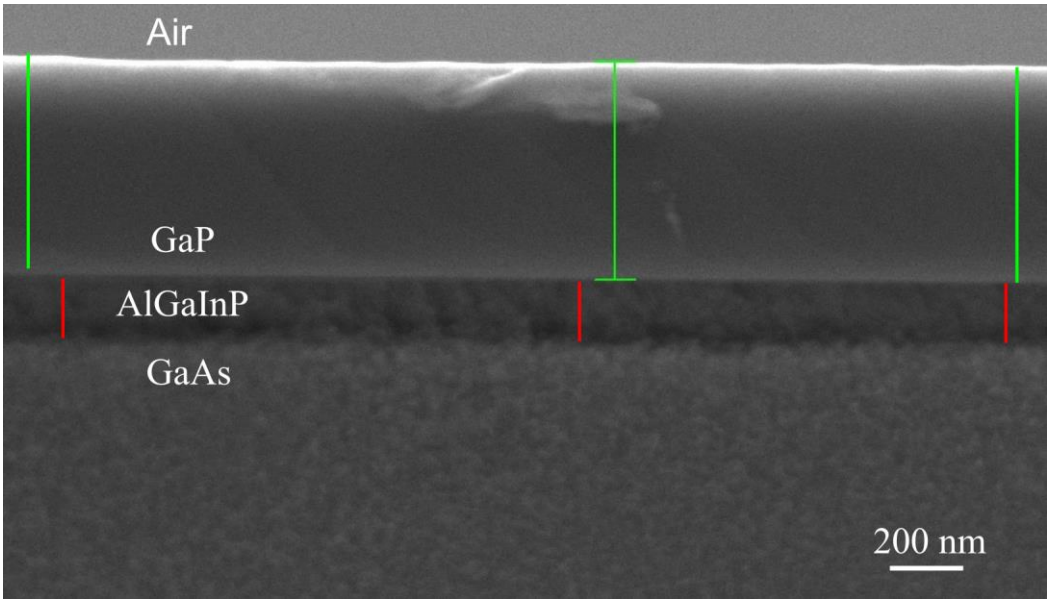

Figure 2.4 SEM image of the sample cross-section after BOE selective etching. The green line is GaP thickness measurement and the red line is AlGaInP thickness measurement.

To further evaluate the surface quality of the GaP thin films, we used AFM to scan the morphology of the 5 μm × 5 μm area. Figure 2.5 shows the topography of the epitaxial GaP layer on an AlGaInP buffer layer with a RMS of about 1.4 nm, indicating a relatively flat surface of the film layer. This lower roughness is usually associated with a uniform nucleation process and stable growth conditions. However, slight surface undulations can still be observed, which may originate from step flow and grain boundary effects during the growth process.

Maintaining a low surface roughness is crucial for the optical performance of photonic devices, as excessive surface undulations increase scattering losses.

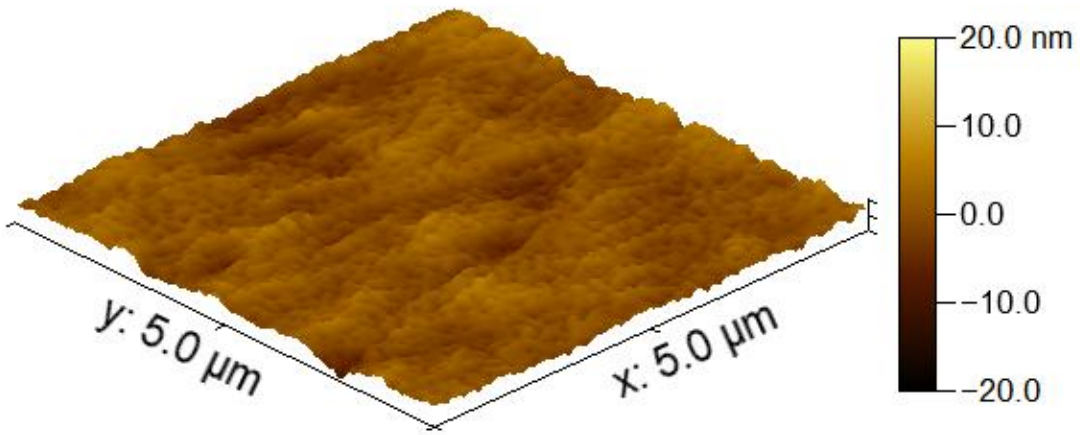

Figure 2.5 AFM image of GaP film surface.

The fabrication flow of the suspended GaP thin film device is shown in Figure 2.6. The wafers used are consistent with the epitaxial structure described above. First, we employed inductively coupled plasma (ICP) etching to thin the GaP layer from about 600 nm to 300 nm using a chlorine-based gas formulation to obtain better pattern constraints and etch control. Subsequently, the designed device pattern was transferred using photolithography. In the fabrication flow, RZJ304.10 photoresist was used to form the desired photolithographic pattern by exposure and development, which was used to transfer the pattern into the GaP layer by ICP etching. After etching, the photoresist was removed using NMP

solution and cleaned with IPA to remove surface residues.

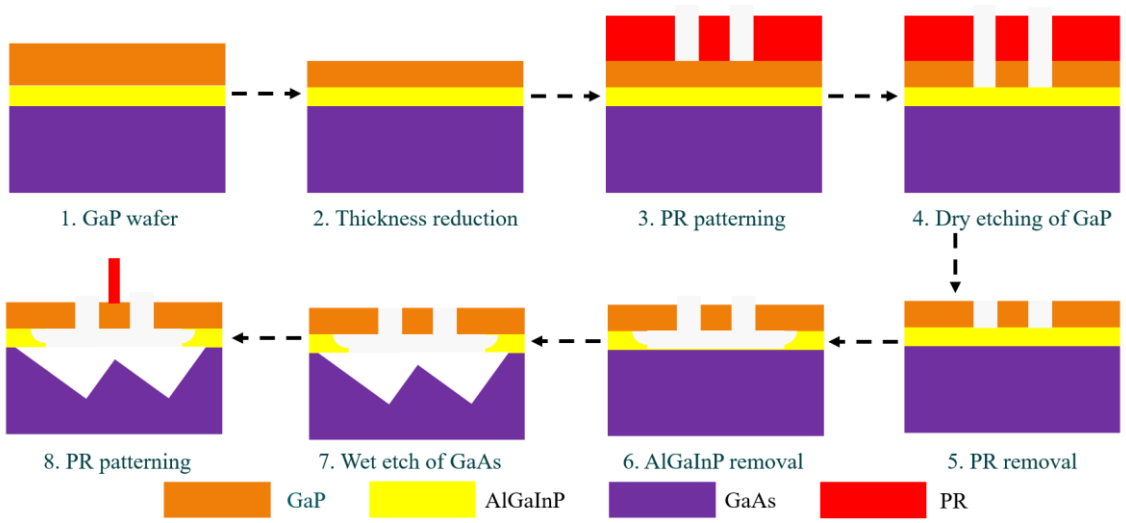

Figure 2.6 Process flow diagram for the fabrication of suspended GaP film.

After the graphic transfer was complete, we used a buffered oxide etching solution to remove the AlGaInP sacrificial layer, thereby creating a cavity underneath the GaP structure. Subsequently, the GaAs substrate underneath is removed using an acidic wet etchant to obtain a fully suspended GaP thin film structure. This release step requires strict control of the etching rate and uniformity to avoid deformation or rupture of the film layer. Finally, to realize specific optical functions, we again perform lithography, exposure and development steps to pattern the polymer waveguide structure on the suspended GaP film to obtain a complete photonic device.

The two-step wet etching process is necessitated by the refractive index hierarchy between the device layer and the growth platform. Since the GaAs substrate possesses a higher refractive index than the GaP epitaxial layer, direct contact would lead to significant optical leakage into the bulk. To facilitate the formation BIC and ensure strong vertical confinement, it is imperative to

construct an air-clad environment. Consequently, the selective removal of the sacrificial GaAs layer serves to establish a high index contrast interface, effectively suppressing substrate radiation and enabling the excitation of high-Q resonant modes within the suspended architecture.

The primary objective of employing a suspended single-crystalline GaP thin-film architecture is to maximize the vertical index contrast, thereby facilitating the formation of BIC. This configuration effectively suppresses radiative leakage into the substrate, ensuring high-Q factor optical confinement within the nanophotonic structures. Furthermore, the removal of the underlying sacrificial layer is strategically designed to release the mechanical degrees of freedom of the GaP membrane. This suspension is critical for enabling the material to function as an acoustic resonator, allowing for the observation of persistent GHz photoacoustic vibrations that would otherwise be heavily damped by energy dissipation into a bulk substrate.

For the optimization of etching conditions, we conducted comparative experiments on the ICP etching effect at different bias RF powers. Figure 2.7 shows the etching morphology and step meter measurement results under two typical powers. When the bias power is 28 W, the etching depth is 68.23 nm, the etching rate is about 2.27 nm/s, and the SEM image shows that the sidewalls are relatively smooth and the etching angle is close to vertical (about 89°). When the bias power was reduced to 24 W, the etching depth increased to 89.08 nm with an etching rate of about 2.97 nm/s, however, the sidewall morphology changed and the inclination angle increased to about 57°. This change may be attributed to the weakened ion bombardment energy at lower power and the greater reliance

on chemical reactions for the etching process, resulting in a weakened etching directionality but an increased rate.

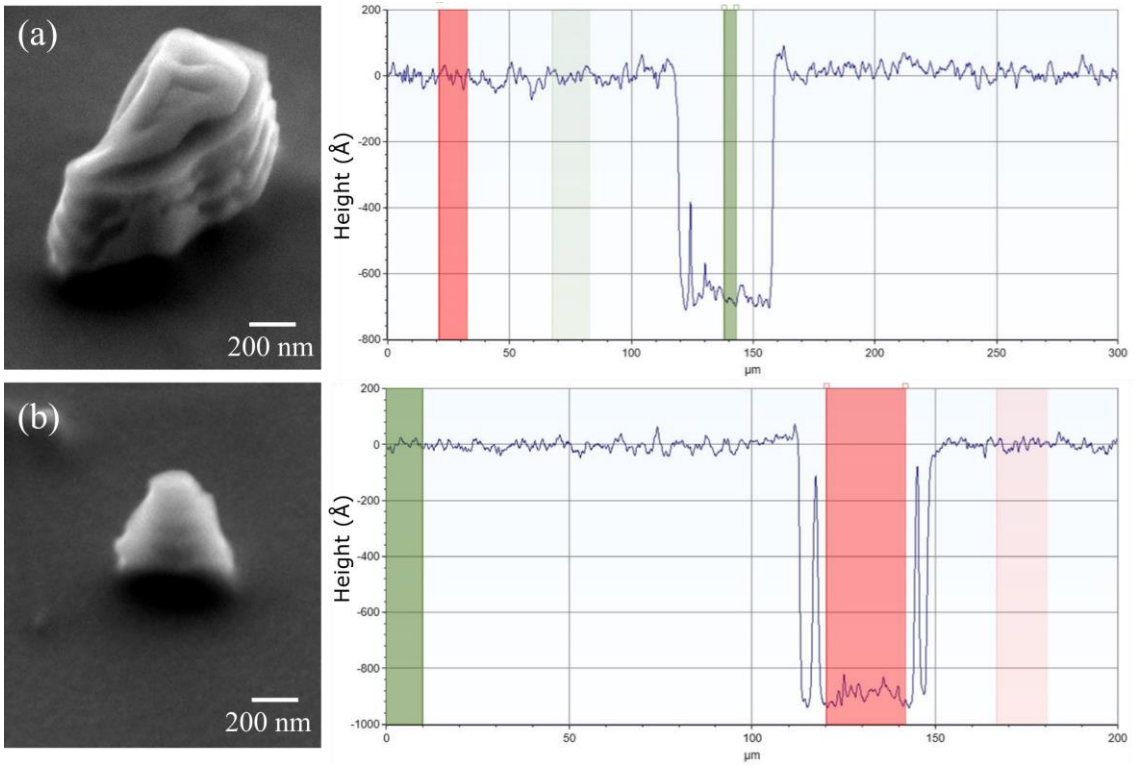

Figure 2.7 ICP etching results and step meter measurements at different bias RF powers. (a) Etching depth of 68.23 nm at 28 W; (b) Etching depth of 89.08 nm at 24 W.

While GaP can be patterned using conventional plasma etching, the adoption of a Waveguide Bound State in the Continuum (BIC) architecture offers several strategic advantages for high-performance photonics. First, by shifting the patterning process to a processable top-cladding layer, we effectively mitigate the scattering losses caused by etching-induced sidewall roughness as shown in Figure 2.8 and lattice damage, thereby preserving the high intrinsic quality of the single-crystal GaP film. Second, the BIC framework provides a robust pathway

for developing suspended membrane structures, which are essential for minimizing substrate-related losses and enabling active piezoelectric or mechanical tuning.[120]–[122] Finally, this design acts as a versatile integration platform; it allows functional materials, such as two-dimensional monolayers or gain media, to be incorporated through additive processes.[123]–[125] This approach avoids the destructive processing of both the active materials and the GaP substrate, facilitating the development of complex, multi-functional photonic integrated circuits (PICs) with reduced fabrication barriers. The final obtained suspended GaP waveguide is shown in Figure 2.9. Under an optical microscope (a), a neatly aligned waveguide array can be seen, with the width of the straight waveguide portion being 3 μm; under a SEM (b), it is clearly visible that the underside of the waveguide has been completely released, forming a high-quality overhanging structure.

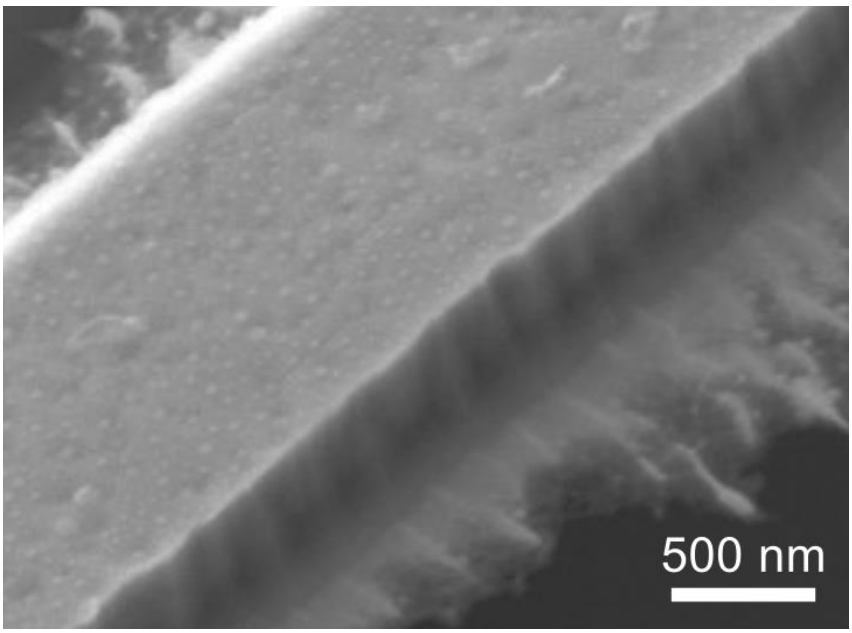

Figure 2.8 SEM image shows the cleaved edge of a GaP waveguide. The sidewall exhibits a series of vertical, parallel striations, indicating significant sidewall

roughness due to the etching process. A 500 nm scale bar is in the lower right.

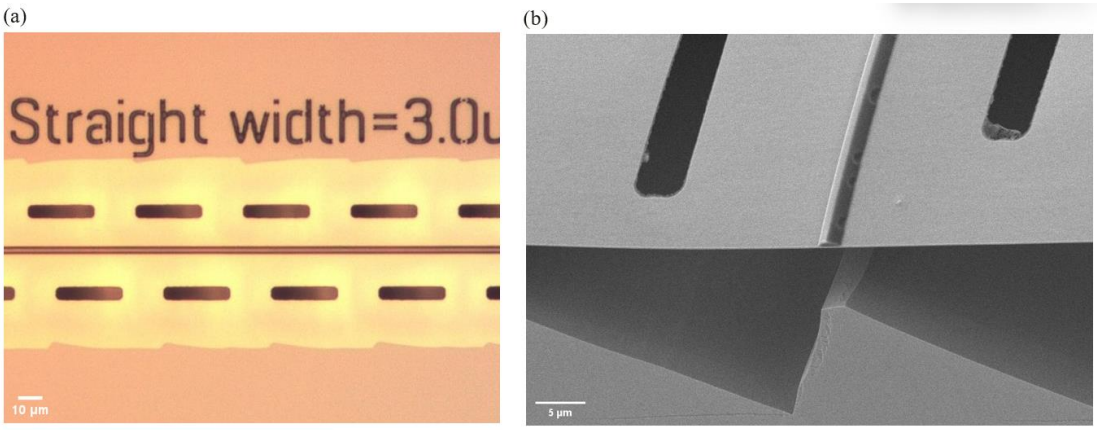

Figure 2.9 Microscopic images of the suspended GaP waveguide. (a) 3 µm wide waveguide array under optical microscope; (b) suspended waveguide structure under SEM.

In order to estimate the surface of the released overhang film, we scanned the 5 µm × 5 µm region again using AFM. The 3D topography of this surface is given in Figure 2.10, and the measured RMS roughness is about 5.3 nm. The increase in roughness compared to the epitaxial initial film surface is mainly due to the slight roughening of the surface caused by plasma etching and wet etching during the release process. Nevertheless, this roughness level is still within the acceptable range. Taken together, the fabrication process established in this chapter is capable of stably preparing high-quality suspended GaP thin-film devices with surface flatness and structural integrity that meet the requirements of high-performance photonic applications.

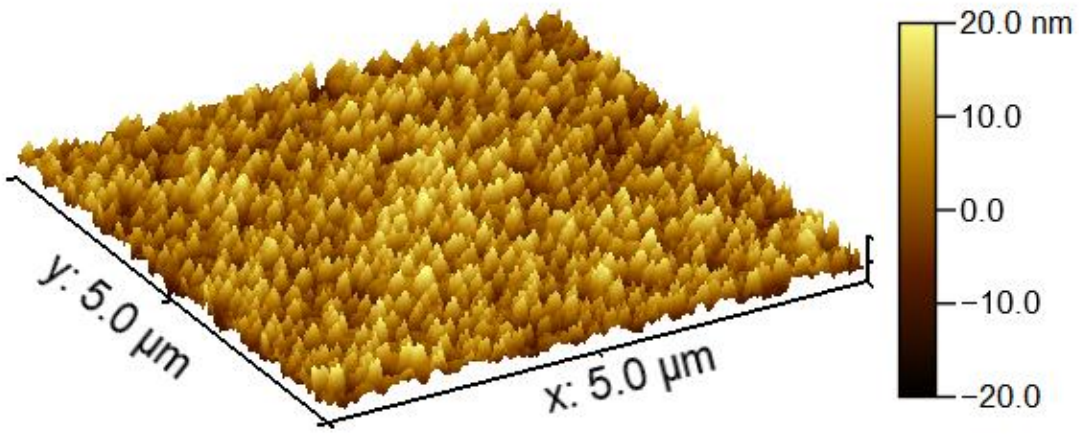

Figure 2.10 AFM image of the surface of the suspended GaP film (scanned area of 5 µm × 5 µm) with RMS roughness of about 5.3 nm.

We perform a systematic propagation loss test at two representative wavelengths (1550 nm and 775 nm) for the linear optical characterization of bound-state waveguides in the continuous spectrum. The tests are performed by the cut-back method, using a lens fiber (LF) with a spot diameter of about 2.5 µm to couple the optical power in and out, respectively, so as to ensure the stability and reproducibility of the coupling conditions. During the test, we recorded the total loss at different waveguide widths and analyzed the relationship between waveguide width and propagation loss by comparing with the simulation results.

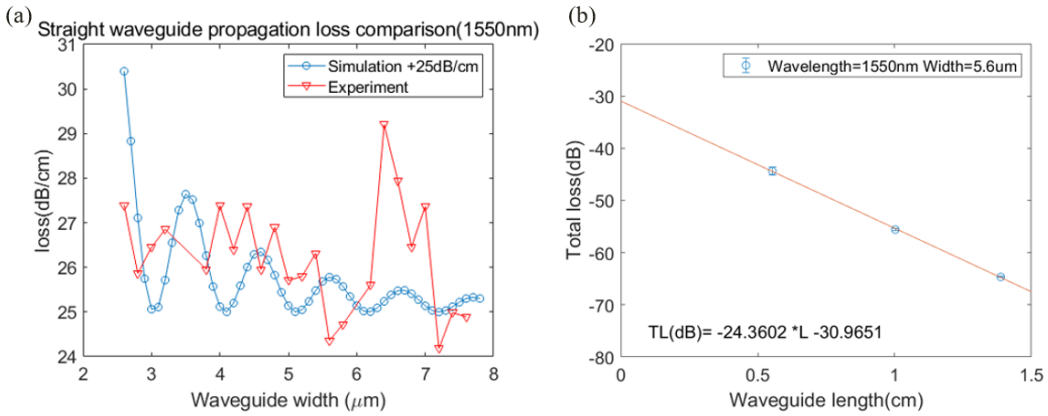

Figure 2.11 Linear optical properties of the bound-state waveguide in the continuous spectrum. (a) Experimental as well as simulated waveguide propagation loss with simulated width. (b) Waveguide propagation loss as a function of waveguide length for a width of 5.6 μm.

Figure 2.11(a) shows the trend of waveguide propagation loss with waveguide width obtained from experimental measurements and simulations at a wavelength of 1550 nm. Although the experimental results are overall higher than the simulation curves with a constant deviation of about 25 dB/cm, the two loss trends remain the same when the waveguide width changes. The high loss in the experiment is mainly attributed to the material intrinsic absorption and scattering losses as well as the surface roughness introduced by the fabrication, and these loss sources are usually not fully considered in the simulation model.

In order to further quantify the propagation loss, we choose a waveguide with a width of 5.6 μm, measure the total loss corresponding to different waveguide lengths at a wavelength of 1550 nm, and fit the results linearly (Figure 2.11(b)). The slope of the fit gives a propagation loss of 24.35 dB/cm for the TM fundamental mode, while the coupling loss per end face corresponding to the

longitudinal axis intercept is about 15.5 dB, which indicates that the propagation loss has become an important part of the total loss at this wavelength, and the coupling loss is also not negligible.

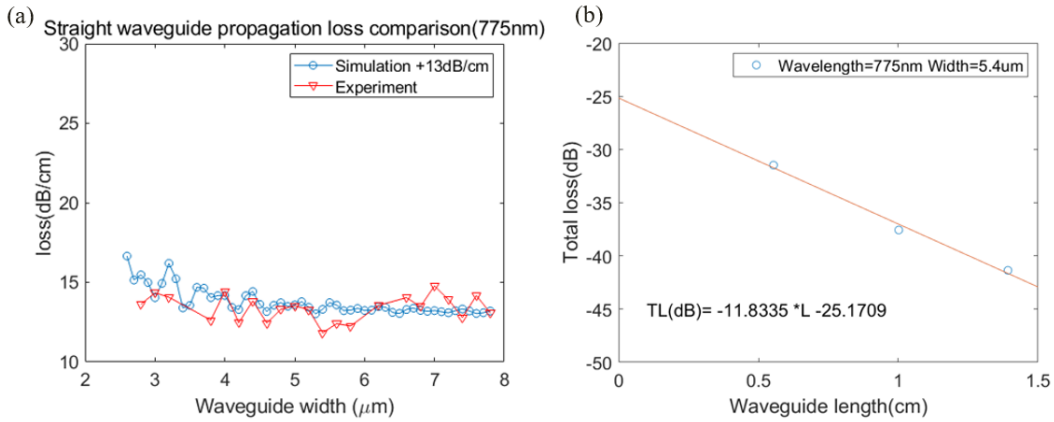

Figure 2.12 Linear optical properties of a bound-state waveguide in the continuous spectrum. (a) Experimental as well as simulated waveguide propagation loss with simulated width. (b) Waveguide propagation loss with waveguide length for a width of 5.4 μm.

At 775 nm, the experimental method is consistent with the parameters. Figure 2.12(a) shows the experimental and simulation results. At this wavelength, the experimental loss profile is overall about 13 dB/cm higher than the simulated profile, but also shows a similar waveguide width dependence. This lower loss difference suggests a more centralized field distribution due to the reduced mode size at shorter wavelengths, resulting in a relatively lower sensitivity to fabrication defects and material loss.

Further, we choose a waveguide with a width of 5.4 μm and measure the total loss for different waveguide lengths at a wavelength of 775 nm and perform a linear fit (Figure 2.12(b)). Compared with the results at 1550 nm, the

propagation loss at shorter wavelengths is significantly lower, which is closely related to the reduction of the mode area and the sensitivity of the waveguide to material absorption.

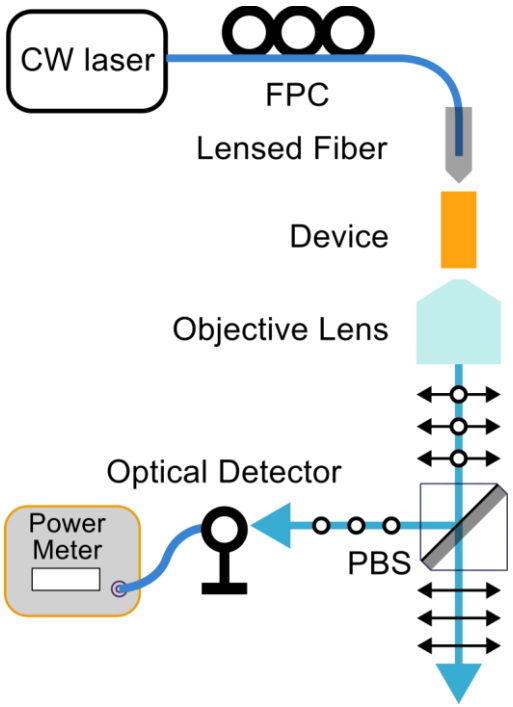

Figure 2.13 Schematic of the experimental setup for distinguishing TE/TM modes. A PBS analyzes the output polarization, enabling identification of the dominant mode based on extinction contrast. FPC: fiber polarization controller.

Taken together, the experimental and simulated results at different wavelengths show consistent width dependence, but the experimental values are overall higher than the simulated values, and the loss is more significant at longer wavelengths. This trend can be attributed to the fact that the longer wavelength modes have greater penetration depth and mode area, which enhances the sensitivity to sidewall roughness and material absorption. The optical performance of the GaP waveguides was characterized specifically for the

Transverse Magnetic (TM) polarization. To distinguish the modes, the chip output was passed through a polarizing beam splitter (PBS) to ensure that the measured power corresponds to the TM component as shown in Figure 2.13. The discrepancy between these experimental values and ideal simulations is primarily attributed to material absorption and fabrication-related scattering. Thermal bistability analysis reveals that material absorption is a dominant factor, with the fraction of absorbed optical power calculated at approximately 92.6% based on the measured thermal susceptibility.[126] Additionally, scattering losses contribute to the background noise, arising from the residual surface roughness (measured at 5.3 nm RMS via AFM) and microscopic inhomogeneities in the photoresist layer. These test results not only verify the validity of the design and simulation models, but also provide an important experimental basis for subsequent waveguide optimization.

2.3.2 Nonlinear Optical Characterization

The third-order nonlinear optical response is a very important optical property in nonlinear optics, which provides the direction for the development of optoelectronic devices and all-optical devices in the aspects of optical switching, optical storage and phase conjugation. The third-order nonlinear effect is the lowest nonlinear property of all media. The difference between the third-order nonlinear response and the second-order nonlinear response is: First, the third-order nonlinear response has the interaction of four photoelectric fields; Secondly, in the second-order nonlinear response, the incident light frequency will change after passing through the medium, while in the third-order nonlinear

response, not only a certain light frequency generated after the incident light frequency passing through the medium can be the same as the incident light frequency, so it can play a role in the attenuation and enhancement of the incident light intensity, such as some parametric scattering processes and Raman induced Kerr effect. In addition, the third-order nonlinear coefficient $\chi^{(3)}$ of different materials or the same material is different at different incident frequencies, but the third-order nonlinear response of the material can be increased by enhancing the resonance effect of the material, which is widely used in material optics. On the other hand, if a specific incident light frequency is kept constant, the optical effect generated by the medium is only corresponding to the incident light frequency, and this effect can make the refractive index of the medium material change, namely: the self-focusing and self-defocusing phenomenon. New output light with unique phase characteristics can also be generated, such as the four-wave mixing phenomenon. It can be seen that third-order optical non-linear effects can also be used in the research of low-dimensional materials. The third-order nonlinear effects mainly include nonlinear absorption and nonlinear refraction. Nonlinear saturation absorption mainly includes saturation absorption, inverse saturation absorption, free carrier absorption and two-photon absorption. For saturation absorption, the main reason is that the ground state electrons will transition to the excited state when excited, so the absorption coefficient is inversely proportional to the incident light intensity. The inverse saturation absorption is due to the accumulation of energy density in the medium, so its absorption coefficient is proportional to the incident light intensity. For carrier absorption, the number of carriers that essentially absorb the pulse energy

is established in the energy band. For two-photon absorption, under the irradiation of strong light, the atom absorbs two photons at the same time through a virtual energy state, from the ground state to the excited state.

The third-order nonlinear optical coefficient measurement methods of materials mainly include Z-scan, degenerate three-wave mixing, four-wave mixing, nonlinear interference, ellipsoid method and beam distortion method. Among them, Z-scan method is simple and easy, and it can also determine the symbol of the nonlinear absorption coefficient and nonlinear refraction coefficient, which is the method adopted in this project. In 1989, M. Sheik-Bahael proposed a Z-scan method for measuring the nonlinear refraction coefficient of materials based on single beam distortion.[127] In 1990, the team expanded the use of the Z-scan method to enable the characterization of nonlinear absorption of materials and proposed a theoretical model for analyzing Z-scan experimental results.[128] The principle of Z-scan method is described as follows: The laser is focused after passing through the lens and diverges after passing through the focus, so when the sample moves before and after the laser focus, different positions correspond to different incident light intensity, resulting in different degrees of nonlinear optical processes inside the sample. By recording the curve of the change of the optical observable amount (generally transmission) of the nonlinear optical process with the sample position. The nonlinear optical coefficient can be fitted by the theoretical model. The nonlinear optical processes characterized by the Z-scan method include nonlinear absorption and nonlinear refraction. Nonlinear absorption includes saturation absorption and inverse saturation absorption. Saturation absorption means that the greater the light

intensity, the weaker the absorption of the material, and the corresponding nonlinear absorption coefficient is negative. Inverse saturation absorption such as two-photon absorption means that the greater the light intensity, the stronger the absorption of the material, corresponding to a positive nonlinear absorption coefficient. The nonlinear refraction will cause the shift of the laser focus position. According to the different characteristics of the material, nonlinear refraction will have two kinds of effects: self-focusing and self-defocusing. The self-focusing will cause the laser light to converge inside the material (as shown in Figure 2.14(a)), and the corresponding nonlinear refraction coefficient is positive. Self-defocusing causes the laser light to diverge inside the material (as shown in Figure 2.14(b)), corresponding to a negative nonlinear refraction coefficient.

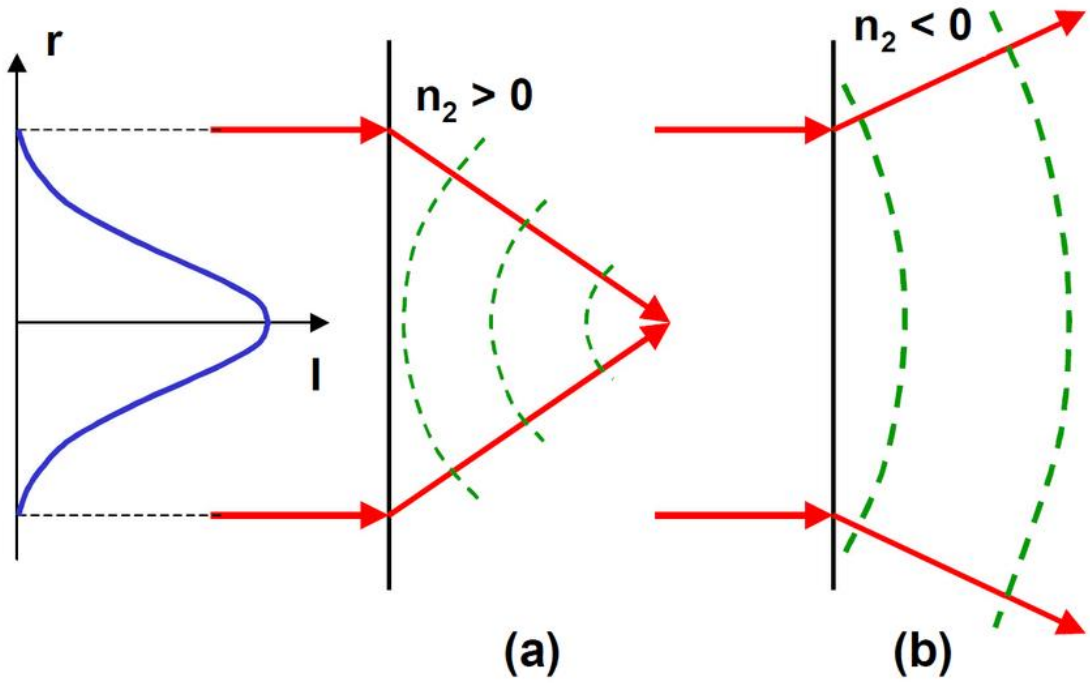

Figure 2.14 (a) Self-focusing and (b) self-defocusing schematics.

A femtosecond laser Z-scan system is shown in Figure 2.15. The system is equipped with an optical parametric amplifier to adjust the operating wavelength of the femtosecond laser, and the nonlinear absorption and refraction coefficients of the material are obtained by transmission Z-scan measurements. The focal length of the lens used in the system is 250 mm. Detector D1 acquires open aperture Z-scan data, which is mainly used to study the nonlinear absorption properties, while detector D2 acquires closed aperture Z-scan data, which is used to analyze the nonlinear refraction effects.

When the material is saturated absorption, the greater the incident light intensity, the lower the absorption and the higher the transmittance; if it is anti-saturation absorption, the increase in light intensity will lead to enhanced absorption and weakened transmission. Using D1, the correspondence between transmittance and sample position can be obtained, and the link between transmittance and incident light intensity can be further extrapolated to fit the nonlinear absorption coefficient. Due to the nonlinear refraction process, the spot size at the position of the small hole varies with the incident light intensity; with the help of D2, the relationship between the transmittance of the closed hole and the position of the sample can be measured and the correlation with the incident light intensity can be deduced, from which the nonlinear refraction coefficient can be fitted.

We simulate the complete optical process through the theoretical model, derive the theoretical expressions for the variation of open and closed aperture transmittance with sample position, and experimentally measure the relationship between the two and the position of the sample, and finally fit the nonlinear

optical coefficient with the theoretical model. The two-photon absorption of visible light can cause electrons to jump to the conduction band and involves different jump processes across the indirect and direct bandgaps. Therefore, this work measures and compares the nonlinear optical coefficients of the material at different wavelengths, which helps to deeply understand the energy band structure of the material from an experimental point of view and reveals the details of the femtosecond laser interaction with the material.

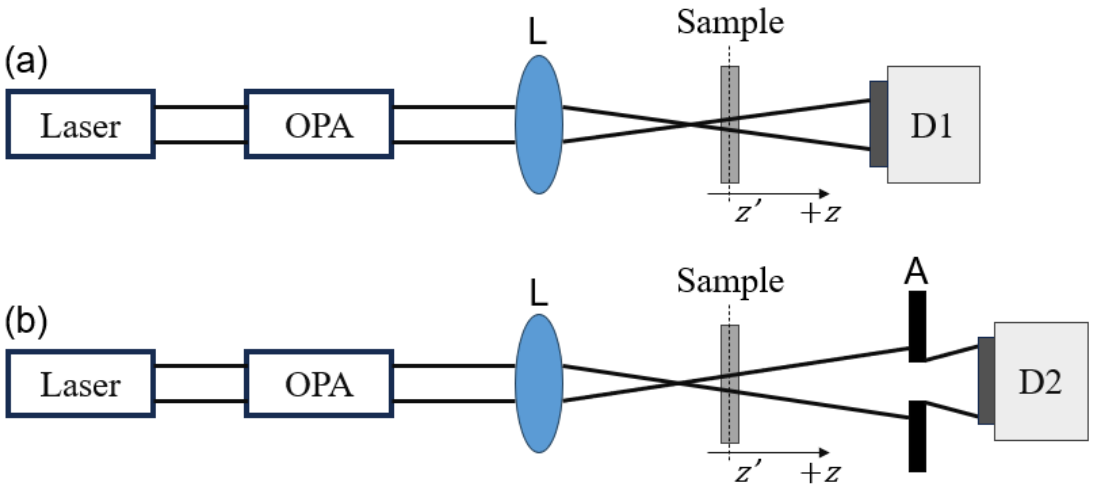

Figure 2.15 Z-scan (a) open-aperture measurement setup and (b) closed-aperture measurement setup. L denotes a convex lens with a focal length of 250 mm, D1 and D2 are the power detectors, and A represents the diaphragm.

In the linear optical range, the absorption coefficient of the material remains constant; whereas in the nonlinear optical range, the absorption coefficient α is related to the light intensity I as:

$$\alpha = \alpha_0 + \Delta\alpha = \alpha_0 + \beta I + \gamma I^2 + \cdots \quad (2.1)$$

In the equation, α_0 is the linear absorption coefficient of the material. When nonlinear optical processes are present, the absorption coefficient changes and is

denoted as $\Delta\alpha$, where β is used to characterize the two-photon absorption effect and γ is used to describe the three-photon absorption effect. Nonlinear absorption will cause changes in the light intensity distribution. It is necessary to calculate the incident light intensity distribution $I_i(r,z,t)$ and the light intensity distribution $I_e(r,z,t)$ after the non-linear refraction of the sample, and then calculate the open aperture transmission of the sample by the ratio of the integral of the light intensity before and after the sample in space and time.

The incident Gaussian beam has a beam waist radius w_0 of the electric field and propagates along the direction of $+z$, whose expression of the electric field distribution is as following:

$$E(r,z,t) = \frac{E_0(t)w_0}{w(z)} exp\left(-\frac{r^2}{w^2(z)} - \frac{ikr^2}{2R(z)}\right) e^{-j\Phi(z,t)} \quad (2.2)$$

At the center of the beam at the focal point, $E_0(t)$ shows the amplitude of the electric field, the radius of beam satisfies $w^2(z) = w_0^2(1 + z_0^2/z^2)$, $R(z) = z(1 + z^2/z_0^2)$ is the wavefront curvature radius at position z, $k = 2\pi/\lambda$ is the wavevector and $z_0 = kw_0^2/2$ represents the Rayleigh length of the light, and $e^{-j\Phi(z,t)}$ tells the phase change during propagation.

The distribution of incident light intensity at the sample surface is obtained by electric field distribution as follows:

$$I_i(r,z,t) = \frac{1}{2} c\varepsilon_0 n|E(r,z,t)|^2 = \frac{1}{2} c\varepsilon_0 n E_0^2(t) \frac{w_0^2}{w^2(z)} exp\left[-\frac{2r^2}{w^2(z)}\right] \quad (2.3)$$

Where c denotes the speed of light, n is the refractive index of the material, and ε_0 is the vacuum dielectric constant.

When the thickness of the sample is much smaller than the Rayleigh length, the variation of the beam radius inside the sample is negligible. In the case where

the sample undergoes two-photon absorption, the higher-order nonlinear absorption processes can be approximately neglected. In the internal coordinate system of the sample z', the variation law of light intensity inside the sample can be described by the following differential equation:

$$\frac{dI}{dz'} = -\alpha_0 I - \beta I^2 \tag{2.4}$$

Taking the light intensity distribution Equation 2.3 on the surface of the sample as the boundary condition, the differential Equation 2.4 is solved to obtain the transmitted light intensity distribution $I_{e2}(r,z,t)$ and when the material is undergoing two-photon absorption. By integrating the transmitted and incident light intensity distributions in space and time and dividing by the total incident energy, the transmission expressions for two-photon absorption can be obtained.

$$T(z) = \frac{\iint I_{e2}(r,z,t)drdt}{\iint I_i(r,z,t)drdt} = \frac{1}{\sqrt{\pi}q_0(z)}\int_{-\infty}^{+\infty} \ln\left[1 + q_0(z)e^{-\tau^2}\right] d\tau \tag{2.5}$$

where

$$\tau = \frac{z}{z_0}$$

$$q_0(z) = \beta I_0 L_{eff}/(1 + \frac{z^2}{z_0^2})$$

$$L_{eff} = \frac{1 - e^{-\alpha_0 L}}{\alpha_0}$$

Where I_0 shows the peak light intensity in the focal plane, L_{eff} represents the equivalent thickness of the material when two-photon absorption occurs.

The transmission in Equation 2.5 is normalized, and the normalization factor is the transmission of the material without nonlinear optical process $T(\infty)$. The two-photon absorption coefficient β_{TPA} can be obtained by fitting the

transmittance T obtained from the open aperture Z-scan experiments to the sample position z using Eq. (2.5).

According to the theoretical derivation, for each open-aperture Z-scan measurement, it is necessary to obtain the peak light intensity for that experiment I_0 and the linear absorption coefficient of the material at that wavelength α_0. Where the peak light intensity I_0 can be calculated by the following equation:

$$I_0 = P/S/t_{FWHM}/f \;\; S = \pi r_x r_y \tag{2.6}$$

Where P shows the beam power, S is the spot area at the focus, t_{FWHM} is the full width of femtosecond laser at half maximum, f is the repetition rate of the laser, r_x and r_y is the radius of the laser cross section in the x and y direction at the focus. The radius is the distance between the spot center and the position where the light intensity decays to $1/e^2$ of the light intensity in the spot center.

The linear absorption coefficient α_0 can be obtained by Equation 2.7:

$$\alpha_0 = -\ln(P_o/P_i)/L \tag{2.7}$$

Where P_i shows the power before, P_o represents the power passing through the sample at a location that does not cause nonlinear absorption, and L is the sample thickness.

In the nonlinear optical category the refractive index is related to the light intensity:

$$n = n_0 + \Delta n = n_0 + n_2 I + n_3 I^2 + \cdots \tag{2.8}$$

where n denotes the refractive index, Δn is the refractive index change due to nonlinear optical effects, n_0 is the linear refractive index of the material, and n_2 and n_3 corresponds to the third-order and fifth-order nonlinear refractive indices, respectively.

Nonlinear refraction leads to a change in the phase of the electric field. Therefore, in order to obtain the relationship between the closed hole transmittance and the position of the sample, it is necessary to first calculate the incident electric field distribution $E_i(r,z,t)$ as well as the electric field distribution of the sample after the effect of nonlinear refraction $E_e(r,z,t)$ from which the transmitted optical power of the sample is found. Then, in combination with the role of small holes, the optical power through the small holes and the optical power through the small holes when there is no nonlinear refraction are integrated in time separately, and the ratio is taken to obtain the closed hole transmittance of the sample.

When the thickness of the sample is much less than the Rayleigh length, the change of its internal beam radius can be ignored. At this time, the wavefront phase change caused by the refractive index change Δn can be expressed as:

$$\Delta\Phi(r,z,t) = \frac{\Delta\Phi_0(t)}{1+z^2/z_0^2}\exp\left(-\frac{2r^2}{w^2(z)}\right) \tag{2.9}$$

Where $\Delta\Phi_0(t) = k\Delta n(t)L_{eff}$ is the phase change of the wavefront at the focus.

The distribution of the electric field on the emission plane of the sample can be described as:

$$E_e(r,z,t) = E_i(r,z,t)e^{-\frac{\alpha L}{2}}e^{i\Delta\Phi(r,z,t)} \tag{2.10}$$

The electric field may be expressed as the superposition of multiple Gaussian beam components, each having a distinct waist radius, it can be expressed as:

$$e^{i\Delta\Phi(r,z,t)} = \sum_{m=0}^{\infty}\frac{[i\Delta\Phi(r,z,t)]^m}{m!}e^{-\frac{2mr^2}{w^2(z)}} \tag{2.11}$$

Based on Huygens' principle, each sub-Gaussian beam is allowed to propagate through the aperture independently, after which they are recombined at the aperture plane. In this way, the electric field distribution on the aperture plane can be determined as:

$$E_a(r,z,t) = E(0,z,t)e^{-\frac{\alpha L}{2}}\sum_{m=0}^{\infty}\frac{[i\Delta\Phi(r,z,t)]^m}{m!}\frac{w_{m0}}{w_m}e^{-\frac{r^2}{w_m^2}-\frac{ikr^2}{2R_m}+i\theta_m} \quad (2.12)$$

Define d as the spatial distance between the sample and the plane where the hole is located, and set $g = 1 + d/R(z)$, where the parameters are as following:

$$w_{m_0} = \frac{w(z)}{\sqrt{2m+1}}$$

$$d_m = \frac{k\omega_{m_0}^2}{2}$$

$$w_m^2 = w_{m_0}^2\left(g^2 + \frac{d^2}{d_m^2}\right)$$

$$R_m = d\left(1 - \frac{g}{g^2 + d^2/d_m^2}\right)^{-1}$$

$$\theta_m = \tan^{-1}(\frac{d/d_m}{g})$$

The optical power transmitted through the aperture is proportional to the surface integral of the squared electric field amplitude over the aperture area:

$$P_t[z,\Delta\Phi_0(t)] = c\varepsilon n_0\pi\int_0^{r_a}|E_a(r,z,t)|^2 r dr \quad (2.13)$$

Taking into account the temporal variation of the optical power, the transmission obtained from the normalized closed-aperture Z-scan can be expressed as:

$$T(z) = \frac{\int_{-\infty}^{\infty} P_t[z,\Delta\Phi_0(t)]dt}{S\int_{-\infty}^{\infty} P_i(t)dt} \tag{2.14}$$

Where $P_i(t) = \frac{\pi w_0^2 I_0(t)}{2}$ represents the incident light power, $S = 1 - \exp(-2r_a/w_a)$ is used to measure the size of the aperture, r_a denotes the aperture radius, while w_a represents the beam radius at the aperture plane.

In actual calculation, let $\Delta\Phi(t) \leq 1$, if the far field condition $d \gg z_0$ is satisfied, the first two terms of Taylor series can be retained to obtain the sufficiently accurate normalized transmission. The approximate normalized transmission expression is as follows:

$$T(z,\Delta\Phi_0) = 1 - \frac{4\Delta\Phi_0(t)\tau}{(\tau^2+9)(\tau^2+1)} \tag{2.15}$$

In closed aperture Z-scan experiments, nonlinear absorption also affects the measurement results. Therefore, after obtaining the closed aperture Z-scan data, it is necessary to divide it with the open aperture Z-scan data to eliminate the interference of nonlinear absorption on the results of closed aperture experiments.

The bandgap of GaP is about 2.26 eV, and the output bands of commercially available femtosecond lasers are mostly located in the near-infrared or visible ranges, so the energy absorption of femtosecond lasers by GaP is mainly dependent on multiphoton absorption. However, data on the relevant nonlinear absorption coefficients in the existing literature are very limited and only for a few specific wavelengths. At the same time, the femtosecond laser induces a nonlinear refraction effect in GaP, resulting in a self-focusing phenomenon and a certain shift of the laser focus position. The two-photon absorption properties and nonlinear refractive behavior of GaP are systematically investigated in the

wavelength range of 650-850 nm by variable wavelength Z-scan experiments.

For GaP in this experiment, a typical two-photon absorption wavelength of 800 nm was selected for Z-scan experiment, and its nonlinear absorption coefficient was obtained by fitting the two-photon absorption model. As shown in Figure 2.16, as the sample moves from the left side of the focus (-*z* axis) to the focus, the transmittance of the sample gradually decreases and reaches the lowest value at the focus position. However, as the sample moved from the focus to the right side of the focus (+*z* axis), the transmission of the sample gradually recovered. In this process, the surface light intensity of the sample first becomes strong and then becomes weak, and the absorption of the sample also first becomes strong and then becomes weak, indicating that GaP has inverse saturation absorption properties.

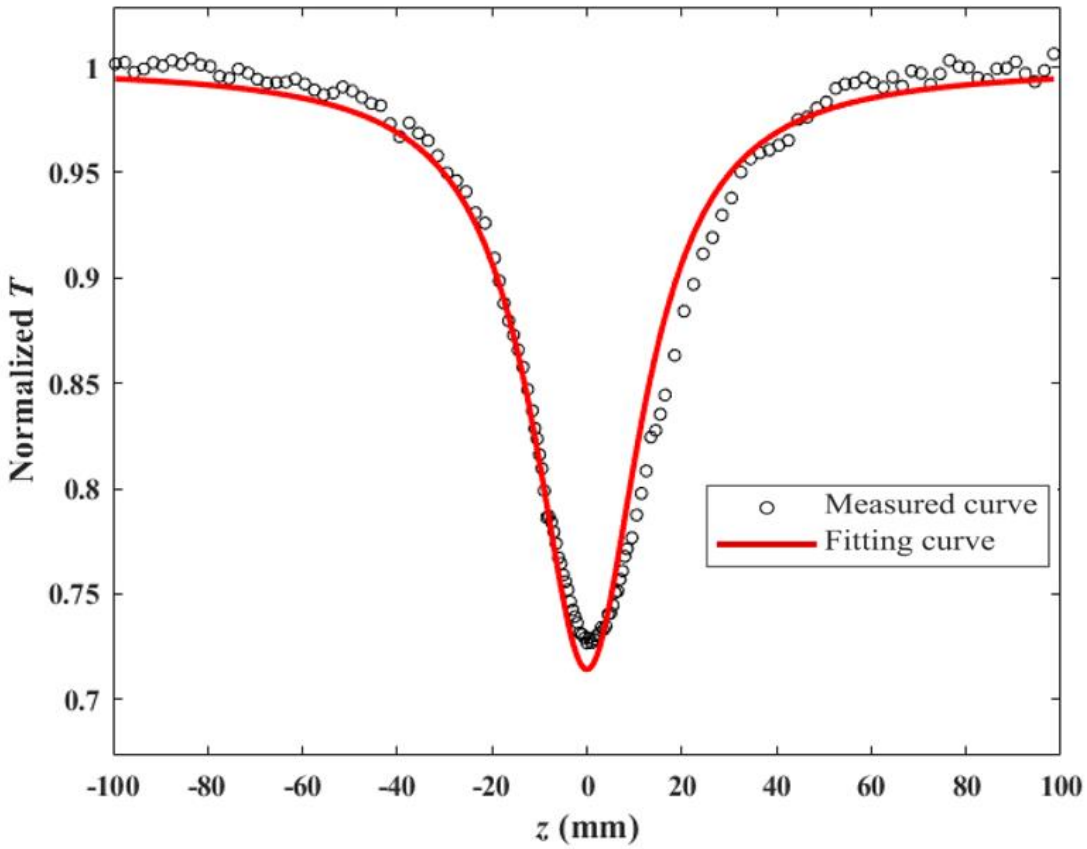

Figure 2.16 The open aperture Z-scan curve and fitting curve of GaP at 800nm.

In the experiment, the closed aperture Z-scan experimental data of GaP in the range of 650-850 nm were measured using an optical parametric amplifier combined with the Z-scan technique, and the nonlinear refractive coefficients of GaP were obtained by fitting the nonlinear refractive theory model. Typical closed aperture Z-scan test results and the fitted curves are shown in Figure 2.17. As can be seen from the figure, under the 800 nm femtosecond laser irradiation, as the position of the sample moves from the left side to the right side of the focus, the transmission curve first shows a valley and then a peak, which indicates that GaP has the self-focusing property.

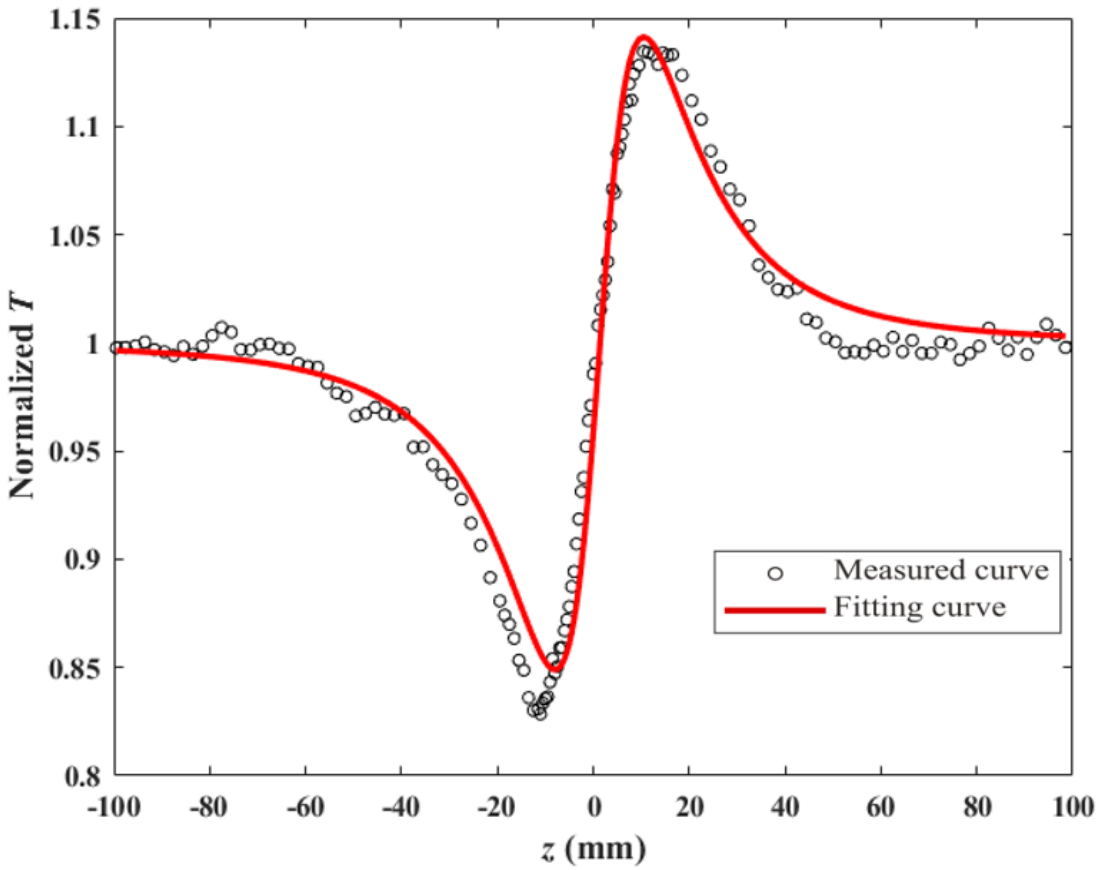

Figure 2.17 The closed aperture Z-scan curve and fitting curve of GaP at 800nm.

When the sample is very far to the left of the focus, the laser spot on the sample is large, the light intensity is weak, and will not cause nonlinear refraction. In this case, the laser energy through the small aperture can be used as a normalized benchmark. When the sample reaches the position near and in front of the focus, the light intensity is stronger, and the laser self-focusing of the sample pair causes the focus position to move to the *-z* direction. After the focus, the divergence distance becomes longer, and the spot size becomes larger before the laser reaches the small aperture, the small aperture size is fixed, so the laser energy through the small aperture becomes smaller, corresponding to the valley in the transmission change curve. When the sample is at the focal point,

the focus position does not change, and the laser energy through the aperture is the same as when the sample was at the initial position. When the sample is near and behind the focus, the laser beam begins to diverge when it reaches the sample. The self-focusing of the sample leads to the decrease of the laser divergence angle, the size of the spot before the laser beam reaches the small aperture, and the laser energy passing through the small aperture increases, corresponding to the peak in the transmission change curve.

The observed asymmetry in the closed aperture Z-scan traces is attributed to a combination of instrumental factors and sample induced perturbations. Potential sources include non-ideal Gaussian beam profiles, slight misalignments in the far-field aperture centering, or local inhomogeneous scattering within the GaP membrane. To resolve these discrepancies, a systematic calibration protocol is mandated: the optical system must first be benchmarked using a standard reference material to ensure precise alignment and characterize the intrinsic beam waist. Following this baseline correction, the experimental measurements can be revalidated to isolate the material's nonlinear refractive response from systematic artifacts, thereby ensuring the accuracy of the extracted nonlinear indices.

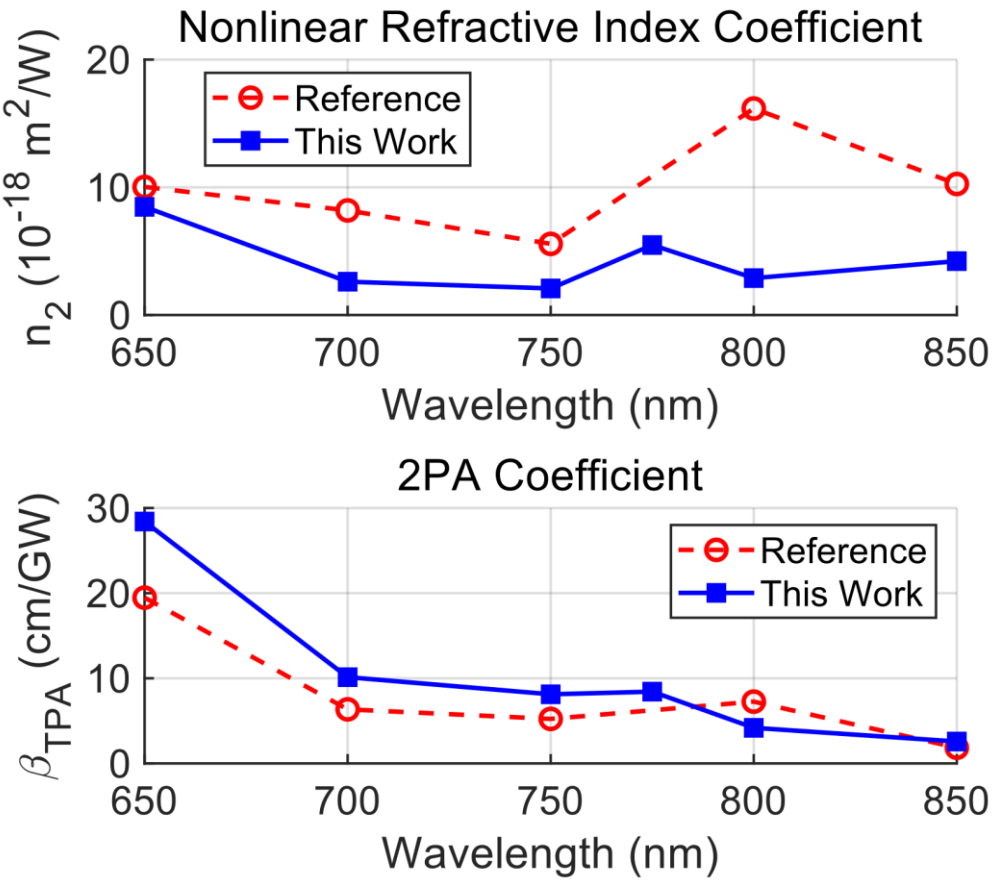

Figure 2.18 Nonlinear refractive index/Two-photon absorption coefficients from 650 nm to 850 nm for GaP compared with reference[16].

Table 2.1 Comparison of nonlinear refractive index and two-photon absorption coefficient with reference[16].

Wavelength(nm)	Nonlinear refractive index coefficient ($10^{-18}m^2/W$)		TPA coefficient (cm/GW)	
	Ref.	This work	Ref.	This work
650	10.03	8.47	19.47	28.41
700	8.19	2.61	6.35	10.13
750	5.57	2.08	5.23	8.12
775	-	5.48	-	8.43
800	16.17	2.89	7.26	4.18

850	10.26	4.22	1.84	2.57

The theoretical model of closed hole Z-scan considers that the laser satisfies the Gaussian beam propagation equation and requires the laser center to coincide with the aperture center exactly. In the actual experiment, due to the accuracy of the lens position and the quality of the spot, there may be differences from the hypothesis, which brings great challenges to the Z-scan experiment at different wavelengths. Finally, we selected several specific wavelengths and repeatedly adjusted the optical path to measure the nonlinear refraction coefficient and nonlinear absorption coefficient, the results are shown in Figure 2.18. The results of nonlinear refraction coefficients and absorption coefficients at 750 nm are numerically close to those reported in the previous literature [54].

2.3.3 Ultrafast All-Optical Modulation

In another set of fabrication, we used a combination of bonding and wet etching to transfer GaP films epitaxialized on GaAs substrates to glass substrates, thus realizing the stripping and reuse of high-quality films. The process starts with a GaP/AlGaInP/GaAs multilayer epitaxial wafer as the starting material as shown in Figure 2.19, where GaP is the target functional layer, AlGaInP is used as the sacrificial layer, and GaAs is the support substrate. A layer of SiO_2 was grown on the GaP surface by PECVD to serve as a protective layer and intermediate medium for subsequent bonding.

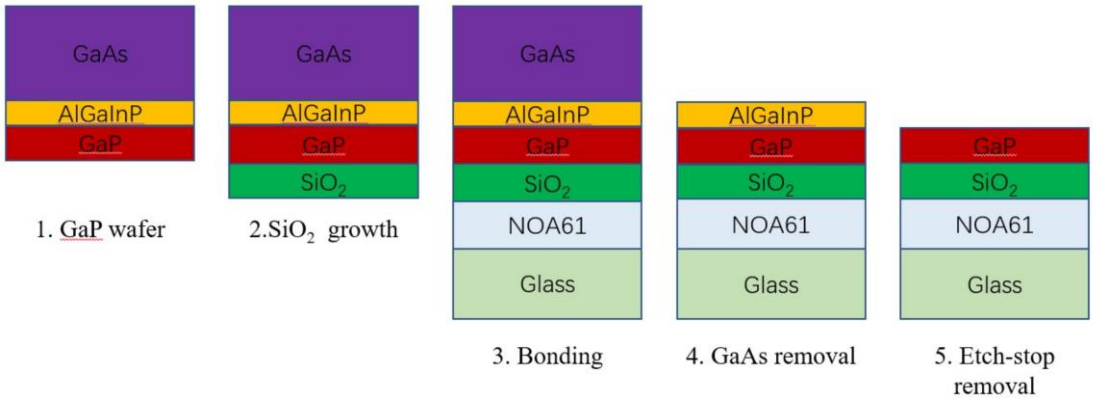

Figure 2.19 Schematic diagram of the process flow of GaP thin film transfer to glass substrate.

Subsequently, the SiO_2 layer was bonded to the glass substrate using UV-curable adhesive NOA61. This process ensured a strong bonding of the GaP film to the glass while maintaining its mechanical support. After the bonding was completed, the GaAs substrate was removed by selective wet etching until the AlGaInP sacrificial layer was exposed. Finally, the AlGaInP layer was removed using a specific chemical etching solution to retain the intact GaP/SiO_2/NOA61/glass structure, resulting in a released high-quality GaP film.

GaP thin films deposited on glass substrates were fabricated to serve as a standardized reference for ultrafast spectroscopic characterization. The objective of this configuration is to provide a baseline for the material's intrinsic third-order nonlinearity and carrier dynamics in the absence of structural resonance or mechanical suspension. By comparing the differential reflectivity signals from these substrate-supported films with those from suspended membranes, we can quantitatively isolate the contributions of local field enhancement and acoustic confinement. This comparative analysis is essential for verifying the performance

gains attributed to the nanophotonic and nanomechanical design of the suspended platform.

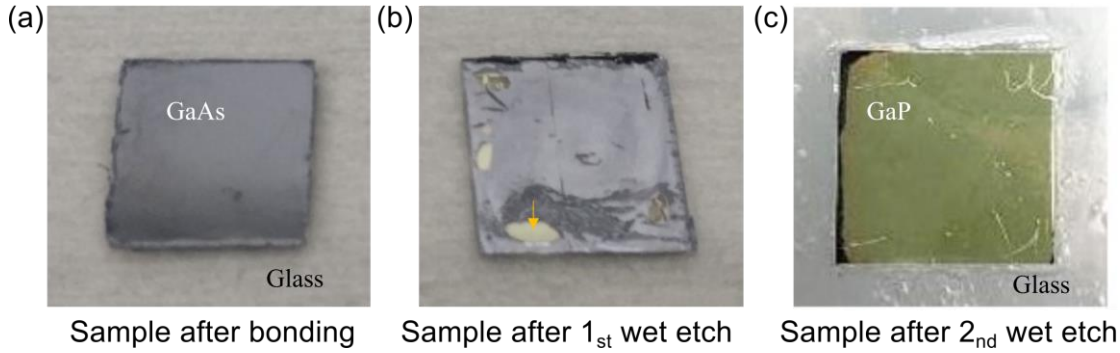

Figure 2.20 Physical photographs of the different stages of the wet etching process. (a) Initial stage, GaAs substrate is completely covered. (b) After the first stage part of GaAs is etched and yellow area appears. (c) Final stage, AlGaInP layer is completely removed and GaP film is revealed.

Figure 2.20 show physical photographs of the key stages of the wet etching process. In the initial stage, the GaAs substrate is covered with the topmost layer, which is overall gray-black and smooth. As the first stage of etching proceeds, some GaAs is removed and localized areas transmit yellow reflections of the structure below, indicating that the etching has reached the AlGaInP layer. In the second stage, GaAs is further removed, while the AlGaInP layer starts to dissolve, and the surface color change is more obvious. Upon completion of the third stage, the AlGaInP is completely removed by etching, revealing the GaP film at the bottom, and its yellow reflection on the glass substrate is clearly visible, indicating the successful completion of the transfer and etching process. Throughout the process, no obvious cracks, scratches or particle contamination were found through optical microscopy, indicating strong bonding and precise

control of wet etching.

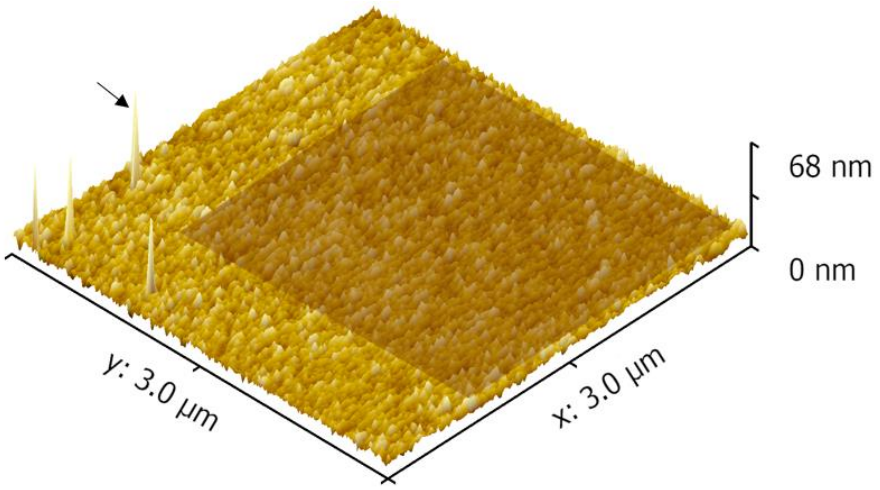

Figure 2.21 AFM 3D surface topography of GaP films transferred to glass substrate.

To further evaluate the surface of the GaP films transferred to the glass substrate during the wet etching and bonding process, we characterized them using an AFM with a scanning range of 3.0 µm × 3.0 µm (Figure 2.21). The measurement results show that the overall height variation of the surface, and the surface morphology features include two main categories: one is the local peaks indicated by arrows, with the maximum undulation of 68 nm, which is presumed to be originated from the local corrosion rate difference during the wet etching process or the stress concentration during the transfer process; and the other is the large flat area, which has an Ra of 1.56 nm, and the RMS is 1.99 nm, which indicates that the overall surface of the film is extremely smooth, and it has reached the surface quality requirements for the fabrication of high-performance optical devices.

We systematically compare the differences in nonlinear optical response of

several suspended GaP thin film device structures using pump-probe ultrafast spectroscopy, with the goal of revealing the effect of structural design on the transient reflectance modulation efficiency and response dynamics. Figure 2.22(a) shows microscope images of several typical structures, including a photoresist grating (PR grating) prepared on the surface of a suspended GaP film, a waveguide (PR waveguide), a uniform photoresist film (PR film on GaP), a bare suspended GaP film, and a glass-based GaP film. The difference between these structures is not only in their geometrical shape, but also in their ability to modulate the mode distribution of the incident pump light, the degree of field localization, and the density of photonic states. Gratings and waveguide structures are able to introduce sub-wavelength periodic refractive index modulation or transverse mode constraints, whereas homogeneous and bare films rely primarily on overall refractive index and film thickness modulation, and glass-based films have little or no localization capability.

To achieve high frequency, ultrafast all-optical modulation, both pump and probe wavelengths are strategically positioned within the material's transparency window. This off resonant excitation scheme is critical to avoid the generation of real photocarriers via linear absorption, which would otherwise introduce long lived carrier induced effects and thermal relaxation bottlenecks that limit the modulation bandwidth. Consequently, this spectral alignment ensures a purely refractive response with picosecond scale recovery times, effectively eliminating the parasitic absorption induced transients that constrain high speed performance.

Figure 2.22(b) shows the transient reflectance change ($\Delta R/R$) versus time delay for different structures at a 775 nm pump and a probe of 600 nm. The most

significant response comes from the PR grating with a peak of about 2.3%, which is significantly higher than the other structures. This enhancement can be attributed to the combined effect of guided-mode resonance (GMR) and diffraction coupling effect, which results in a strong local electric field distribution of the pumped light within the film. The peak for the waveguide structure is about 2.0%, which is slightly lower than that of the grating, but still maintains a high response, with the enhancement coming from the increase in the interaction area due to the longer optical range. The peak for the homogeneous PR film drops to 1.5%, indicating limited enhancement relying only on refractive index perturbation and interface modulation. The bare suspended GaP film has a peak of only 0.5%, reflecting a significant decrease in the pump light modulation efficiency in the absence of any field localization design.

In terms of temporal characteristics, the response curves of the different structures all show a sharp rise on the sub-picosecond scale near the delay time 0 ps, followed by a decay phase on the picosecond scale. This fast component mainly reflects the electronic polarization process under the nonresonant Kerr effect, whose time constant is usually less than 1 ps and is proportional to the pump intensity. Some structures, especially homogeneous and bare films, also show a slower decay component (> 10 ps) after the main peak, which may originate from the refractive index change induced by multiphoton absorption of free carriers or absorption in defect states, with the recovery process being controlled by carrier-phonon scattering and non-radiative complexes. In contrast, the slow component in grating and waveguide structures is relatively weak, suggesting that strongly localized structures are more concentrated on the

electronic polarization process in the pump light energy distribution and excite a lower proportion of long-lived carriers, thus favoring high-speed modulation applications.

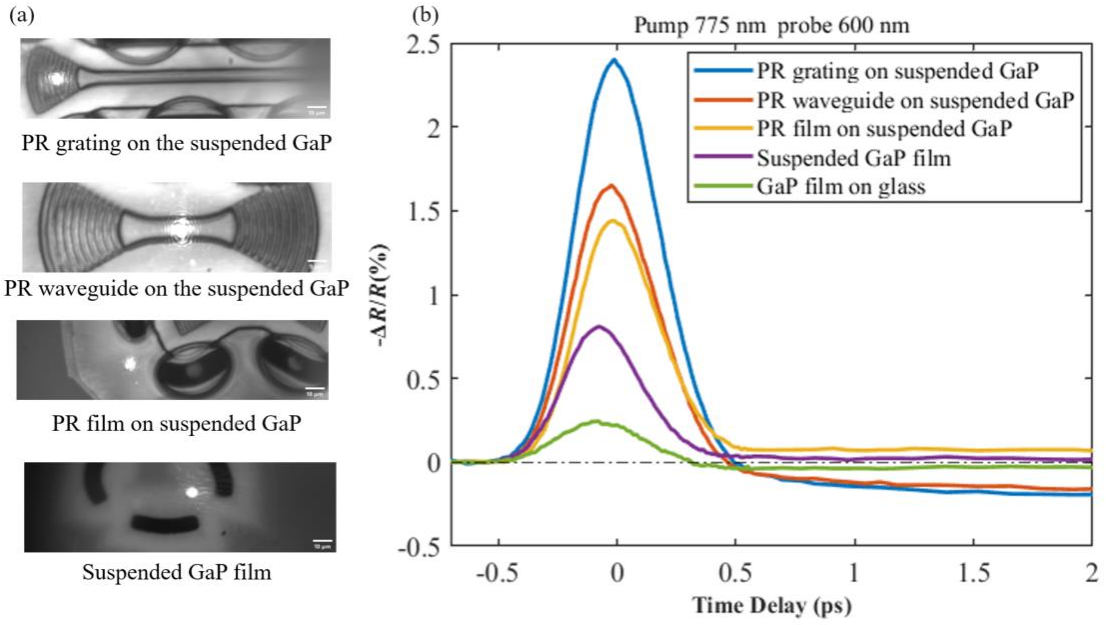

Figure 2.22 (a) Microscopic optical images of different suspended GaP device structures, including PR grating, PR waveguide, PR film, bare suspended GaP film, and glass-based GaP film. (b) Time-delayed transient reflectance change ΔR/R curves for each structure at 775 nm pump and 600 nm probe.

From the perspective of the underlying physical mechanism, the pump wavelength of 775 nm (corresponding to a photon energy of approximately 1.6 eV) is smaller than the direct band gap of GaP (around 2.26 eV), so that electron-hole pairs cannot be generated directly under single-photon absorption channel, and the transient signals are mainly originated from the transient refractive index change due to the nonresonant electron polarization (Kerr effect). However, a

small number of carriers may still be generated under strong pumping conditions through two-photon absorption (TPA) or defect-assisted absorption, and this contribution is more likely to be reflected in the slow decay component. The high field enhancement factor of the grating and waveguide structures (field strength can be boosted to several times the incidence) not only amplifies the Kerr effect contribution, but may also increase the TPA probability in the localized high-intensity region, which provides an explanation for the weak slow component after the main peak. Homogeneous and bare membranes lack this spatial selectivity, and thus the slow component is relatively more significant and decays more slowly.

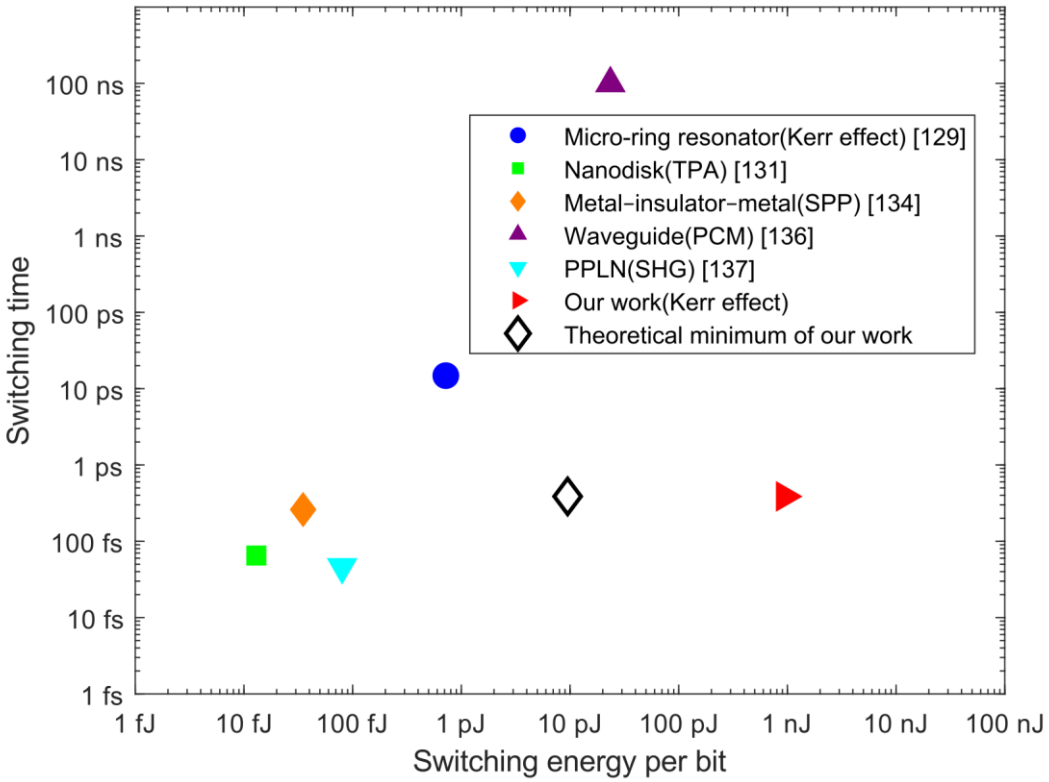

Figure 2.23 Performance distribution of all-optical switches for each type of all-optical switch in the plane of switching energy versus response time. The red dots are the present working suspended GaP thin-film devices, and the black hollow diamonds are the theoretical energy lower limit.

In order to compare the performance of this work with existing all-optical switching devices in a unified framework, we refer to the literature data in Figure 2.23 and organize it into Table 2.2. A distinct balance exists among switching energy, response speed, and switching ratio across various devices. Nanodisk structures can achieve ultrafast response of 10-100 fs based on TPA or Kerr effect, but the device size is small and the energy density is high; metal-insulator-metal MIM structures use surface-isolated exciton polariton (SPP) modes to achieve 1-2 ps switching, but the pumping intensity can be up to the MW/cm^2 level; photonic crystals and micro-ring resonators achieve high switching ratios at lower power through mode localization, but often at the expense of bandwidth and fabrication tolerances. In this work, a Kerr effect switch based on a suspended GaP film achieves a response speed of 387 fs and a switching ratio of 16.4 dB without using a subwavelength localization design, which is in the class of sub-picosecond high-speed modulation devices.

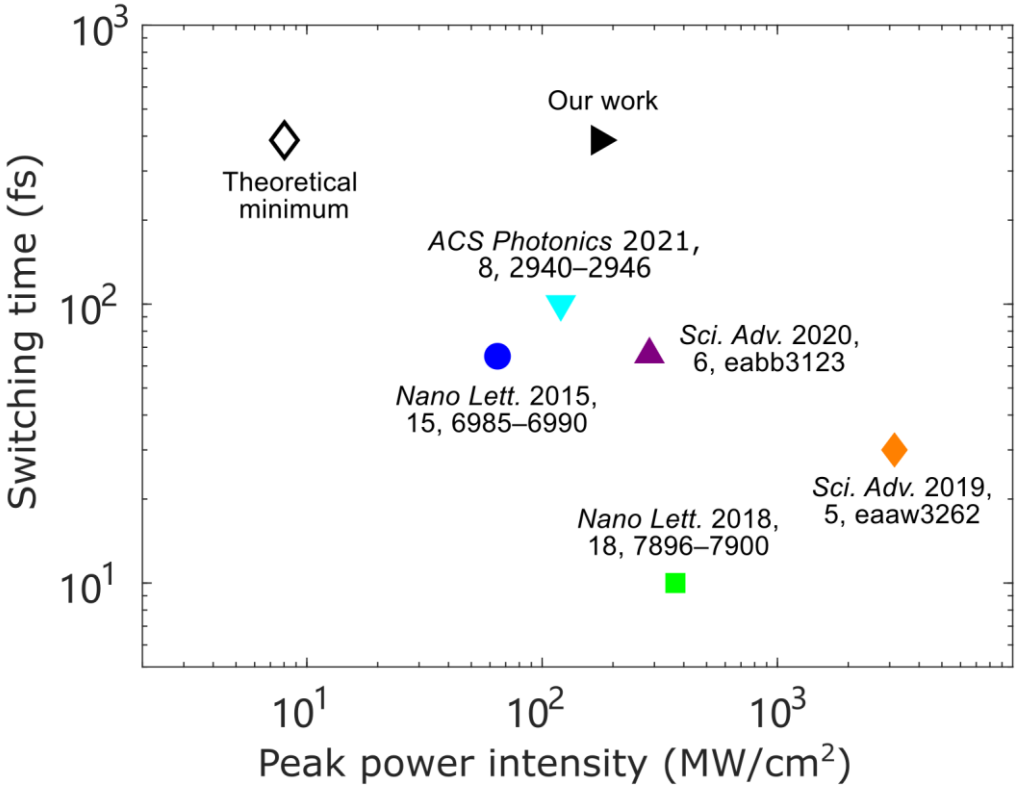

Figure 2.24 Performance distribution of Kerr-type all-optical switches in the plane of peak power intensity versus response time.

However, the switching energy of the present work is 509.7 J/m², which is significantly higher than that of some strongly localized nanostructures. The main reasons for this gap are the large effective mode field volume, insufficient focusing of the pump light, and the lack of resonance enhancement in the structure. The selection of GaP as a nonlinear medium is driven by its ability to support near-instantaneous Kerr effect transitions without the slow free-carrier interference common in other semiconductors.[129] This characteristic enables sub-picosecond modulation speeds, potentially reaching the terahertz regime. In our analysis, we prioritize peak power intensity over integrated switching energy

as the primary performance metric, since the third-order nonlinear refractive index change is directly tied to the instantaneous intensity. As shown in Figure 2.24, our current GaP-based device achieves a switching response in the hundreds of femtoseconds, remaining competitive within the Kerr-type switching landscape. While the current energy requirements are largely dictated by the excitation pulse duration, a clear pathway toward on-chip integration exists. Future improvements will focus on refining nanofabrication to minimize scattering losses and implementing resonant architectures, such as high-Q cavities or anapole-enhanced nanostructures, to maximize light-matter interaction and approach theoretical energy-efficiency limits. The theoretical limits in Table 2.2 (black hollow diamonds) suggest that by introducing gratings, photonic crystals, or equipartitioned excitonic structures on the suspended GaP film, increasing the localized field enhancement factor by several times and reducing the mode volume, it is expected that the energy requirement can be reduced by an order of magnitude or even close to the theoretical limit. This will not only significantly enhance the competitiveness of the devices in energy-sensitive applications, but also help to expand their utility in high-speed optical communications.

Table 2.2 Performance parameter comparison among various all-optical switching architectures.

Structure	Mechanism	Power	Speed	On/off Ratio	Year	ref
Micro-ring resonator	Kerr effect	720 fJ	14.8 ps	23.3 dB	2014	[130]

Micro-ring resonator	TPA	25 mW	25 ps	12.3 dB	2014	[131]
Nanodisk	TPA	13 fJ/disk	65 fs	99.30%	2015	[132]
Photonic crystal	Coupling Modulation	560 kW/cm^2	15 ps	10 dB	2017	[133]
Nanodisk	Kerr effect	28 J/m^2	10 fs	99.70%	2018	[134]
Bulk material	Kerr effect and TPA	220 J/m^2	30 fs	30%	2019	[16]
Nanodisk	Kerr effect and TPA	20 J/m^2	66 fs	60%	2020	[15]
Waveguide	Surface plasmon polaritons	35 fJ/bit	260 fs	3.5	2020	[135]
Bulk material	TPA	26.67 J/m^2	100 fs	73%	2021	[136]
Waveguide	PCM	23.5 pJ	100 ns	23%	2022	[137]
PPLN	SHG	80 fJ	46 fs	3 dB	2022	[138]
Suspended film	Kerr effect	509.7 J/m^2	387 fs	16.4 dB	2024	Our work

In summary, the suspended GaP thin-film devices exhibit remarkable transient reflectivity modulation capability in the sub-picosecond scale, especially the grating and waveguide structures, which significantly enhance the nonlinear response amplitude through field localization and mode modulation. While maintaining the high speed response, future work should focus on reducing the energy requirement and improving the device integration. This can be achieved by introducing high-Q resonant cavities or sub-wavelength photonic structures, which can significantly improve the modulation efficiency while maintaining the ultrafast response, and enable these devices to occupy a more advantageous position in the field of high-speed, low-power all-optical signal

processing.

2.4 Conclusion

This chapter centers on the fabrication, linear and nonlinear optical properties of suspended GaP thin-film devices and their applications in ultrafast all-optical modulation. Firstly, GaP/AlGaInP/GaAs multilayer structures are grown by MOCVD and combined with ICP dry etching and wet release techniques to successfully prepare high-quality suspended GaP waveguides, which achieve the BIC with low-loss TM mode, and the devices exhibit excellent fabrication tolerance under waveguide width and bending radius optimization and bending performance. In the linear optical test, the experimental and finite element simulation trends are consistent, but the overall experimental loss is high due to the material absorption and fabrication roughness; at short wavelengths, the mode area is reduced to lower the loss. In the nonlinear research part, in this work, the two-photon absorption coefficient and nonlinear refractive index of GaP in the 650-850 nm band have been systematically measured using Z-scan technique. The results show that the material exhibits antisaturation absorption and self-focusing behavior at 800 nm. The transient reflection modulation experiments show that, thanks to the field localization effect, the grating and waveguide structures can significantly improve the modulation depth, and the response speed can reach the sub-picosecond level (the fastest is about 387 fs), but the energy consumption is still high. In the future, the introduction of high-Q resonant cavities or sub-wavelength structures is expected to maintain the high-

speed characteristics while effectively reducing energy consumption, thus enhancing the competitiveness of its application in high-speed, low-power all-optical signal processing.

Chapter 3 Suspended GaP Thin Films for Optomechanics

3.1 Introduction

Optomechanics, the generation and control of hypersonic waves upon optical excitation, is seeing tremendous interest for its potential applications, including high-speed communication,[139], [140] sensing,[141], [142] and quantum computing.[143] Compact devices have been achieved with recent advancements in nanostructured optomechanical resonators,[144]–[147] which act as both optical and mechanical resonators, enabling efficient bidirectional electromagnetic-acoustic wave transduction.[148]–[151] When pumped by an intense light pulse above the bandgap or the interband transition threshold, nonradiative decay inside the nanoantennas transfer optical energy to the crystal lattice ultimately, leading to mechanical vibrations of the nanostructure following its normal modes.[152], [153] Detection of such vibrations can be used for fields such as information transfer and environment sensing,[154], [155] which can be emitted as acoustic waves through mechanical coupling. The duration of the acoustic waves serves as an important indicator of the information loss rate into the surrounding medium. Conventional nanoresonators, such as plasmonic antennas fabricated of noble metals, support optomechanical oscillations with the duration of 1 ns - 2.5 ns.[144], [156]

The quality factor (Q) extracted from the vibrational spectrum has been widely used to understand the performance of optomechanical resonators. For

example, the quality factors are observed to attain 10-20 for gold nanoparticles,[157] nanorods,[158] and nanopolyhedrons,[159] 5-10 for aluminum nanodisks[160], [161] and nanoparticles,[162] 7-12 for silver nanocubes[163] and nanowires,[164] and 20 for copper nanowires.[165] Key determinants of Q include the material's crystallinity,[166], [167] the surrounding medium,[168] and the nanostructure's coupling to its substrate.[169], [170] To achieve higher Q values, several strategies such as tailoring resonator morphology,[156] adopting semi-suspended nanostructures,[171] and single-crystal growth[172], [173] have been applied to suppress the energy dissipation. However, the high loss and lack of magnetic modes hinder the applications of metal-based plasmonic optomechanical devices. Notably, all-dielectric materials have emerged as promising nanosystems for the visible-light applications.[174] However, the experimental demonstrations of silicon carbide (SiC) metasurfaces indicate their quality factors remain limited to approximately 2.0, primarily due to geometric constraints and structural design.[175] Similarly, individual GaP nanodisks exhibit quality factors around 6.0, constrained mainly by their mechanical coupling to substrates and acoustic energy leakage.[176] Consequently, dielectric resonators require extra design rules towards the mitigation of vibrational dissipation.

Table 3.1 Summary of reported GHz phononic structures

Structure	Substrate	Size	f (GHz)	Q	Optical response	Acoustic response	Ref
Au film	Glass	Thickness 45 nm	33.6	10	Tunable	Tunable	[177]
Au nanoplate	Glass	Thickness 83.5 nm	19.4	50-60	Not mentioned	Not mentioned	[178]

Au nanorod	Quartz	140*60*35 nm	8.5 (air) 9 (PMMA)	27 14	Not mentioned	Tunable	[141]
Au bipyramids	Colloidal dispersion		27.8	15-20	Tunable	Tunable	[154]
Au metasurface	Sub-5nm tip-supported	Thickness 20 nm	5.27	37	Not mentioned	fixed	[171]
Au nanodisk	Glass	Thickness 35 nm Diameter 70-178 nm	5-20	18.8 ± 2.3	Not mentioned	Tunable	[172]
Au nanowire	Suspended	Diameter 200 nm	13.5	24	Not mentioned	Tunable	[179]
Ag nanowire	Glass	Diameter 62 ± 11 nm Length 2-20 μm	46.8	20.4 ± 4.4	Tunable	Tunable	[180]
Ag nanocubes Ag nanowires	Glass	Side length 35.5 ± 3.4 nm Diameter 40-80 nm	50-55 25-50	19.7 ± 2.9 23.2 ± 6.1	Not mentioned	Tunable	[164]
Cu nanowires	Si Free-standing	Diameter 200 nm	15.6 39.6	80 130	Not mentioned	Tunable	[181]
Cu nanowires	10 um Si membrane	Diameter 400/120 nm Length >10 μm	8.0 ± 0.2 (400 nm) 26.5 ± 0.2 (120 nm)	$Q \approx 20$ (400 nm) $Q \approx 30$ (120 nm)	Not mentioned	Tunable	[165]
Tungsten/Polycarbonate multilayers	Glass	Thickness 2.5-20.2 nm	135	15	Not mentioned	Tunable	[182]
InSe layer	Sapphire/Si	Thickness 63-115 nm	20/60	10/30	Not mentioned	Tunable	[183]
Ni stripes 1D-surface phononic crystal Al nanodisk 2D-surface phononic crystal	Sapphire Si	Period 1058 nm Width 250 nm Height 20 nm Period 1 μm Diameter 350 nm Height 45 nm	6 11.88 5.23 10.43	173 91 91 22	Not mentioned	Tunable	[184]
Polystyrene microspheres + silicon membrane	Suspended	Diameter 1.02 μm Thickness 1.27 μm	1.03	>12	Not mentioned	Tunable	[185]
Si membrane	Free-standing	Thickness 222nm	19	313	Not mentioned	Tunable	[186]
GaP nanoantenna	SiO_2	Diameter 330-580 nm Thickness 125 nm	8-11	6	Tunable	Tunable	[176]

This work	Suspended	Thickness 550 nm	5.22 (n=1) 15.72 (n=3)	65.48 90.38	Tunable	Fixed	

Suspended dielectric structures could be an alternative solution for suppressing energy dissipation, by which the vibrational interactions from supported substrate can be potentially eliminated.[187], [188] Recent reviews have highlighted advances in GHz phononics and the use of ultrafast pump-probe techniques for assessing vibrational modes.[189], [190] Alternatively, in view of the simultaneous modulation of optical and acoustic properties by nanostructures, fixing either the optical resonance or the vibrational mode presents a counterintuitive approach for precisely manipulating hypersonic waves. However, this decoupling strategy remains largely unexplored due to the scarcity of systems supporting unshifted optical or acoustic resonant modes. Notably, geometric complementary (Babinet-inverted) devices has been widely applied to design optical nanometer-thick membranes from isolated nanostructures.[191]–[193] Babinet's principle in electromagnetics[194] predicts that the electric field behind the complementary screen (i.e. a conductor strip) is related to the magnetic field that would exist behind the original screen (slot in a conducting plane), and vice versa, under specific conditions[195]–[197]. This involves an interchange of electric and magnetic field components, reflecting a duality principle.[198] However, this design rule of structure complementarity in the photoacoustic regime, to the best of our knowledge, remains largely unexplored.

In this work, we propose and examine the capability of a suspended GaP fishnet membrane in terms of generating and controlling gigahertz hypersonic

waves. We investigate their optomechanical properties through a combination of finite element method (FEM) simulations and ultrafast pump-probe experiments. Through systematic comparison with conventional disk-based designs, we illustrate how the geometric complements exhibit divergent mechanical responses due to differences boundary conditions in the photoacoustic regime. We demonstrate that the long-lasting hypersonic waves reasonably give rise to an order of magnitude higher quality factor with up to five odd-order vibrational modes. Our discoveries not only identify a subtle yet important limitation of geometric complementarity in the photoacoustic regime but also establish a pathway toward designing high-performance optomechanical devices.

3.2 Methods

3.2.1 Sample fabrication.

The GaP epitaxial film was fabricated on a 4-inch GaAs substrate via MOCVD, with a 200 nm-thick AlGaInP interlayer introduced to alleviate the lattice mismatch between GaP and GaAs. The thickness of the GaP layer was about 550 nm. The surface was nearly perpendicular to the [100] crystal direction and was tilted 15° towards [011]. In the process of device patterning, we used a photoresist (SPR955) with a thickness of about 900 nm and exposure through a laser direct writing device (DWL66+, Heidelberg Instruments). We then transferred the pattern to the GaP layer using a chlorine-based recipe via an inductively coupled plasma (ICP) etcher. The residual photoresist was removed by a 1-methyl-2-pyrrolidone (NMP) solution. Next, we used a buffer oxide

etching solution to remove the AlGaInP sacrificial layer. The underlying GaAs substrate was then removed with an acid etching solution, and a suspended GaP film was finally obtained.

3.2.2 Numerical simulations.

The reflection and absorption properties of the fishnet film were calculated using a commercial FDTD simulation software (Lumerical FDTD-Solutions v.8.24.2387). A single basic cell of the fishnet film structure was selected as the computational domain for the simulation and its surroundings were set as air. Periodic boundary conditions are imposed in all four boundary directions. The structure is illuminated by a linearly polarized plane wave at normal incidence in the wavelength range of 300-800 nm. the refractive index and extinction coefficient of GaP were taken from the relevant literature[199].

The linear elastic response of the system was obtained by solving Navier's equation in the frequency domain using the solid mechanics module of the finite element solver COMSOL Multiphysics 6.2. As a displacement excitation mechanism, a thermal strain ε_{th} is introduced proportional to the lattice temperature increase ΔT_L = 100 K, which satisfies the relation $\varepsilon_{th} = \alpha \Delta T_L$, where α is the linear thermal expansion coefficient. To account for the intrinsic damping effect, an isotropic loss factor η = 0.1 is initially set in the GaP region, and a fixed constraint is imposed on the entire periphery of the computational domain for the boundary conditions.

3.2.3 Reflection measurement.

We measured the reflection of the sample using a custom-built reflection test system, in which spectral information was collected by a spectrometer (Ocean ST). In the experimental setup, a supercontinuum light source (SC-5) was directed onto the sample surface via a 20× objective lens with a numerical aperture of 0.4, producing a focused spot of roughly 20 μm in diameter. The reflection of the sample was obtained by comparing it to a reference mirror with a known reflection spectrum.

3.2.4 Pump-probe experiments.

The laser source used for the pump-detection experiments was a femtosecond laser (PHAROS-10W, Light Conversion) with an output center wavelength of 1030 nm, a pulse width of about 290 fs, and an experimental repetition frequency of 50 kHz. The pump beam and the detection beam were adjusted to 800 nm and 600 nm, respectively, by two optical parametric amplifiers (OPA, ORPHEUS-N and ORPHEUS-F, Light Conversion). The pump and probe beams were adjusted to 800 nm and 600 nm, respectively, by two optical parametric amplifiers (OPA, ORPHEUS-N and ORPHEUS-F, Light Conversion). The pump light was focused into a beta barium borate (BBO) crystal, and the resulting 400 nm second harmonic was modulated by a diaphragm-type light valve (MC2000B-EC, Thorlabs) at a set frequency. The signal corresponding to the modulation frequency was subsequently extracted using a lock-in amplifier (SR860, Stanford Research Systems) to suppress noise at other frequencies. The pump and probe beam were focused onto the sample surface through the same

objective lens (NA = 0.6), with spot radii (e^{-2}) of 1.6 μm and 1.1 μm for the pump and probe beam, respectively, and the average power of the pump beam at the sample was 48.2 μW. A delay stage was set up in the probe light path to change the optical range difference between the pump and probe by adjusting its position.

3.3 Results and discussion

3.3.1 Design of Suspended GaP Fishnet Structures

The exceptional performance of GaP is quantified via the defined Figure of Merit (FOM), which integrates three critical parameters: the thermoelastic conversion efficiency, the photoelastic coupling strength, and the optical absorption cross section as shown in Figure 3.1. While metallic nanostructures exhibit strong light matter interaction, their performance is severely bottlenecked by significant Ohmic losses and thermal dissipation. Conversely, although certain wide bandgap dielectrics offer low parasitic absorption, they often lack the necessary refractive index or photoelastic coefficients to support high-Q optical and acoustic resonances simultaneously. GaP effectively bridges this gap, combining a high refractive index with a broad transparency window and a large acousto-optic coefficient.

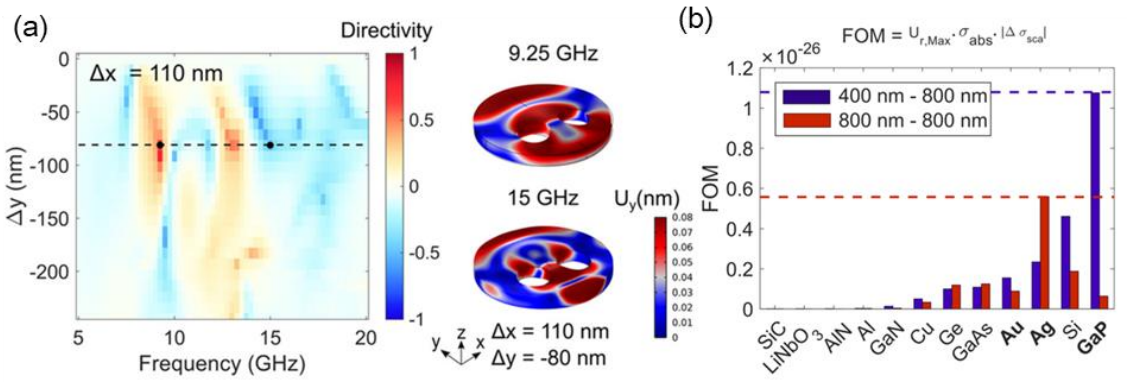

Figure 3.1 (a) The antenna emits vibration at two opposite directions at 9.25 GHz and at 15 GHz. (b) Proposed FOM for both plasmonic and dielectric materials at their optimal radii (below 300 nm).[174]

Figure 3.2(a) displays our design of the suspended GaP fishnet membrane thin film, featuring a hole diameter $D = 3.05\,\mu m$ and a thickness $T = 550\,nm$. The SEM image of the film in Figure 3.2(b) illustrates the top-view of the crystalline GaP fishnet membrane. This film is suspended by removing a sacrificial 200 nm thick AlGaInP layer on top of a 350-μm-thick gallium arsenide (GaAs) substrate, which was partially removed (see fabrication details in the Methods section). The structure consists of a periodic array of circular holes with a period of 4 μm throughout this work.

The adoption of a fishnet architecture, arranged in a staggered square lattice, is driven by the need to decouple optical and acoustic resonances. Unlike conventional nanodisk arrays where lateral geometry simultaneously dictates both optical and mechanical responses, the fishnet membrane supports thickness-dominated acoustic modes. These modes are primarily governed by film thickness and elastic properties, allowing the optical resonance to be independently tuned

via in-plane parameters.

Beyond functional decoupling, this structure serves as a platform to investigate Babinet's principle within a coupled photoacoustic framework. While Babinet-inverted geometries (such as hole and disk arrays) may exhibit complementary optical far-field patterns, our analysis reveals a significant divergence in their mechanical behavior. Due to the vectorial nature of elastic waves, the continuous fishnet membrane suppresses lateral phonon leakage and supports long-lived thickness modes that are not present in discrete disk systems. This 'functional asymmetry' underscores that while optical duality may hold, the mechanical boundary conditions in the photoacoustic regime do not follow simple Babinet reasoning. Consequently, the fishnet design provides a robust strategy for creating acoustic filters where optical excitation and mechanical frequency can be optimized separately.

The linear optical response of the fabricated GaP fishnet membrane is shown in Figure 3.2(c), which is computed by the FDTD method (see numerical simulations in the Methods section). The simulated reflectance (solid line), absorptance (shaded region), and experimental reflectance (circles) of our devices are plotted as functions of the wavelength. The custom-built reflection measurement setup was in the Methods section. The observed peaks and dips in the reflectance spectrum can be due to interference of the multiple reflected light beams. While the simulated and experimental results are generally consistent, minor discrepancies can primarily be attributed to surface roughness and imperfections at the hole edges introduced during fabrication. Figure 3.2(d) shows the normalized power density for the 400 nm pump in the *xy* and *xz* cross

sections. The top view reveals that absorption is strongly localized at the perimeters of the holes. The cross-sectional view further indicates that the absorption is concentrated near the top surface of the membrane and sidewalls of the holes, highlighting the role of surface-enhanced resonances.

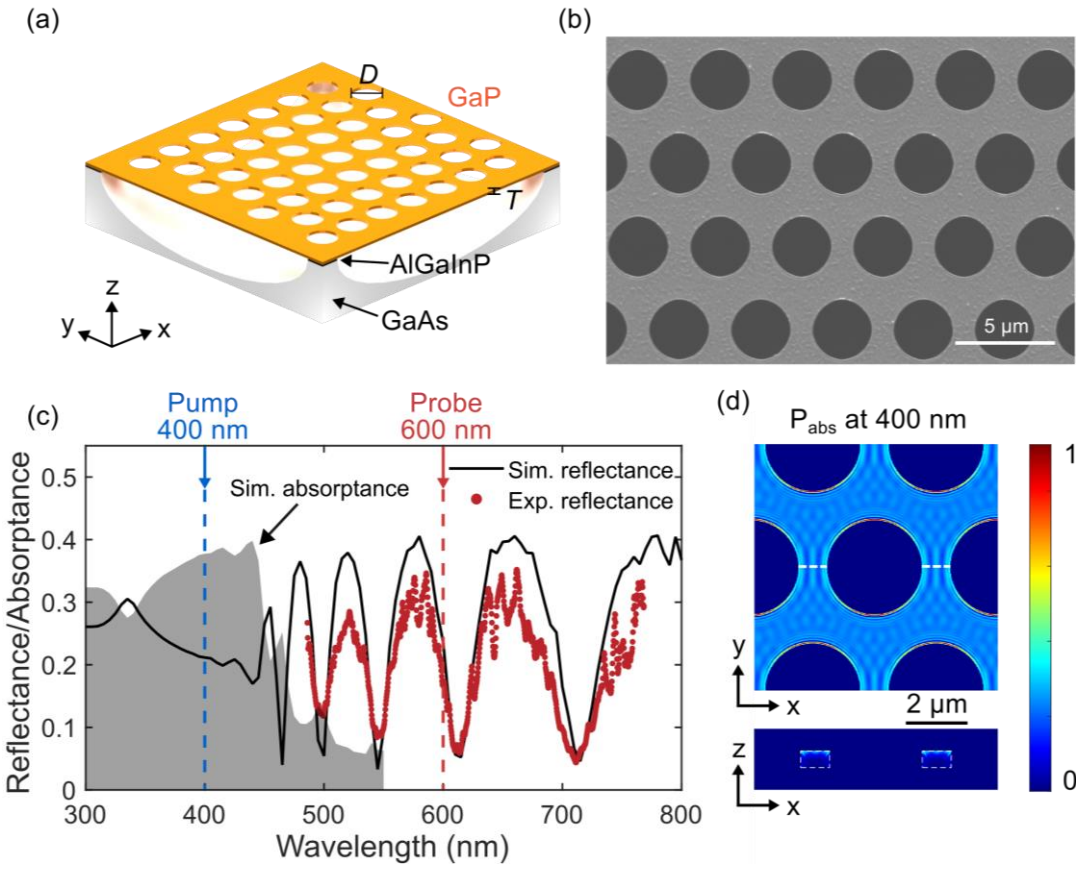

Figure 3.2 GaP fishnet membrane design and linear optical response of the structure. (a) The schematic view and (b) SEM image of the device where the hole diameter D is 3.05 μm, the period is 4 μm and the thickness T is 550 nm. (c) Simulated reflectance (solid line), absorptance (shaded region) and experimental reflectance (circles) of the fishnet membrane as functions of the wavelength. The blue and red arrows indicate that 400 nm and 600 nm are used for the pump and

probe wavelengths. (d) The normalized power density of *xy*-plane and *xz*-plane when the wavelength is 400 nm, with the *xy*-plane taken near the upper surface and the *xz*-plane taken at the middle of the unit structure.

We simulated and compared the frequency domain distributions of the displacement of the fishnet membrane for different hole diameters which can be seen in Figure 3.5(a). Despite the variation in geometry, two distinct resonant peaks consistently appear at approximately 5.2 GHz and 16.2 GHz, which is the fundamental and the n = 3 mode, respectively. Further studies indicate that the vibrational modes are effectively fixed, which reflects a decoupling between the optical excitation and the acoustic response (Figure 3.3). Figure 3.5(b) and (c) present instants of maximum deformation (expansion and contraction) details of the two resonant modes. Both modes remain localized between the holes from the top view, corresponding to an out-of-plane mode and its higher-order mode. The two modes can be assigned from the cross-section view, highlighting the out-of-plane nature. We hypothesis that the unshifted resonances could be due to either the loss of complementarity (switching from the disk array to the hole array) or the mechanical support from the substrates.

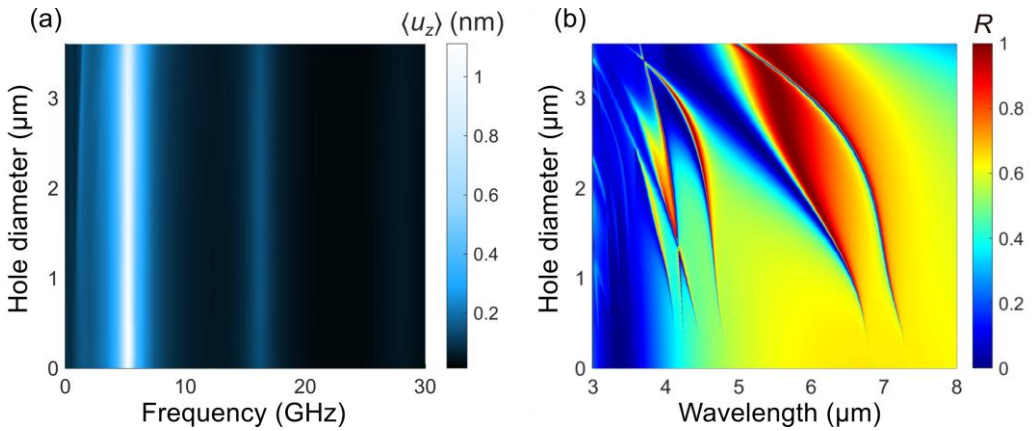

Figure 3.3 Optical and acoustic response of the fishnet membrane. (a) Simulation in the frequency domain of the mean displacement along the z-direction for holes of different diameters. (b) Reflectance spectra with wavelength and hole diameter. The decoupling between the optical and acoustic response is achieved by fixing the vibration mode.

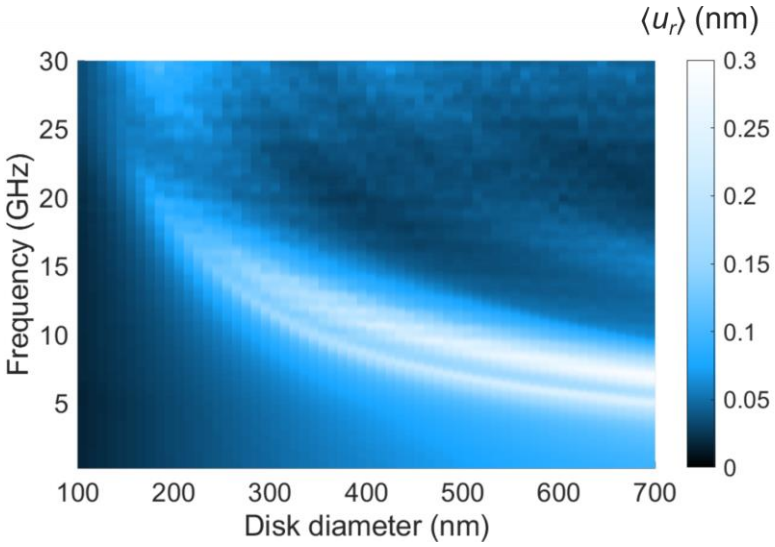

Figure 3.4 Verification of simulation accuracy. Our simulation results show excellent agreement with those reported in the reference,[176] demonstrating the accuracy and validity of our simulation model.

To further identify the origin of the unshifted resonances, we conducted a comparative study involving four types of structures in Figure 3.6(a): (i) GaP disk array with a silica substrate, (ii) GaP disk array without any substrate, (iii) GaP hole array with a silica substrate, and (iv) GaP hole array without any substrate (our design). The total thickness/height of all the four structures (the yellow parts in Figure 3.6(a)) was set to 550 nm, with the disk on suspended thin

films having a film thickness and disk height of 275 nm each. Figure 3.6(b) presents the dependence of the fundamental mode's resonant frequency on the disk or hole diameter for four structural types. We validated our simulation results by comparing them with those from the reference (Figure 3.4).[176]

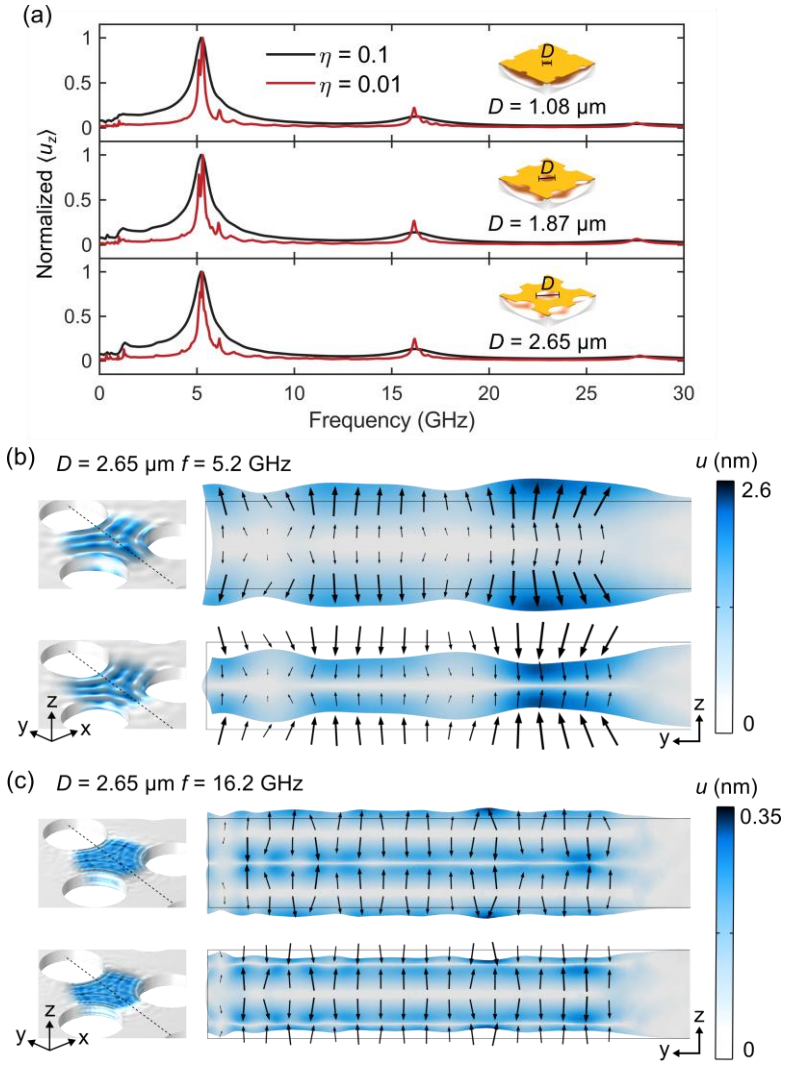

Figure 3.5 Numerical photoacoustic response of the fishnet membrane. (a) The simulated frequency domain of the displacement of the devices with three different hole diameters, 1.08 μm, 1.87 μm, and 2.65 μm, respectively, when the

thickness of the film is 550 nm. The left image presents a 3D representation, while the right image displays cross-sections of the displacement field for the fundamental mode (b) and the n = 3 mode (c). To enhance visibility, the deformation was magnified by 60× (b) and 200× (c).

For structures (i) and (ii), with the disk diameter increased, both peak frequencies exhibit a drastic decrease from 13.0 GHz to around 5.2 GHz. The resonances have a slight red shift when the substrate is removed. At smaller disk dimensions, minor geometric changes significantly alter the mass-stiffness ratio, leading to substantial shifts in the resonant frequency. However, as the disk size increases, further dimensional scaling has a minimal impact on the mechanical properties, and the resonance tends to converge. This results in a stable frequency despite further increases in the disk size, illustrating the balance between boundary conditions, mass, and material elasticity in determining the resonant behavior.

In contrast, a fixed hypersound frequency around 5.2 GHz is observed across different hole sizes for structures (iii) and (iv)s. This unaffected resonance appears both with and without the silica substrate and by any changes in the hole diameter. The displacement distributions for both hole structures in Figure 3.6(e) and (f) show that the mode is dominated by the out-of-plane vibration. However, these are in sharp contrast with the complementary disks, which exhibit redshift in the resonant frequencies as their diameters increase. As shown in Figure 3.6(c) and (d), the deformation of the disk structures is composed of a combination of in-plane and out-of-plane vibration modes, with in-plane displacement

highlighted by the red arrows. The in-plane breathing mode becomes less evident with increasing diameters and less coupled with the out-of-plane mode.

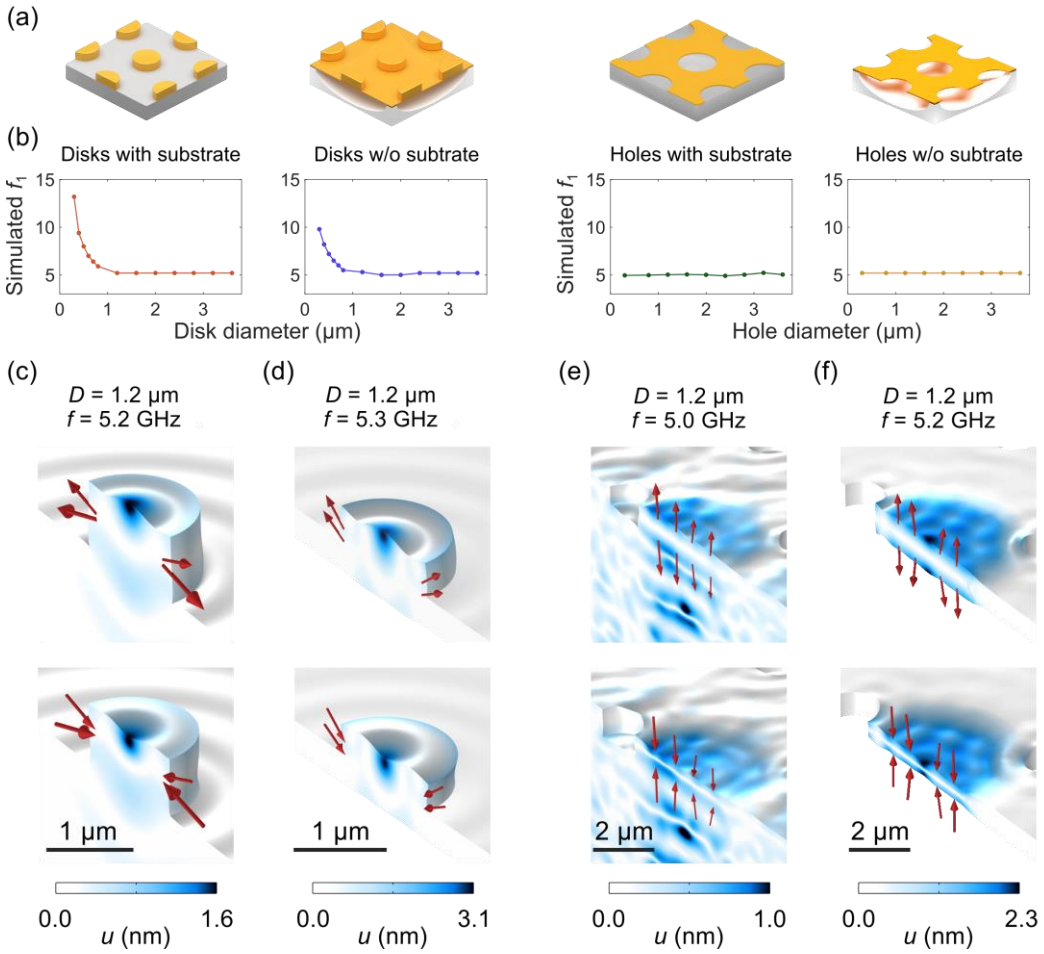

Figure 3.6 Numerical analysis of the fundamental resonant mode. (a) Schematic of the four types of structures. (b) Frequency variation of the fundamental resonant mode with the disk/hole diameter for the four types of structures. (c-f) Calculated deformation geometries at the fundamental resonance of the four different structures when the diameter is 1.2 μm. The upper and lower panels depict images captured at the moments of maximum expansion and contraction,

respectively. A scale factor of 50× (c), 20× (d),150× (e), and 60× (f) was applied to enhance the visibility of deformation.

3.3.2 Mode Analysis and Quality Factor Enhancement

As illustrated in Figure 3.7(a), an ultrafast pump–probe system was utilized to characterize the optomechanical behavior of the suspended GaP fishnet membrane, thereby verifying the simulation predictions. The experiment used a femtosecond laser at a 50 kHz repetition rate, with a 400 nm pump beam to ensure significant above-bandgap absorption and a 600 nm probe beam chosen for its position on the sharp reflection slope in Figure 3.2(c). The pump beam had an average power of 48.2 μW at the sample site. (see more details in the Methods section). Figure 3.7(b) shows the reflectance change ($\Delta R/R$) of the GaP devices with D = 2.26 μm. An initial sharp increase is observed immediately after photoexcitation, attributed to photogenerated free carriers, followed by picosecond relaxation processes. The red line in Figure 3.7(b) shows a tri-exponential decay fit to the original data. On nanosecond timescales, periodic oscillations arise from coherent acoustic phonons induced by transient thermoelastic expansion of the suspended membrane.

The GaP fishnet membrane demonstrates accelerated carrier decay primarily due to the surface recombination and defect-mediated relaxation under optical excitation. Our tri-exponential fitting (Eq. 1) effectively isolates the fishnet membrane's acoustic response by excluding these rapid carrier dynamics.

$$\frac{\Delta R}{R}(t) = y_0 + A_1 e^{-t/\tau_1} + A_2 e^{-t/\tau_2} + A_3 e^{-t/\tau_3} \tag{3.1}$$

In our analysis, A_1, A_2, and A_3 represent the respective magnitudes of the exponential terms, while τ_1, τ_2, and τ_3 denote their characteristic decay times, with t being the time variable.

Table 3.2 Summary of fitting parameters extracted from the tri-exponential analysis of Figure 3.7(b).

y_0	A_1	τ_1 (ps)	A_2	τ_2 (ps)	A_3	τ_3 (ps)
0.0224	-1.44e-3	2637.54	-1.43e-3	2637.56	-1.44e-3	2637.55

In Figure 3.7(c), the residual signal obtained by subtracting the tri-exponential fit from the original signal (time zero corresponding to the peak reflectance change) is shown. Figure 3.7(d) presents the residual signal processed with a 3.0 GHz high-pass filter and fitted with a dual-damped sinusoidal model in the following equation.

$$\frac{\Delta R}{R}(t) = A_1 \cdot e^{-\frac{x}{\tau_1}} \cdot \cos\left(2\pi \frac{x}{T_1} - \phi_1\right) + A_3 \cdot e^{-\frac{x}{\tau_3}} \cdot \cos\left(2\pi \frac{x}{T_3} - \phi_3\right) \qquad (3.2)$$

where $\Delta R/R$(t) represents the transient reflectivity signal, A_1 and A_3 are the initial amplitudes of the two vibrational modes, τ_1 and τ_3 are the decay time constants, T_1 and T_3 are the oscillation periods, and ϕ_1 and ϕ_3 are the phase offsets. The two terms respectively correspond to the fundamental and n = 3 localized vibrational modes. The two dominant vibrational modes were fitted to the model with periods T_1 = 191.53 ps and T_3 = 63.63 ps, and damping times τ_1 = 3992.35 ps and τ_3 = 1830.64 ps. Such results yield quality factors of $Q_1 = \pi\tau_1/T_1 \approx 65.48$ and $Q_3 = \pi\tau_3/T_3 \approx 90.38$. The corresponding fast Fourier transform (FFT) spectrum, shown in Fig. 3.6e, reveals resonance frequencies f_1 = 5.22 GHz and f_3

= 15.72 GHz, consistent with the time-domain fittings, validating the reliability of our analysis. Additionally, by using a 15.0 GHz high-pass filter, we extracted a resonant signal near 15.72 GHz (Figure 3.8). It is noteworthy that only odd-order modes are typically observed in such transient reflectance measurements, as they are associated with symmetric thickness oscillations that lead to volume changes and thus stronger optical modulation.[200]

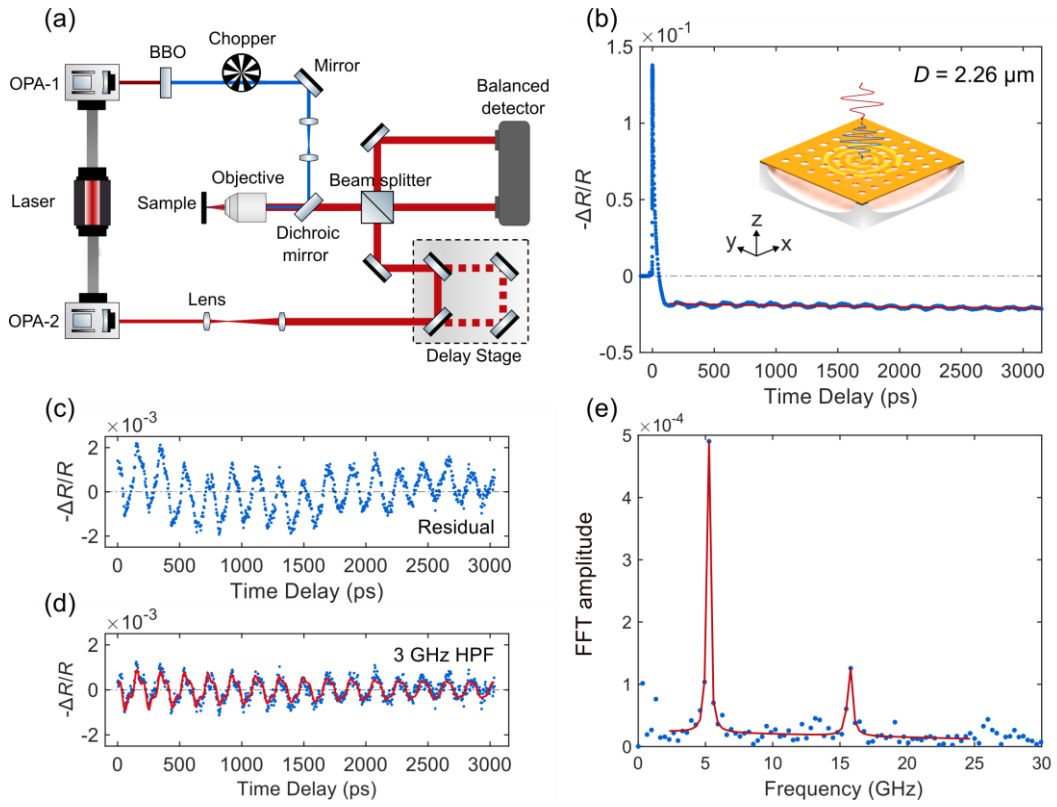

Figure 3.7 Experimental optomechanical response on the GaP fishnet membrane. (a) The ultrafast pump-probe system. OPA: optical parametric amplifier, BBO: beta barium borate. (b) Experimental reflectance change ($\Delta R/R$) of the fishnet membrane. The red line shows a fitted tri-exponential decay to the original data. The inset illustrates the pump-probe experiment conducted on the GaP fishnet

membrane. (c) The residual signal after subtracting the tri-exponential fit, where a significant oscillation can be observed. (d) The optomechanical response spectrum of the fishnet membrane after applying a 3.0 GHz high-pass filter. The red line is a dual-damped attenuated sinusoidal function fit. (e) FFT spectra of the signal in (d). The red line represents Lorentzian fits for the n = 1 and n = 3 resonant modes.

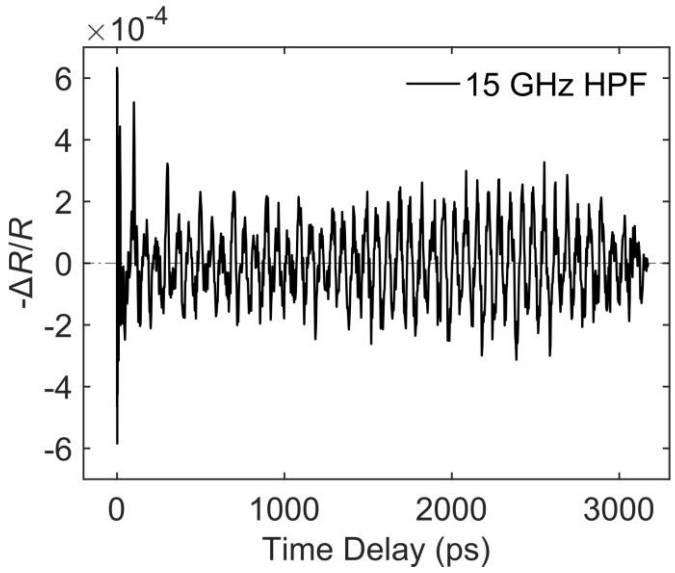

Figure 3.8 The signal was obtained by applying a 15.0 GHz high-pass filter after subtracting a tri-exponential fit from the original signal (with time zero corresponding to the peak reflectance change). This confirms a periodic resonant signal with a dominant frequency near 15.72 GHz.

In order to control the resonance of this localized surface acoustic wave, Figure 3.9 compares the hole diameter dependency and thickness dependency. The simulated *z*-direction displacement magnitude is displayed with the hole

diameter and frequency. The experimentally observed n = 1 and n = 3 resonant frequencies are also marked in the figure, with the error bars (with a factor of five to enhance visibility) representing the FWHMs of the resonant peaks in the FFT analysis. The dashed lines show that the simulation results of the disk arrays. As previously mentioned, the resonant modes in the fishnet membrane are primarily confined longitudinally, making the sample thickness an effective knob to modulate the resonant frequency. The simulated *z*-direction displacement magnitude as a function of the thin-film thickness and frequency is shown in Figure 3.9(b). Consistent with the simulation, our experiments also reveal that the resonant frequency increases as the thickness decreases. In the experiments, we were able to observe only two resonant frequencies, as resonant modes with higher frequency were obscured by noise due to their lowering amplitudes. Notably, we observed up to five resonant modes in the FFT analysis for $D = 1.87$ μm and $T = 550$ nm (Figure 3.10). This is likely due to the enhanced confinement of the resonant modes and an improved signal-to-noise ratio under these conditions.

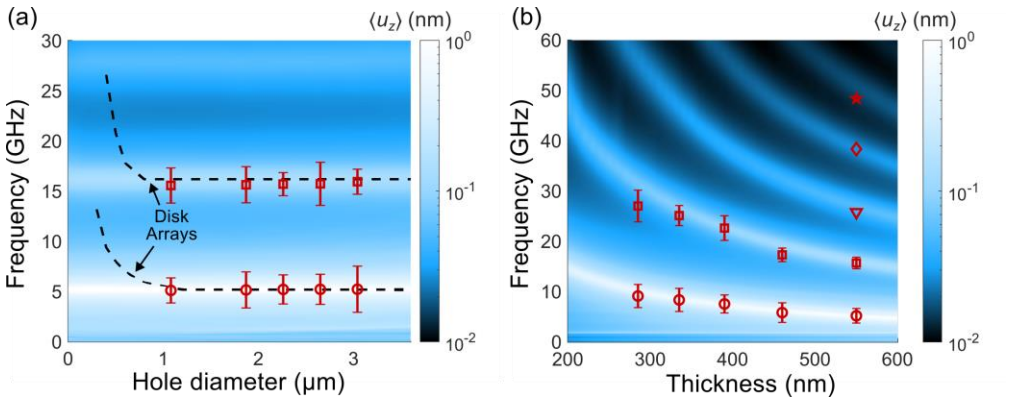

Figure 3.9 Resonance control by geometry of the fishnet membrane. Frequency-domain analysis of mean *z*-axis displacement for various hole diameters at $T =$

550 nm (a) and film thicknesses (D = 2.26 μm) (b), respectively. The circle and square dots represent the fundamental and n = 3 resonant modes measured in our experiments, and the error bars (with a factor of five to enhance visibility) represent the FWHMs obtained by fitting over the frequency domain. The classical prediction (dashed line) is derived from the simulation results of the disk arrays.

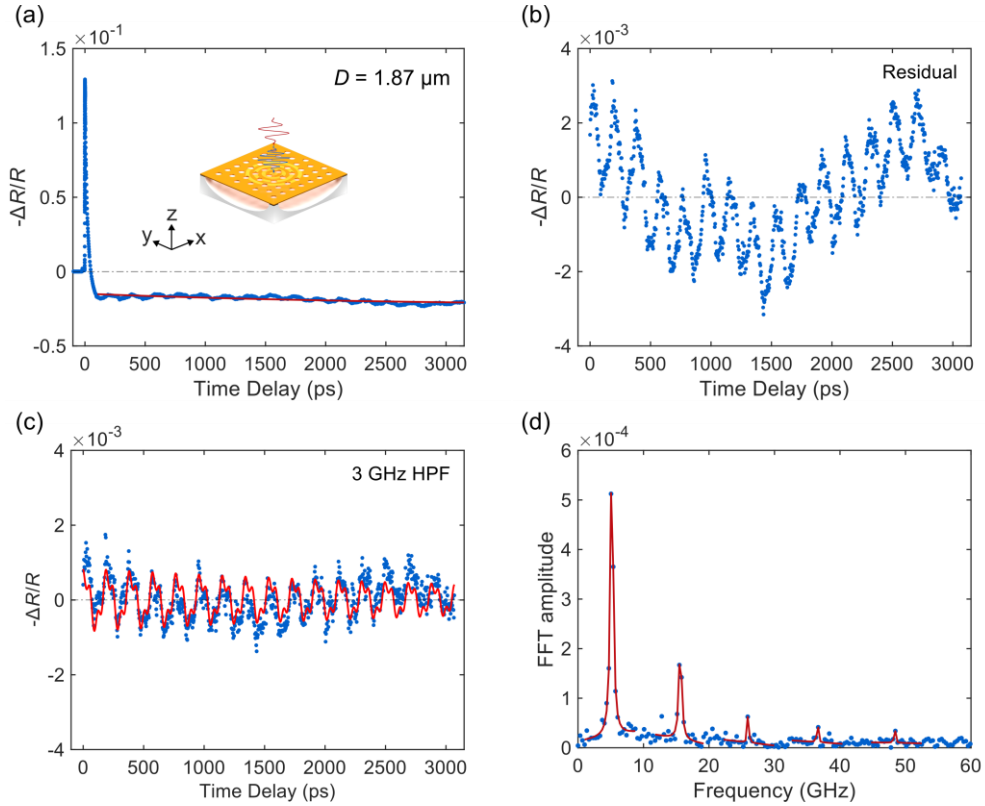

Figure 3.10 Detection of multiple resonant modes. (a) Experimental differential probe reflection signals ($\Delta R/R$) of the fishnet membrane with the hole diameter of 1.87 μm and a thickness of 550 nm. The red line shows a fitted tri-exponential decay plus attenuated sinusoidal model to the original data. (b) The residual

signal after background subtraction, where a significant oscillation can be observed. (c) Optomechanical response of the fishnet membrane reflection modes after applying a 3 GHz high-pass filter. The red line is an attenuated sinusoidal function fit. (d) The FFT spectrum of the signal in (c).

To further validate the simulated mode localization and experimental reproducibility, spatially resolved pump-probe measurements were performed by varying pump-probe distances and detecting different positions across the device. On one hand, the observed rapid decay of oscillation amplitude and FFT intensity with increasing distance confirms that the vibrational modes are highly localized, rather than propagating through the membrane (Figure 3.11). On the other hand, resonant frequencies measured across the device surface are found to be 5.22 ± 0.04 GHz and 15.76 ± 0.16 GHz, while corresponding quality factors of Q_1 = 55.64 ± 13.57 (fundamental mode) and Q_3 = 252.56 ± 197.37 (n = 3 mode) (Figure 3.12). Given that photoresist residues at hole edges and increased surface roughness of the GaP are plausible sources of fabrication imperfections, the observed variation in Q-values is likely attributed to local structural inhomogeneities (see SEM image in Figure 3.2(b)).

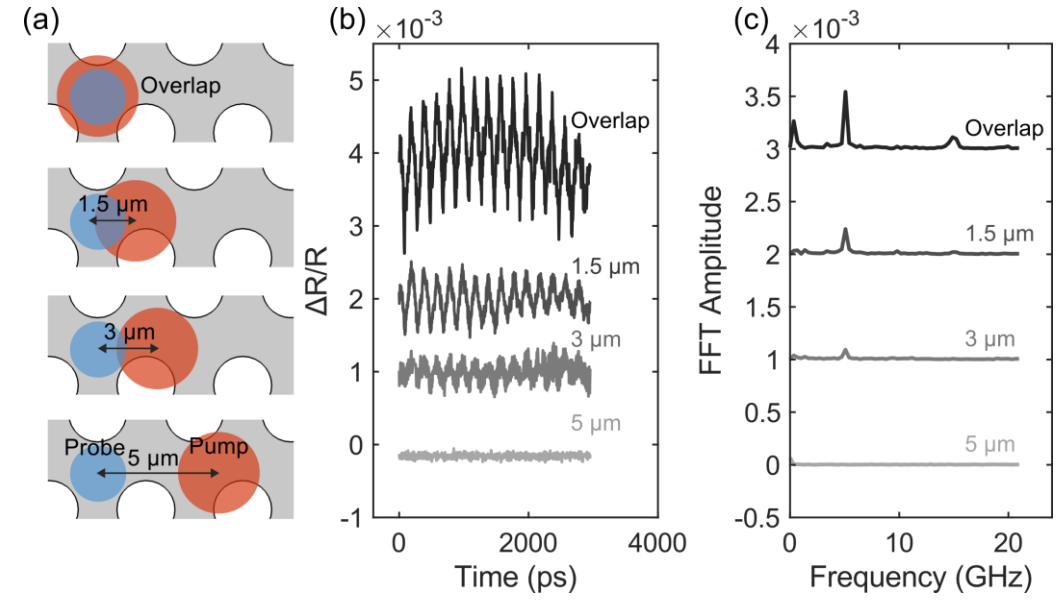

Figure 3.11 Spatially resolved pump-probe measurements demonstrate acoustic mode localization. (a) Schematic of pump and probe beam configurations with varying spatial separations. (b) Time-domain reflectance change signals measured at different pump-probe distances, showing reduced oscillation amplitude as the distance increases. (c) Corresponding FFT spectra indicating the suppression of resonant signals.

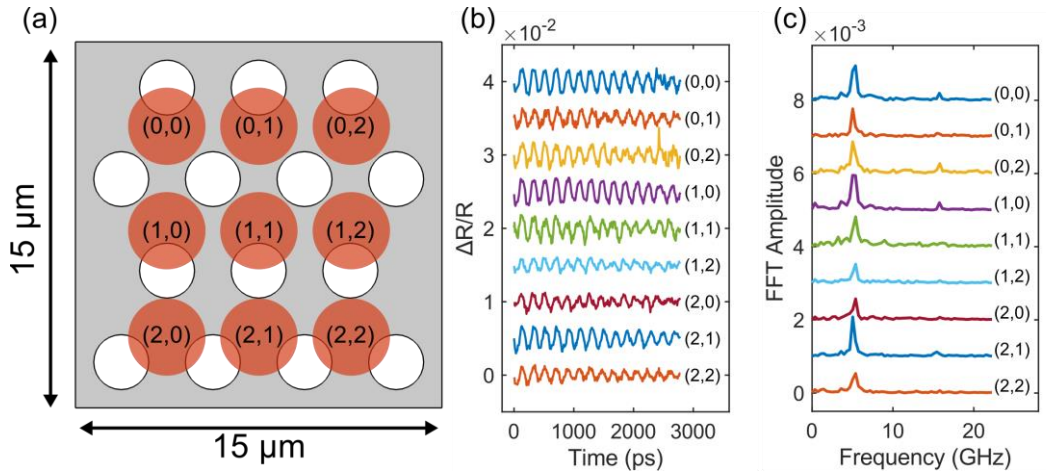

Figure 3.12 Spatial pump-probe scan of the device. (a) Schematic diagram labeling the different scanning regions. (b) Time-domain curves for each region (misaligned for ease of viewing). (c) FFT spectra of the corresponding regions (also misaligned).

Table 3.3 Spatial distribution of resonance frequencies and Q factors calculated by equation (R1) across different unit cells within the same suspended membrane.

	(0,0)	(0,1)	(0,2)	(1,0)	(1,1)	(1,2)	(2,0)	(2,1)	(2,2)	Avg ± SD
f_1	5.21	5.24	5.16	5.19	5.25	5.25	5.27	5.19	5.24	5.22 ± 0.04
f_3	15.83	15.81	15.70	15.75	16.00	15.81	15.73	15.40	15.79	15.76 ± 0.16
Q_1	68.14	47.27	62.96	82.52	52.34	43.21	42.25	57.88	44.68	55.69 ± 13.57
Q_3	610.16	94.92	506.94	227.01	77.62	351.15	217.02	63.73	124.75	252.59 ± 197.38

Our experimental results presented in Figure 3.7 and Figure 3.9 show close agreement with numerical simulations using a damping parameter of $\eta = 0.01$ (Figure 3.13). Although $\eta = 0.1$ was adopted in previous study[150], it yields a quality factor of only ~6, which is approximately one order of magnitude lower than our Q-values. The high Q-factors observed in our system can be attributed to the intrinsic material properties of GaP, its strong covalent bonding and low anharmonicity, which suppress phonon-phonon scattering[201] as well as the suspended membrane architecture, which effectively minimizes substrate-induced damping and other extrinsic loss channels. Some features in Figure 3.6

may suggest mode splitting, however, due to the limitation of our current measurement resolution, this observation remains inconclusive and warrants further investigation.

To investigate the mechanical dissipation in our GaP resonators, all experiments were performed under ambient conditions at room temperature. The loss factor η utilized in our simulations serves as an effective phenomenological parameter that accounts for the cumulative energy dissipation from all channels, including material damping, air resistance, and boundary leakage. By matching the experimental resonant linewidths with our frequency-domain model, we estimated the effective η for the devices.

Our analysis indicates that the Q factors are primarily governed by intrinsic material loss rather than external damping. Spatially resolved pump–probe measurements confirm that the acoustic modes are highly localized within the suspended membrane, with minimal energy leakage to the substrate, thereby ruling out clamping loss as a dominant factor. Furthermore, the observation that the fishnet structures maintain Q factors comparable to unpatterned films, suggests that air damping is secondary to internal dissipation mechanisms, such as phonon–phonon scattering and internal friction within the crystalline GaP. Future work involving vacuum-based measurements and surface passivation will aim to further decouple these intrinsic loss channels and approach the theoretical limits of GaP-based acoustic resonators.

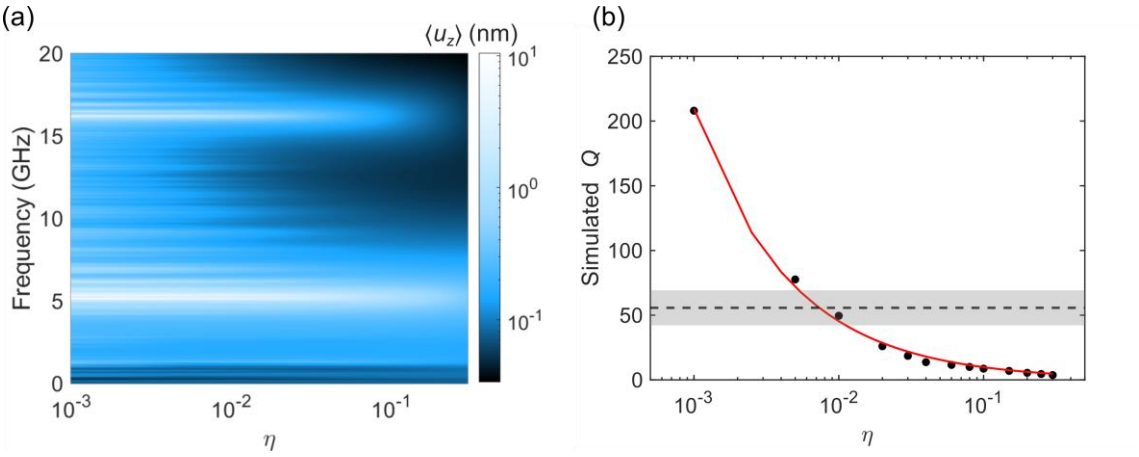

Figure 3.13 Frequency Domain Simulation and Parameter Analysis. (a) Simulation of the average displacement of a 2.26 μm diameter, 550 nm thickness, 4 μm period disk in z-direction with different loss factors η. At high η, there is only a single resonance peak; as η decreases, the resonance peak splits into multiple peaks with narrower peaks and larger amplitudes. (b) Simulated Q of the fundamental mode as a function of η, together with a power-law fit (red curve). The gray shaded region marks the experimentally measured Q value (55.69 ± 13.57), indicating that the actual η is approximately 0.01.

We also numerically evaluated the robustness of the photoacoustic resonance for environmental influences such as temperature fluctuations and changes in the surrounding medium. Simulations and material property analysis (Figure 3.14) indicate that the resonance frequency varies by approximately 3.4% over the temperature vary from -100 °C to 100 °C. Meanwhile, our device exhibits environment-dependent damping accompanied by slight frequency shifts, as confirmed by our simulations (Figure 3.15). These findings are

consistent with previous reports, which also highlight enhanced damping in denser or encapsulated environments[158], [202], [203].

The comparative study of vibrational modes under air and SiO_2 cladding is intended to benchmark device performance across diverse operational environments and interface conditions. While experimental results reveal distinct shifts in mechanical Q-factors and resonance frequencies, it is acknowledged that the current computational model predominantly accounts for solid state elastic boundary conditions. Consequently, the influence of fluid structure interaction and radiation damping into the surrounding gaseous or liquid media is not yet fully incorporated. Addressing these hydrodynamic effects represents a critical direction for future model optimization, which will enable more precise predictions of acoustic dissipation in complex micro fluidic or atmospheric integrated photonic systems.

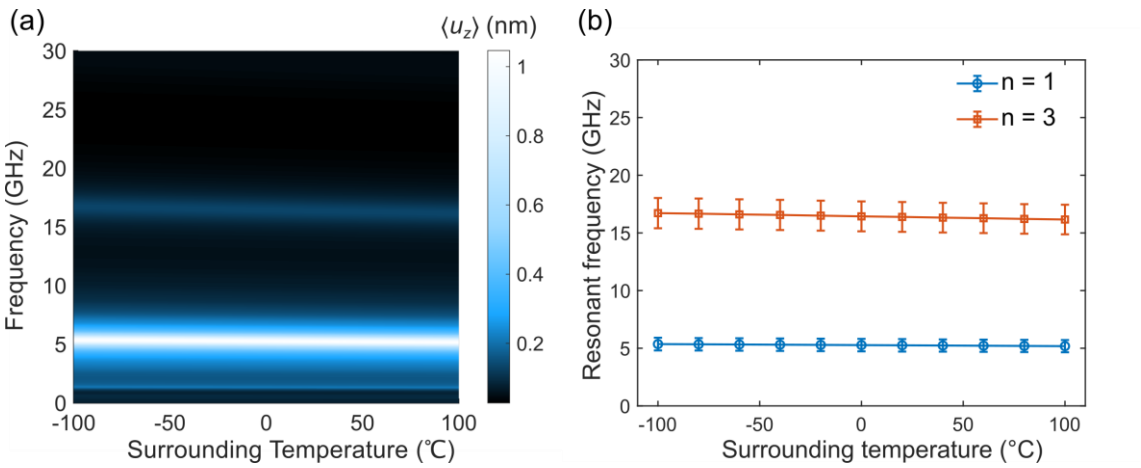

Figure 3.14 (a) Simulated vibrational spectra of the suspended GaP fishnet membrane under varying surrounding temperatures from -100 °C to 100 °C, showing stable resonance peaks for both the fundamental (n = 1) and n = 3

resonant modes. (b) Extracted resonance frequencies of the two modes with temperatures, showing minimal frequency shift across the entire temperature range. Error bars represent the FWHMs obtained by fitting over the frequency domain .

The Young's modulus E(T) decreases approximately linearly with temperature and can be expressed as:

$$E(T) = E_0 \cdot \left(1 + \alpha_E \cdot (T - T_0)\right) \tag{3.3}$$

where E_0 represents the Young's modulus at reference T_0 (taken as 25°C), and α_E is the temperature coefficient of elasticity for GaP, approximately -2 × 10^{-4}/K.

Meanwhile, the density ρ(T) changes minimally with temperature due to GaP's small thermal expansion, following:

$$\rho(T) = \rho_0 \cdot \left(1 - 3 \cdot \alpha_L \cdot (T - T_0)\right) \tag{3.4}$$

where ρ_0 is the density at T_0, and α_L is the linear thermal expansion coefficient, approximately 4.65 × 10^{-6}/K. Given the small value of α_L, density variations are negligible over the examined temperature range.

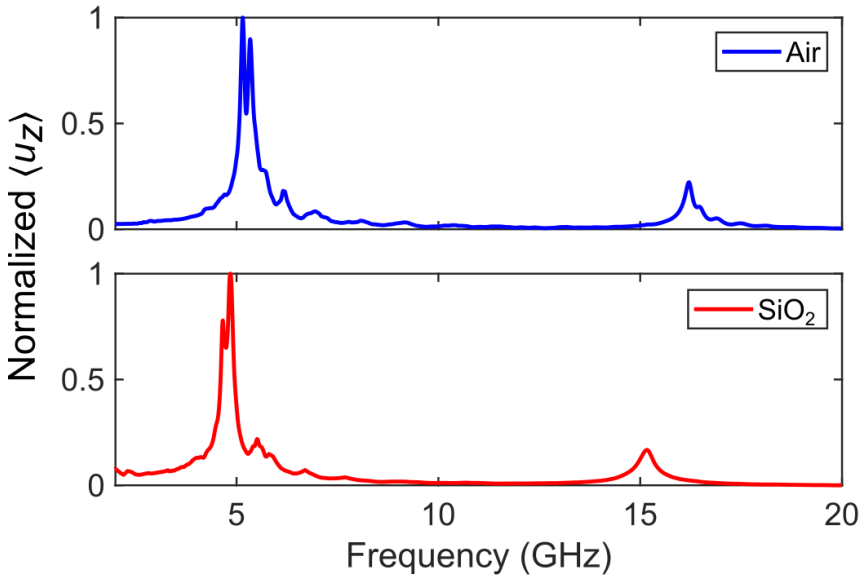

Figure 3.15 Simulated normalized displacement spectra of the GaP fishnet membrane in air and SiO_2.

Table 3.4 Comparison of dominant vibrational modes in different environments

System	Dominant Mode(s)	Frequency Shift	Quality Factor (Q)
Au Nanorods[158]	Breathing (~95.0 GHz) Extensional (~15.0 GHz)	Negligible	Air: 27.6±1.4 Water: 21.8±0.9 Air: 17.9±1.0 Water: 5.6±0.3
Au nanoantenna[203]	Extensional-like (~10.0 GHz)	$\Delta f \approx 0.8$ GHz Decrease from air to mesoporous oxide	Air: 20-30 Mesoporous oxide: 6-8
Au Nanowire[202]	Breathing (~24.0 GHz)	Negligible	Air: 90 ± 29 Water: 39 ± 15
GaP fishnet membrane (This work)	Out-of-plane 5.2 GHz (n = 1) 16.2 GHz (n = 3)	Δf_1 = 0.32 GHz (n = 1) Δf_3 = 1.06 GHz (n = 3)	Air: 51.35 (n = 1) 81.13 (n = 3) SiO_2: 32.80 (n = 1) 25.01 (n = 3)

Furthermore, control experiments were conducted on a simple suspended GaP membrane without any periodic patterning (Figure 3.16). The measured

quality factors (Q_1 = 48.93 ± 4.30 and Q_3 = 98.92 ± 33.97) are comparable to those of the periodic hole array structure, confirming that high-Q localized modes can be achieved even in the absence of periodicity. However, the primary advantage of the periodic hole array lies in its ability to maintain robust acoustic responses while enabling greater flexibility for optical design - such as tuning resonant wavelengths, enhancing light-matter interaction, or supporting guided resonances.

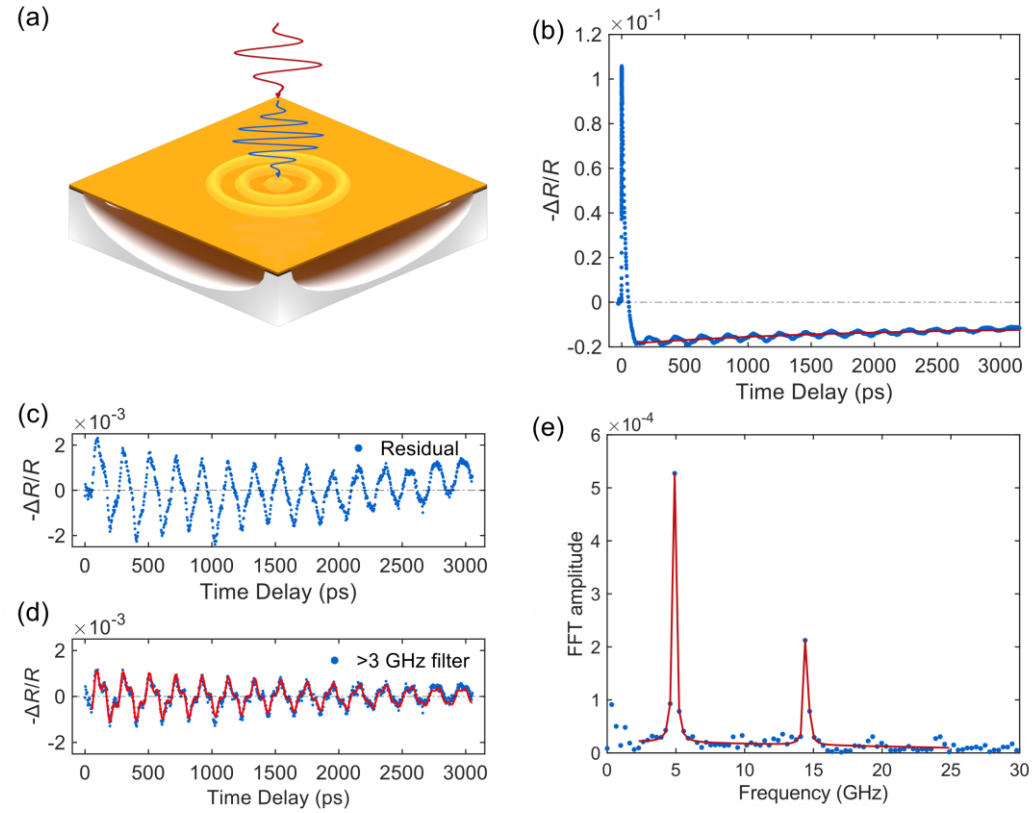

Figure 3.16 Experimental optomechanical response on unpatterned GaP suspended membrane. (a) Schematic of the pump-probe experiment on the suspended membrane. (b) Experimental reflectance change ($\Delta R/R$) of the sample. The red line shows a tri-exponential decay fit to the original data. (c) The residual

signal after subtracting the tri-exponential fit. (d) The optomechanical response spectrum of the sample after applying a 3.0 GHz high-pass filter. The red line is a dual-damped sinusoidal function fit. (e) FFT spectrum of the signal in (d) and red line represent Lorentzian fits for the fundamental and n = 3 resonant modes.

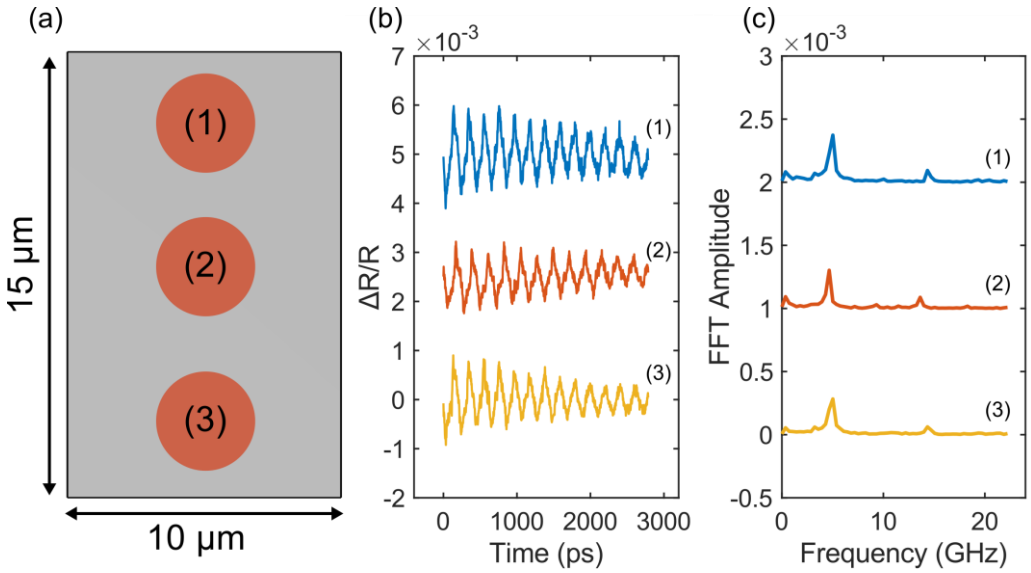

Figure 3.17 Spatial pump-probe scan of an unpatterned suspended GaP film. (a) Schematic diagram marking the scanning regions. (b) Time-domain signals corresponding to each region (misaligned). (c) FFT spectra of each region (shown misaligned).

Table 3.5 Spatial distribution of resonance frequencies and Q factors calculated by equation (R1) across different positions within the same unpatterned GaP suspended membrane.

	(1)	(2)	(3)	Avg ± SD
f_1	4.89	4.58	4.88	4.78 ± 0.18
f_3	14.41	13.58	14.44	14.14 ± 0.49

Q_1	46.68	53.81	46.15	48.93 ± 4.30
Q_3	85.79	137.48	73.42	98.92 ± 33.97

3.4 Conclusion

In summary, we have demonstrated that hypersonic waves can be excited and modulated by the acoustic response of our designed GaP suspended fishnet membranes. Unlike conventional disk structures, the resonant frequencies of these thin-film fishnet membrane are immune to changes in hole diameters, offering new insights into the loss of geometric complementarity in optomechanical systems and highlighting the structural robustness of the design. Furthermore, the fishnet membrane support up to five resonant modes with an exceptionally low isotropic loss factor ($\eta = 0.01$), significantly lower than that of existing conventional plasmonic and dielectric nanosystems. This results in high-quality factors (Q = 65.48 and 90.38 for the fundamental and n = 3 resonant modes), setting a new benchmark for nano-optomechanical platforms. Simulations and experiments consistently confirm that the resonant modes of the fishnet membrane are longitudinally confined to out-of-plane vibration modes. Based on this understanding, we propose and verify that modifying the thin-film thickness could be an effective strategy to modulate these resonant modes. Our work provides direct evidence for the generation of hypersonic waves in suspended thin-film fishnet membrane structures with limited propagation,

laying the foundation for integrating dielectric nanostructures to generate and control acoustic waves at the nanoscale.

Chapter 4 Conclusions and outlook

This thesis systematically carries out an in-depth exploration around the design, fabrication, characterization and application of suspended GaP thin films in photonics and photoacoustics, and achieves representative results in the areas of continuum-spectrum bound-state waveguides, nonlinear optical response, ultrafast all-optical modulation, and GHz photoacoustic vibration modulation. In terms of photonic device design, this thesis proposes and realizes a hybrid waveguide structure based on polymer and a suspended GaP thin film, which utilizes the principle of BIC and achieves a complete decoupling of the TM modes from the continuous spectrum of the TE through geometrical phase control and a multichannel interference mechanism, thus obtaining zero-radiation-loss optical propagation within the continuous spectrum. This approach is different from the traditional waveguide design relying on high refractive index difference and total internal reflection, and avoids the process challenge of deep etching directly on brittle or expensive single-crystal materials, which provides a new technical path for the integration of difficult-to-process materials. Theoretical simulations and experimental tests show that low-loss propagation can be achieved by precisely tuning the geometrical parameters in both linear and curved waveguides, and the design is highly tolerant to fabrication errors, showing good robustness and application potential.

In terms of material fabrication, GaP/AlGaInP/GaAs three-layer structure is epitaxially grown on GaAs substrate using MOCVD, and high-quality suspended

GaP thin films are successfully prepared by wet etching of sacrificial layers. The systematic SEM and AFM characterization shows that the films have excellent thickness uniformity and low surface roughness, which provide a reliable material basis for the subsequent fabrication of photonic devices. In the optical performance test, the propagation losses of BIC waveguides with different widths were measured at 1550 nm and 775 nm wavelengths, respectively, and the results were consistent with the finite element simulations in terms of trend, although the experimental values were higher than the simulation results overall, but they were in good agreement with each other in terms of width dependence, which verified the validity of the model. The higher loss at long wavelengths is mainly attributed to the large mode area and greater sensitivity to sidewall roughness and material absorption, whereas the modes are more concentrated at shorter wavelengths and thus exhibit lower loss levels.

In this work, the Z-scan technique was employed to systematically determine the third-order nonlinear optical coefficients of GaP thin films within the 650–850 nm range, yielding quantitative values for both two-photon absorption coefficients and nonlinear refractive indices. The results show that at 800 nm, GaP exhibits significant antisaturation absorption properties and self-focusing effects, with values close to the best values reported in the literature, indicating that the material maintains excellent nonlinear optical properties. This lays an experimental foundation for its application in the fields of all-optical modulation, nonlinear frequency conversion and ultrafast optical switching.

The important roles of field localization effects and mode modulation in enhancing the nonlinear response are further revealed by comparing the transient

reflection changes of different geometrical structures in ultrafast all-optical modulation experiments. The results show that the grating and waveguide structures, by virtue of the strong local field distribution and mode confinement effects, achieve peak reflectance variations of 2.3% and 2.0% under 775 nm pumping, and 600 nm probing conditions, respectively, which are significantly higher than those of the homogeneous film and bare film structures. In terms of temporal characteristics, all the structures exhibit a fast sub-picosecond rise process and a picosecond decay process, while the slow decay component of the strongly localized structure is significantly weakened, implying a higher signal-to-noise ratio and faster recovery for high-speed modulation applications. Although the current switching energy of 509.7 J/m² is still higher than that of some strongly localized nanostructures, it is expected that the energy consumption can be reduced by more than an order of magnitude by introducing high-Q resonant cavities, photonic crystals, or sub-wavelength periodic structures.

In the direction of photoacoustics, this thesis proposes and validates the superior performance of suspended GaP fishnet membrane structures for GHz vibration modulation. Compared with the conventional nanodisk structure, the fishnet membrane presents completely different vibration mode distributions and energy dissipation characteristics in photoacoustic interactions. It is shown that the structure is not only capable of supporting multiple higher-order odd vibrational modes, but also significantly extends the vibrational lifetime and improves the quality factor to more than 90, which is an order of magnitude higher than that of the conventional design. This result reveals the difference in

the behavior of geometrically complementary designs in the photoacoustic and electromagnetic domains, and shows that by optimizing the boundary conditions of the suspended medium structure, energy leakage can be effectively suppressed and long-lived, high-Q optomechanical vibrations can be achieved.

Future research can be further deepened in the following directions: first, in all-optical modulation applications, stronger field localization and mode compression can be achieved by introducing high-quality factor resonant cavities, photonic crystals, or sub-wavelength structures, which is expected to significantly reduce the switching energy consumption and enhance the depth of modulation. Second, the suspended GaP waveguide can be integrated with functional modules such as nonlinear frequency conversion, quantum light source, and opto-mechanical resonator, and a multi-physics field coupling system-on-chip to meet the needs of high-speed optical communication and quantum information processing. To expand the device's performance in a wider wavelength band, and to explore its potential applications in visible, mid-infrared and multi-wavelength communication and imaging. In addition, to optimize the photoacoustic modeling of high-Q structures by combining cavity optomechanics, which is expected to achieve high-sensitivity sensing and ultra-low-noise signal processing. Lastly, to extend the design concepts in this paper to other high-performance materials, such as silicon nitride, gallium nitride, diamond, or lithium niobate, and a multifunctional, low-energy, and high-speed photonic-photo-acoustic hybrid integrated system can be obtained through heterogeneous integration.

It can be expected that with the continuous optimization of structural design

methods, further improvement of fabrication processes, and gradual implementation of multifunctional integration strategies, the suspended GaP thin-film devices will show broader application prospects in the frontier areas of low-loss photon transmission, ultra-fast all-optical modulation, and high-Q opto-mechanical vibration

Appendix

Appendix A The code used for Z-scan measurement

```
clear all;
clc;
% parameter description: wavelength, laser pulse width, spot x-diameter, spot y-diameter, laser absorption ratio, sample surface power, front aperture power, rear aperture power
% for i=50:5:150
[num,txt,raw]=xlsread('pa.xlsx');
%for i=1:size(num(:,1))
N=8; % number of different wavelengths
B=zeros(1,N); % two-photon absorption coefficient
n2=zeros(1,N); %n2
RMSE=zeros(1,N);
RMSE1=zeros(1,N);
p=zeros(1,N*2);
p1=zeros(1,N*2);
Ra=zeros(1,N);
Ra1=zeros(1,N);
d1=zeros(1,N);
Lc=zeros(1,N);
%wavelength=1100;
R=num(:,7);% reflectivity
L=0.5*10^-3;
for i=8:N
for m=1:1
clearvars -EXCEPT i B THREE RMSE RMSE1 num txt raw N m n p Ra Ra1 n2 wavelength L p1 d1 Lc R
clc;
range=100;
para=num(i,:);
h=num2str(m);% repetition count
%h1=num2str(2*m);
txt_temp=[txt{i,1},' open ',txt{i,2},'-',h,'.txt'];
```

```
file1=txt_temp;
file2=strrep(file1,'open','close');
T1= load(file1);
%file1=strrep(file1,h,h1);
global T2
%T2=load(file1);
%T1=(T1+T2)/2;
lamda=para(1)*10^-9;
k=2*pi/lamda; % laser wave vector
Pf=para(5)*(1-R(i)); % power on sample surface, unit mw
Pb=mean(T1(1:5,3))*10^3/(1-R(i)); % power behind sample, unit mw
bw=para(2)*10^-15; % pulse width, unit fs
dx=para(3)*10^-6; % spot size μm
dy=para(4)*10^-6; % spot size μm
S=pi*dx*dy/4;

a=-log(Pb/Pf)/L; % linear absorption coefficient of sample
I0=Pf4(log(2))^0.5/pi^0.5 * 10^-3/10000/bw/S; % peak intensity
fprintf('peak intensity is%d GW/cm2\n',I0 * 10^-13);
w0=(dx+dy)/4; % focus waist radius, after focusing waist diameter d=0.61wave-
lengthfocal length/spot size before focusing Gaussian beam transformation
through thin lens
%% nonlinear absorption


if a<=0
    a=0;
    Leff=L;    % effective thickness for two-photon absorption
    Leff1=L;    % effective thickness for three-photon absorption
else
     Leff=(1-exp(-a*L))/a;    % effective thickness for two-photon absorption
     Leff1=(1-exp(-2*a*L))/2/a;    % effective thickness for three-photon ab-
sorption
end

global z0
z0=k*w0^2/2;
Lc(i)=z0;
global c1
c1=I0*Leff*10^(-13);
```

```
global  c2
c2=2*I0^2*Leff1*10^(-28);


% T1(1:100,:)=[];
% T1(size(T1,1)-50:size(T1,1),:)=[];
T1(:,3)=T1(:,3)/(mean(T1(1:10,3))+mean(T1(size(T1,1)-10:size(T1,1),3)))*2;
[x,y]=min(T1(:,3));
z=T1(:,1)-T1(y,1);
j=0;
d=zeros(1,2);
l=1;

for ii=1:size(T1,1)    % take data within 80 mm range
    if abs(z(ii))<=range
      j=j+1;
      z1(j)=z(ii);
      T11(j)=T1(ii,3);
    end

    if ii<size(T1,1)&&T1(ii,3)>=(x+1)/2  && T1(ii+1,3)<=(x+1)/2
          d(l)=z(ii);
          l=l+1;
    end
end
d1(i)=abs(d(2)-d(1))*10^-3+d1(i);
z1=z1*10^-3;
%plot(z1*10^3,T11,'ko','markersize',4);hold  on;
figure,plot(z1*10^3,T11,'ko','markersize',4);hold  on;
syms t b X;


% f=fittype('1-b*c1/(1+(t/z0).^2)/2.^1.5+(-b*c1/(1+(t/z0).^2)).^2/3.^1.5+(-
b*c1/(1+(t/z0).^2)).^3/4.^1.5+(-b*c1/(1+(t/z0).^2)).^4/5.^1.5+(-
b*c1/(1+(t/z0).^2)).^5/6.^1.5+(-b*c1/(1+(t/z0).^2)).^6/7.^1.5','inde-
pendent','t','coefficients',{'b'},'problem',{'c1','z0'});
%    f=fittype('1-b*c1/(1+(t/z0).^2)/2.^1.5','independent','t','coeffi-
cients',{'b'},'problem',{'c1','z0'});
% g1=@(b,x)1/(pi.*b.*c2).^0.5*quad(@(t) log((1+c2.*b/(1+x^2/z0^2)^2.*exp(-
2*t^2)).^0.5+(c2*b).^0.5/(1+x^2/z0.^2)*exp(-t.^2)),t,-1000,1000)
```

```
% f1=fittype(g1)
% 1/factorial(2*1-1)
% clc;
z11=z1';
T2=T11';
one=ones(size(T2,1),1);


      %TWO
      %options = optimoptions('lsqcurvefit','Algorithm','levenberg-marquardt');
      [r,resnorm,residual,exitflag,output]=lsqcurvefit(@f2,700,z11,one,0,5000);
      %f=fittype('1-b.*c1./(1+(t./z0).^2)./2.^1.5+(-
1).^2.*(b.*c1./(1+(t./z0).^2)).^2./3.^1.5+(-
1).^3.*(b.*c1./(1+(t./z0).^2)).^3./4.^1.5+(-
1).^4.*(b.*c1./(1+(t./z0).^2)).^4./5.^1.5+(-
1).^5.*(b.*c1./(1+(t./z0).^2)).^5./6.^1.5+(-
1).^6.*(b.*c1./(1+(t./z0).^2)).^6./7.^1.5+(-
1).^7.*(b.*c1./(1+(t./z0).^2)).^7./8.^1.5+(-
1).^8.*(b.*c1./(1+(t./z0).^2)).^8./9.^1.5+(-
1).^8.*(b.*c1./(1+(t./z0).^2)).^8./9.^1.5','independent','t','coeffi-
cients',{'b'},'problem',{'c1','z0'});
      %[cfun,goodness,o]=fit(z11,T2,f,'problem',{c1,z0},'StartPoint', 1)
      dlmwrite('2.txt',r*10^-13,'-append')%b *10^-13
      B(i)=r+B(i);
      p(2*i+m-2)=r;
      rmse=(resnorm/size(z11,1))^0.5;
      dlmwrite('RMSE.txt',rmse,'-append');
      RMSE(i)=rmse+RMSE(i);

%f=fittype('(-1)^(1-1)*((2*c2*b)^0.5/(1+(t/z0)^2))^(2*1-2)/factorial(2*1-
1)/(2*1-1)^0.5+(-1)^(2-1)*((2*c2*b)^0.5/(1+(t/z0)^2))^(2*2-2)/factorial(2*2-
1)/(2*2-1)^0.5+(-1)^(3-1)*((2*c2*b)^0.5/(1+(t/z0)^2))^(2*3-2)/factorial(2*3-
1)/(2*3-1)^0.5+(-1)^(4-1)*((2*c2*b)^0.5/(1+(t/z0)^2))^(2*4-2)/factorial(2*4-
1)/(2*4-1)^0.5+(-1)^(5-1)*((2*c2*b)^0.5/(1+(t/z0)^2))^(2*5-2)/factorial(2*5-
1)/(2*5-1)^0.5','independent','t','coefficients',{'b'},'problem',{'c2','z0'});
% f1=fittype(@(b,x)t(b,x));
%cfun=fit(z1,T2,f1,'problem')
%cfun=fit(z11,T2,f,'problem',{c2,c1,z0})% fit data x,y using custom fitting
function f,'lower',[0 0]
```

```
%dlmwrite('1.txt',file1(1:end-15),'-append','delimiter','')
dlmwrite('1.txt',I0*10^-13,'-append','delimiter','');


T3=f2(r,z11).*T2;
plot(z11*10^3,T3,'r','LineWidth',2);hold on
set(gca,'FontName','Times New Roman','FontSize',10,'FontWeight','bold');
%set(gcf,'unit','centimeters','position',[10 5 12 4.5]);
ylabel('Normalized {\itT}','FontName','Times New Roman','FontSize',12);
xlabel('{\itz} (mm)','FontName','Times New Roman','FontSize',12);
%text(,file1(1:end-13));
axis([-range range  min(T3)-(1-min(T3))/7 1+(1-min(T3))/10]);
   tx=[num2str(para(1)),'nm','-',num2str(m)];

text(range-35,min(T3)+(1-min(T3))/4,tx,'FontName','Times New Roman','Font-
Size',15);
filename=[file1,'.fig'];
savefig(filename);
% end


%  Nonlinear refractive index

temp=T1;
T1=load(file2);
%file2=strrep(file2,'2*m-1','2*m');
%T2=load(file2);
%T1=(T1+T2)./2;
% T1(:,3)=T1(:,3)./(mean(T1(1:10,3))+mean(T1(end-10:end,3))).*2;
% S=1-exp(-2*(-log(mean(T1(1:10,3))*10^3/para(m+6)*(exp(-1)-1)+1))^0.5);

% consider both absorption and refraction
temp(:,3)=temp(:,3)/(mean(temp(1:10,3))+mean(temp(size(temp,1)-
10:size(temp,1),3)))*2;
T1(:,3)=T1(:,3)./temp(:,3);
T1(:,3)=T1(:,3)/(mean(T1(1:5,3))+mean(T1(size(T1,1)-5:size(T1,1),3)))*2;


%figure,plot(temp(:,1),temp(:,3),'ro','markersize',4);hold on;
% plot(T1(:,1),T1(:,3),'ko','markersize',4);hold on;
```

```
% T1(:,3)=T1(:,3)./temp(:,3)
% plot(T1(:,1),T1(:,3),'bo','markersize',4);hold on;
j=0;
for ii=1:size(T1,1)
    if abs(z(ii))<=range
     j=j+1;
     z1(j)=z(ii);
     T11(j)=T1(ii,3);
    end
end
%[x,y]=min(T1(:,3));
z1=z1*10^-3;
figure,plot(z1*10^3,T11,'ko','markersize',4);hold on;
x=z1/z0;
global fai fai1
fai=k*Leff*I0*10^(-19); % to ensure n2 is relatively larger, multiply back corresponding result
fai1=k*Leff1*I0^2*10^(-34);
z11=z1';
global T2
T2=T11';
syms t

        options = optimoptions('lsqcurvefit','Algorithm','levenberg-marquardt');
        [rr,resnorm,residual,exitflag,output]=lsqcurvefit(@r3,6,z11,one,[],[],options);

p1(2*i+m-2)=rr;
n2(i)=n2(i)+rr;
RMSE1(i)=(resnorm/size(z11,1))^0.5+RMSE1(i);
% fit data x,y using custom fitting function f
T3=r3(rr,z11).*T2;
dlmwrite('4.txt',file2(1:end-15),'-append','delimiter','');
dlmwrite('5.txt',rr*10^-19,'-append');
dlmwrite('RMSE1.txt',(resnorm/size(z11,1))^0.5,'-append');

% p1(2*i+m-2)=cfun.n2;
% n2(i)=n2(i)+cfun.n2;
% RMSE1(i)=goodness.rmse+RMSE1(i);
% T3=cfun(z11);
```

```
% dlmwrite('4.txt',file2(1:end-15),'-append','delimiter','')
% dlmwrite('5.txt',cfun.n2,'-append')
% dlmwrite('RMSE1.txt',goodness.rmse,'-append')

plot(z11*10^3,T3,'r','LineWidth',2);
text(range-35,min(T3)+(1-min(T3))/4,tx,'FontName','Times New Roman','Font-
Size',15)
% text(range-35,0.45+(1-0.45)/4,'700nm','FontName','Times New Roman','Font-
Size',15)
set(gca,'FontName','Times New Roman','FontSize',10,'FontWeight','bold');
%set(gcf,'unit','centimeters','position',[10 5 12 4.5]);
ylabel('Normalized {\itT}','FontName','Times New Roman','FontSize',12)
xlabel('{\itz} (mm)','FontName','Times New Roman','FontSize',12)
%title(file2(1:end-13));
filename=[file2,'.fig'];
savefig(filename);
end
Ra(i)=std([p(2*i-1),p(2*i)]);
Ra1(i)=std([p1(2*i-1),p1(2*i)]);
end

% B=B*10^-19/2;%
B=B*10^-13/2;%
RMSE=RMSE/2;
RMSE1=RMSE1/2;
n2=n2*10^-19/2;
Ra=Ra*10^-13;
Ra1=Ra1*10^-19;
d1=d1/2;
% B=B*10^-6;
% Ra=Ra*10^-6;
% n2=n2*10^-15;
% Ra1=Ra1*10^-15;

dlmwrite('errorbar1.txt',Ra');
dlmwrite('errorbar2.txt',Ra1');

figure,errorbar(num(:,1),B,Ra,'ro');hold on
plot(num(:,1),B,'r-','LineWidth',2);hold on
set(gca,'FontName','Times New Roman','FontSize',10,'FontWeight','bold');
```

```
set(gcf,'unit','centimeters','position',[10 5 12 4.5]);
ylabel('2PA coefficient (m/W)','FontName','Times New Roman','FontSize',12);
xlabel('Wavelength (nm)','FontName','Times New Roman','FontSize',12);
savefig('2PA coefficient');

figure,errorbar(num(:,1),n2,Ra1,'ro');hold on
plot(num(:,1),n2,'r-','LineWidth',2);hold on
set(gca,'FontName','Times New Roman','FontSize',10,'FontWeight','bold');
set(gcf,'unit','centimeters','position',[10 5 12 4.5]);
ylabel('Nonlinear refractive coefficient (m^2/W)','FontName','Times New
Roman','FontSize',12);
xlabel('Wavelength (nm)','FontName','Times New Roman','FontSize',12);
savefig('Nonlinear refractive coefficient');

figure,plot(num(:,1),RMSE,'ro');hold on
plot(num(:,1),RMSE,'r-','LineWidth',2);hold on
set(gca,'FontName','Times New Roman','FontSize',10,'FontWeight','bold');
set(gcf,'unit','centimeters','position',[10 5 12 4.5]);
ylabel('Absorption model RMSE','FontName','Times New Roman','Font-
Size',12);
xlabel('Wavelength (nm)','FontName','Times New Roman','FontSize',12);
savefig('Absorption model RMSE');

figure,plot(num(:,1),RMSE1,'ro');hold on
plot(num(:,1),RMSE1,'r-','LineWidth',2);hold on
set(gca,'FontName','Times New Roman','FontSize',10,'FontWeight','bold');
set(gcf,'unit','centimeters','position',[10 5 12 4.5]);
ylabel('Refractive model RMSE','FontName','Times New Roman','FontSize',12);
xlabel('Wavelength (nm)','FontName','Times New Roman','FontSize',12);
savefig('Refractive model RMSE');

FOM=n2*diag((B*diag(num(:,1)*10^-9)).^-1);
figure,plot(num(:,1),FOM,'LineWidth',2); %FOM(figure-of-merit)
set(gca,'FontName','Times New Roman','FontSize',10,'FontWeight','bold');
set(gcf,'unit','centimeters','position',[10 5 12 4.5]);
savefig('FOM');

plot(Lc,d1);
figure,meshgrid(Lc,d1,num(:,1));
scatter(Lc,d1,[],num(:,1),'filled');hold on
```

```
colorbar;
plot(Lc,Lc*1.7);


function Y=f2(b,z11)
global c1 z0 T2
Y=zeros(size(z11,1),1);
syms x;
for i=1:size(z11,1)
Y(i) = vpaintegral(log(1+b.*c1./(1+(z11(i)./z0).^2).*exp(-x^2)),x,[-
inf,inf])./(pi^0.5*b.*c1./(1+(z11(i)./z0).^2));
end
Y=Y./T2;
end
function y=r3(n22,z11)
%n22=-16;
global z0 fai T2
d=1;
N=10;
theta=zeros(size(z11,1),N);
dm=zeros(size(z11,1),N);
d0=z0.*(1+z11.^2./z0.^2);
g=1+d./(z11.*(1+z0.^2./z11.^2));
g(isnan(g)==1)=0;
g(find(g==0))=(g(find(g==0)-1)+g(find(g==0)+1))/2;
theta0=atan(d./d0./g);
y=(g.^2+d.^2./d0.^2).^-0.5.*exp(1i.*theta0);
y0=y;
for m=1:N
dm(:,m)=d0./(2*m+1);
theta(:,m)=atan(d./g./dm(:,m));
y=y+(-1i.*n22.*fai./(1+z11.^2./z0.^2)).^m./facto-
rial(m).*(g.^2+d.^2./dm(:,m).^2).^-0.5.*exp(1i.*theta(:,m));
end
y=abs(y).^2./abs(y0).^2;
y=y./T2;
end
```

Appendix B The recipes for device fabrication

No.	Step Name	Equipment	Detailed Operation	Remarks
1	Cleaning	Wet Bench	Ultrasonic cleaning in Acetone and IPA for 5 min each	\
2	Thinning (Etching)	ICP (Inductively Coupled Plasma)	Chlorine-based recipe	Use dummy wafer for step height
3	Microscopy Inspection	Microscope	\	\
4	Thickness Measurement	Profilometer	Measure the step height of the dummy wafer	\
5	Photolithography	Spin Coater	Photoresist: RZJ304.10	Plasma treatment before coating
6	Microscopy Inspection	Microscope	Inspect developed patterns and surface impurities	\
7	Etching	ICP	Chlorine-based recipe	Use dummy wafer for step height
8	PR Stripping	Water Bath	Photoresist stripper solution	Plasma treatment before stripping
9	Microscopy Inspection	Microscope	Check for residual PR and impurities	\
10	Thickness Measurement	Profilometer	Measure the step height of the dummy wafer	\
11	Wet Etching 1	Wet Bench	Buffered Oxide Etching solution	\
12	Microscopy Inspection	Microscope	\	\
13	Wet Etching 2	Wet Bench	Weak acid solution	\
14	Microscopy Inspection	Microscope	\	\
15	PR Patterning	ICP	Photoresist: RZJ304.10	Plasma treatment before coating

References

[1] W.-Q. Wei *et al.*, “Monolithic integration of embedded III-V lasers on SOI,” *Light Sci. Appl.*, vol. 12, no. 1, p. 84, Apr. 2023, doi: 10.1038/s41377-023-01128-z.

[2] C. Xiang *et al.*, “3D integration enables ultralow-noise isolator-free lasers in silicon photonics,” *Nature*, vol. 620, no. 7972, pp. 78–85, 2023, doi: 10.1038/s41586-023-06251-w.

[3] M. A. Tran *et al.*, “Extending the spectrum of fully integrated photonics to submicrometre wavelengths,” *Nature*, vol. 610, no. 7930, pp. 54–60, 2022, doi: 10.1038/s41586-022-05119-9.

[4] P. Wen *et al.*, “Waveguide coupled III-V photodiodes monolithically integrated on Si,” *Nat. Commun.*, vol. 13, no. 1, p. 909, Feb. 2022, doi: 10.1038/s41467-022-28502-6.

[5] S. Cuyvers *et al.*, “Low Noise Heterogeneous III-V-on-Silicon-Nitride Mode-Locked Comb Laser,” *Laser Photon. Rev.*, vol. 15, no. 8, p. 2000485, Aug. 2021, doi: 10.1002/lpor.202000485.

[6] C. Xiang *et al.*, “Narrow-linewidth III-V/Si/Si 3 N 4 laser using multilayer heterogeneous integration,” *Optica*, vol. 7, no. 1, p. 20, Jan. 2020, doi: 10.1364/OPTICA.384026.

[7] Y. Hu *et al.*, “III/V-on-Si MQW lasers by using a novel photonic integration method of regrowth on a bonding template,” *Light Sci. Appl.*, vol. 8, no. 1, p. 93, Oct. 2019, doi: 10.1038/s41377-019-0202-6.

[8] J. Zhang *et al.*, "III-V-on-Si photonic integrated circuits realized using micro-transfer-printing," *APL Photonics*, vol. 4, no. 11, p. 110803, Nov. 2019, doi: 10.1063/1.5120004.

[9] G. N. Malheiros-Silveira, F. Lu, I. Bhattacharya, T. T. D. Tran, H. Sun, and C. J. Chang-Hasnain, "III-V Compound Semiconductor Nanopillars Monolithically Integrated to Silicon Photonics," *ACS Photonics*, vol. 4, no. 5, pp. 1021–1025, 2017, doi: 10.1021/acsphotonics.6b01035.

[10] P. Trofimov *et al.*, "Perovskite-Gallium Phosphide Platform for Reconfigurable Visible-Light Nanophotonic Chip," *ACS Nano*, vol. 14, no. 7, pp. 8126–8134, 2020, doi: 10.1021/acsnano.0c01104.

[11] V. V. Fedorov *et al.*, "Gallium Phosphide Nanowires in a Free-Standing, Flexible, and Semitransparent Membrane for Large-Scale Infrared-to-Visible Light Conversion," *ACS Nano*, vol. 14, no. 8, pp. 10624–10632, 2020, doi: 10.1021/acsnano.0c04872.

[12] M. Melli *et al.*, "Gallium phosphide optical metasurfaces for visible light applications," *Sci. Rep.*, vol. 10, no. 1, p. 20694, 2020, doi: 10.1038/s41598-020-77753-0.

[13] B. Tilmann *et al.*, "Nanostructured amorphous gallium phosphide on silica for nonlinear and ultrafast nanophotonics," *Nanoscale Horizons*, vol. 5, no. 11, pp. 1500–1508, 2020, doi: 10.1039/d0nh00461h.

[14] N. Hekmat *et al.*, "Cryogenically cooled gallium phosphide for optical rectification at high driving average powers," *Opt. Mater. Express*, vol. 10, no. 11, pp. 2768–2782, 2020, doi: 10.1364/OME.402564.

[15] G. Grinblat *et al.*, "Efficient ultrafast all-optical modulation in a nonlinear crystalline gallium phosphide nanodisk at the anapole excitation," *Sci. Adv.*, vol. 6, no. 34, p. eabb3123, 2020, doi: 10.1126/sciadv.abb3123.

[16] G. Grinblat, M. P. Nielsen, P. Dichtl, Y. Li, R. F. Oulton, and S. A. Maier, "Ultrafast sub–30-fs all-optical switching based on gallium phosphide," *Sci. Adv.*, vol. 5, no. 6, p. eaaw3262, 2019, doi: 10.1126/sciadv.aaw3262.

[17] V. Remesh, G. Grinblat, Y. Li, S. A. Maier, and N. F. Van Hulst, "Coherent Multiphoton Control of Gallium Phosphide Nanodisk Resonances," *ACS Photonics*, vol. 6, no. 10, pp. 2487–2491, 2019, doi: 10.1021/acsphotonics.9b00780.

[18] K. Schneider *et al.*, "Optomechanics with one-dimensional gallium phosphide photonic crystal cavities," *Optica*, vol. 6, no. 5, p. 577, 2019, doi: 10.1364/optica.6.000577.

[19] W. Xie *et al.*, "Nonlinear response of a gallium phosphide nanopatterned photonic waveguide in the CW regime," *Opt. Lett.*, vol. 44, no. 11, p. 2823, May 2019, doi: 10.1364/ol.44.002823.

[20] W. M. Haynes, *CRC handbook of chemistry and physics*. Boca Raton, Florida: CRC press, 2016.

[21] C. Wang, J. Cai, X. Liu, C. Chen, X. Chen, and K. J. Karki, "In Operando Quantification of Single and Multiphoton Photocurrents in GaP and InGaN Photodetectors with Phase-Modulated Femtosecond Light Pulses," *ACS Photonics*, vol. 10, no. 4, pp. 1119–1125, 2022, doi:

10.1021/acsphotonics.2c01851.

[22] Y. Choi, C. Choi, J. Bae, J. Park, and K. Shin, "Journal of Industrial and Engineering Chemistry Synthesis of gallium phosphide quantum dots with high photoluminescence quantum yield and their application as color converters for LEDs," *J. Ind. Eng. Chem.*, vol. 123, pp. 509–516, 2023, doi: 10.1016/j.jiec.2023.04.005.

[23] N. Thomas, R. J. Barbour, Y. Song, M. L. Lee, and K. C. Fu, "Waveguide-integrated single-crystalline GaP resonators on diamond," *Opt. Express*, vol. 22, no. 11, p. 13555, Jun. 2014, doi: 10.1364/OE.22.013555.

[24] S. Chakravarthi *et al.*, "Inverse-designed photon extractors for optically addressable defect qubits," *Optica*, vol. 7, no. 12, p. 1805, Dec. 2020, doi: 10.1364/OPTICA.408611.

[25] C. Munley *et al.*, "Visible Wavelength Flatband in a Gallium Phosphide Metasurface," *ACS Photonics*, vol. 10, no. 8, pp. 2456–2460, Aug. 2023, doi: 10.1021/acsphotonics.3c00175.

[26] J. Wolters *et al.*, "Enhancement of the zero phonon line emission from a single nitrogen vacancy center in a nanodiamond via coupling to a photonic crystal cavity," *Appl. Phys. Lett.*, vol. 97, no. 14, p. 141108, Oct. 2010, doi: 10.1063/1.3499300.

[27] S. Chakravarthi *et al.*, "Hybrid Integration of GaP Photonic Crystal Cavities with Silicon-Vacancy Centers in Diamond by Stamp-Transfer," *Nano Lett.*, vol. 23, no. 9, pp. 3708–3715, May 2023, doi: 10.1021/acs.nanolett.2c04890.

[28] O. Mey *et al.*, “Enhancement of the Monolayer Tungsten Disulfide Exciton Photoluminescence with a Two-Dimensional Material/Air/Gallium Phosphide In-Plane Microcavity,” *ACS Nano*, vol. 13, no. 5, pp. 5259–5267, May 2019, doi: 10.1021/acsnano.8b09659.

[29] L. Sortino *et al.*, “Bright single photon emitters with enhanced quantum efficiency in a two-dimensional semiconductor coupled with dielectric nano-antennas,” *Nat. Commun.*, vol. 12, no. 1, p. 6063, Oct. 2021, doi: 10.1038/s41467-021-26262-3.

[30] B. Tilmann *et al.*, “Comparison of Harmonic Generation from Crystalline and Amorphous Gallium Phosphide Nanofilms,” *Adv. Opt. Mater.*, vol. 11, no. 16, p. 2300269, 2023, doi: 10.1002/adom.202300269.

[31] J.-S. Park, M. Tang, S. Chen, and H. Liu, “Heteroepitaxial Growth of III-V Semiconductors on Silicon,” *Crystals*, vol. 10, no. 12, p. 1163, Dec. 2020, doi: 10.3390/cryst10121163.

[32] Y. Du *et al.*, “Review of Highly Mismatched III-V Heteroepitaxy Growth on (001) Silicon,” *Nanomaterials*, vol. 12, no. 5, p. 741, 2022, doi: 10.3390/nano12050741.

[33] H. Emmer *et al.*, “Fabrication of Single Crystal Gallium Phosphide Thin Films on Glass,” *Sci. Rep.*, vol. 7, no. 1, pp. 2–7, 2017, doi: 10.1038/s41598-017-05012-w.

[34] V. V. Fedorov *et al.*, “Nanoscale Gallium Phosphide Epilayers on Sapphire for Low-Loss Visible Nanophotonics,” *ACS Appl. Nano Mater.*, vol. 5, no. 7, pp. 8846–8858, 2022, doi: 10.1021/acsanm.2c00941.

[35] J. Cambiasso, G. Grinblat, Y. Li, A. Rakovich, E. Cortés, and

S. A. Maier, “Bridging the Gap between Dielectric Nanophotonics and the Visible Regime with Effectively Lossless Gallium Phosphide Antennas,” *Nano Lett.*, vol. 17, no. 2, pp. 1219–1225, 2017, doi: 10.1021/acs.nanolett.6b05026.

[36] K. Rivoire, Z. Lin, F. Hatami, and J. Vučković, “Sum-frequency generation in doubly resonant GaP photonic crystal nanocavities,” *Appl. Phys. Lett.*, vol. 97, no. 4, p. 043103, 2010, doi: 10.1063/1.3469936.

[37] N. S. Yama *et al.*, “Silicon-Lattice-Matched Boron-Doped Gallium Phosphide: A Scalable Acousto-Optic Platform,” *Adv. Mater.*, vol. 36, no. 5, p. 2305434, Feb. 2024, doi: 10.1002/adma.202305434.

[38] R. J. Shul, A. G. Baca, D. J. Rieger, H. Hou, S. J. Pearton, and F. Ren, “Ecr Etching of GaP, GaAs, InP, and InGaAs in Cl 2 /Ar, Cl 2 /N 2 , BCl 3 /Ar, and BCl 3 /N 2,” *MRS Proc.*, vol. 421, p. 245, Feb. 1996, doi: 10.1557/PROC-421-245.

[39] M. Levinshtein, *Handbook series on semiconductor parameters*, vol. 1. World Scientific, 1997.

[40] D. J. Wilson *et al.*, “Integrated gallium phosphide nonlinear photonics,” *Nat. Photonics*, vol. 14, no. 1, pp. 57–62, Jan. 2020, doi: 10.1038/s41566-019-0537-9.

[41] M. Billet *et al.*, “Gallium phosphide-on-insulator integrated photonic structures fabricated using micro-transfer printing,” *Opt. Mater. Express*, vol. 12, no. 9, p. 3731, 2022, doi: 10.1364/ome.461146.

[42] K. Suto and J. Nishizawa, “Radiative recombination mechanisms in stoichiometry-controlled GaP crystals,” *J. Appl. Phys.*, vol.

67, no. 1, pp. 459–464, 1990, doi: 10.1063/1.345225.

[43] D. F. Nelson and E. H. Turner, “Electro-optic and piezoelectric coefficients and refractive index of Gallium Phosphide,” *J. Appl. Phys.*, vol. 39, no. 7, pp. 3337–3343, 1968, doi: 10.1063/1.1656779.

[44] D. P. Lake, M. Mitchell, H. Jayakumar, L. F. dos Santos, D. Curic, and P. E. Barclay, “Efficient telecom to visible wavelength conversion in doubly resonant gallium phosphide microdisks,” *Appl. Phys. Lett.*, vol. 108, no. 3, p. 031109, Jan. 2016, doi: 10.1063/1.4940242.

[45] A. Standing *et al.*, “Efficient water reduction with gallium phosphide nanowires,” *Nat. Commun.*, vol. 6, no. 1, p. 7824, 2015, doi: 10.1038/ncomms8824.

[46] W. Cheng *et al.*, “Wafer-scale inverted gallium phosphide-on-insulator rib waveguides for nonlinear photonics,” *Opt. Lett.*, vol. 48, no. 14, p. 3781, 2023, doi: 10.1364/ol.494949.

[47] J. Ye and M. Huang, “Non-saturation intensity dependence of anisotropic third-order optical nonlinearity approaching the damage threshold in ZnSe and GaP,” *Results Phys.*, vol. 58, no. March 2024, p. 107474, Mar. 2024, doi: 10.1016/j.rinp.2024.107474.

[48] C. J. Glassbrenner and G. A. Slack, “Thermal Conductivity of Si and Ge. from 3 K to the Melting Point,” *Phys. Rev.*, vol. 134, no. 4A, pp. 1058–1069, 1964, doi: 10.1103/PhysRev.134.A1058.

[49] M. Dinu, F. Quochi, and H. Garcia, “Third-order nonlinearities in silicon at telecom wavelengths,” *Appl. Phys. Lett.*, vol. 82, no. 18, pp. 2954–2956, May 2003, doi: 10.1063/1.1571665.

[50] M. Pu, L. Ottaviano, E. Semenova, and K. Yvind, "Efficient frequency comb generation in AlGaAs-on-insulator," *Optica*, vol. 3, no. 8, p. 823, Aug. 2016, doi: 10.1364/OPTICA.3.000823.

[51] B. J. M. Hausmann, I. Bulu, V. Venkataraman, P. Deotare, and M. Lončar, "Diamond nonlinear photonics," *Nat. Photonics*, vol. 8, no. 5, pp. 369–374, May 2014, doi: 10.1038/nphoton.2014.72.

[52] C. Xiong *et al.*, "Integrated GaN photonic circuits on silicon (100) for second harmonic generation," *Opt. Express*, vol. 19, no. 11, p. 10462, May 2011, doi: 10.1364/OE.19.010462.

[53] D. Munk *et al.*, "Four-Wave Mixing in GaN Waveguides," in *Conference on Lasers and Electro-Optics*, 2018, p. SF2A.4, doi: 10.1364/CLEO_SI.2018.SF2A.4.

[54] X. Ji *et al.*, "Ultra-low-loss on-chip resonators with sub-milliwatt parametric oscillation threshold," *Optica*, vol. 4, no. 6, p. 619, Jun. 2017, doi: 10.1364/OPTICA.4.000619.

[55] J. Li, H. Lee, T. Chen, and K. J. Vahala, "Low-Pump-Power, Low-Phase-Noise, and Microwave to Millimeter-Wave Repetition Rate Operation in Microcombs," *Phys. Rev. Lett.*, vol. 109, no. 23, p. 233901, Dec. 2012, doi: 10.1103/PhysRevLett.109.233901.

[56] R. W. Boyd, "Nonlinear Optics: Third Edition," 2008, [Online]. Available: https://api.semanticscholar.org/CorpusID:122684280.

[57] H. Jung, C. Xiong, K. Y. Fong, X. Zhang, and H. X. Tang, "Optical frequency comb generation from aluminum nitride microring resonator," *Opt. Lett.*, vol. 38, no. 15, p. 2810, Aug. 2013, doi:

10.1364/OL.38.002810.

[58] C. Xiong, W. H. P. Pernice, X. Sun, C. Schuck, K. Y. Fong, and H. X. Tang, “Aluminum nitride as a new material for chip-scale optomechanics and nonlinear optics,” *New J. Phys.*, vol. 14, p. 095014, 2012, doi: 10.1088/1367-2630/14/9/095014.

[59] F. Li *et al.*, “Optical rectification in 4H-SiC: Paving the way to generate strong terahertz fields with ultra-wide bandwidth,” *High Power Laser Sci. Eng.*, vol. 11, no. 5, p. 05000e62, 2023, doi: 10.1017/hpl.2023.52.

[60] Y. Zheng, M. Pu, A. Yi, X. Ou, and H. Ou, “4H-SiC microring resonators for nonlinear integrated photonics,” *Opt. Lett.*, vol. 44, no. 23, p. 5784, 2019, doi: 10.1364/ol.44.005784.

[61] D. Zhu *et al.*, “Integrated photonics on thin-film lithium niobate,” *Adv. Opt. Photonics*, vol. 13, no. 2, p. 242, Jun. 2021, doi: 10.1364/AOP.411024.

[62] C. Wang *et al.*, “Lithium tantalate electro-optical photonic integrated circuits for high volume manufacturing,” *Nature*, vol. 629, no. 8013, pp. 784–790, 2024, doi: 10.1038/s41586-024-07369-1.

[63] S. Ashihara *et al.*, “Nonlinear refraction of femtosecond pulses due to quadratic and cubic nonlinearities in periodically poled lithium tantalate,” *Opt. Commun.*, vol. 222, no. 1–6, pp. 421–427, 2003, doi: 10.1016/S0030-4018(03)01568-2.

[64] I. Shoji, T. Kondo, A. Kitamoto, M. Shirane, and R. Ito, “Absolute scale of second-order nonlinear-optical coefficients,” *J. Opt.*

Soc. Am. B, vol. 14, no. 9, pp. 17–19, 1997, doi: 10.1364/JOSAB.14.002268.

[65] W. C. Hurlbut, K. L. Vodopyanov, P. S. Kuo, M. M. Fejer, and Y. S. Lee, "Multi-photon absorption and nonlinear refraction of GaAs in the mid-infrared," *Opt. Lett.*, vol. 32, no. 6, pp. 668–670, 2006, doi: 10.1364/ol.32.000668.

[66] S. J. Madden *et al.*, "Long, low loss etched As_2S_3 chalcogenide waveguides for all-optical signal regeneration," *Opt. Express*, vol. 15, no. 22, p. 14414, 2007, doi: 10.1364/oe.15.014414.

[67] A. D. Logan *et al.*, "400%/W second harmonic conversion efficiency in 14 μm-diameter gallium phosphide-on-oxide resonators," *Opt. Express*, vol. 26, no. 26, p. 33687, 2018, doi: 10.1364/oe.26.033687.

[68] A. D. Logan *et al.*, "Triply-resonant sum frequency conversion with gallium phosphide ring resonators," *Opt. Express*, vol. 31, no. 2, p. 1516, 2023, doi: 10.1364/oe.473211.

[69] A. Lorenzo-Ruiz, C. Cornet, A. Beck, and Y. Léger, "Dual wavelength evanescent coupler for nonlinear GaP-based microdisk resonators," *OSA Contin.*, vol. 3, no. 1, p. 43, 2020, doi: 10.1364/osac.3.000043.

[70] J. Lv *et al.*, "Multi-wavelength unidirectional forward scattering properties of the arrow-shaped gallium phosphide nanoantenna," *J. Opt. Soc. Am. A*, vol. 40, no. 11, p. 2034, 2023, doi: 10.1364/josaa.496501.

[71] J. Lv *et al.*, "Optical anapole modes in gallium phosphide

nanodisk with forked slits for electric field enhancement," *Nanomaterials*, vol. 11, no. 6, p. 1490, 2021, doi: 10.3390/nano11061490.

[72] A. Martin, S. Combrié, A. de Rossi, G. Beaudoin, I. Sagnes, and F. Raineri, "Nonlinear gallium phosphide nanoscale photonics [Invited]," *Photonics Res.*, vol. 6, no. 5, p. B43, 2018, doi: 10.1364/prj.6.000b43.

[73] B. McLaughlin, D. P. Lake, M. Mitchell, and P. E. Barclay, "Nonlinear optics in gallium phosphide cavities: simultaneous second and third harmonic generation," *J. Opt. Soc. Am. B*, vol. 39, no. 7, p. 1853, 2022, doi: 10.1364/josab.455234.

[74] G. Q. Moretti, E. Cortés, S. A. Maier, A. V. Bragas, and G. Grinblat, "Engineering gallium phosphide nanostructures for efficient nonlinear photonics and enhanced spectroscopies," *Nanophotonics*, vol. 10, no. 17, pp. 4261–4271, 2021, doi: 10.1515/nanoph-2021-0388.

[75] C. Munley *et al.*, "Visible Wavelength Flatband in a Gallium Phosphide Metasurface," *ACS Photonics*, vol. 10, no. 8, pp. 2456–2460, 2023, doi: 10.1021/acsphotonics.3c00175.

[76] J. Gao, Q. Zhan, and A. M. Sarangan, "High-index low-loss gallium phosphide thin films fabricated by radio frequency magnetron sputtering," *Thin Solid Films*, vol. 519, no. 16, pp. 5424–5428, 2011, doi: 10.1016/j.tsf.2011.02.068.

[77] L. Hüttenhofer, A. Tittl, L. Kühner, E. Cortés, and S. A. Maier, "Anapole-Assisted Absorption Engineering in Arrays of Coupled Amorphous Gallium Phosphide Nanodisks," *ACS Photonics*, vol. 8, no. 5,

pp. 1469–1476, 2021, doi: 10.1021/acsphotonics.1c00238.

[78] S. Liu *et al.*, “An all-dielectric metasurface as a broadband optical frequency mixer,” *Nat. Commun.*, vol. 9, no. 1, p. 2507, Jun. 2018, doi: 10.1038/s41467-018-04944-9.

[79] S. M. Choudhury *et al.*, “Material platforms for optical metasurfaces,” *Nanophotonics*, vol. 7, no. 6, pp. 959–987, 2018, doi: 10.1515/nanoph-2017-0130.

[80] S. Rosas *et al.*, “Enhanced biochemical sensing with high- Q transmission resonances in free-standing membrane metasurfaces,” *Optica*, vol. 12, no. 2, p. 178, Feb. 2025, doi: 10.1364/OPTICA.549393.

[81] H. Liu *et al.*, “Enhanced high-harmonic generation from an all-dielectric metasurface,” *Nat. Phys.*, vol. 14, no. 10, pp. 1006–1010, 2018, doi: 10.1038/s41567-018-0233-6.

[82] E. Almeida, G. Shalem, and Y. Prior, “Subwavelength nonlinear phase control and anomalous phase matching in plasmonic metasurfaces,” *Nat. Commun.*, vol. 7, no. 1, p. 10367, Jan. 2016, doi: 10.1038/ncomms10367.

[83] X. Guo, Y. Ding, X. Chen, Y. Duan, and X. Ni, “Molding free-space light with guided wave–driven metasurfaces,” *Sci. Adv.*, vol. 6, no. 29, p. eabb4142, Jul. 2020, doi: 10.1126/sciadv.abb4142.

[84] Y. Liu, Y. Ke, H. Luo, and S. Wen, “Photonic spin Hall effect in metasurfaces: A brief review,” *Nanophotonics*, vol. 6, no. 1, pp. 51–70, 2017, doi: 10.1515/nanoph-2015-0155.

[85] A. P. Anthur *et al.*, “Continuous Wave Second Harmonic

Generation Enabled by Quasi-Bound-States in the Continuum on Gallium Phosphide Metasurfaces," *Nano Lett.*, vol. 20, no. 12, pp. 8745–8751, 2020, doi: 10.1021/acs.nanolett.0c03601.

[86] A. Shkarin *et al.*, "Nanoscopic Charge Fluctuations in a Gallium Phosphide Waveguide Measured by Single Molecules," *Phys. Rev. Lett.*, vol. 126, no. 13, p. 133602, 2021, doi: 10.1103/PhysRevLett.126.133602.

[87] K. Pantzas *et al.*, "Continuous-Wave Second-Harmonic Generation in Orientation-Patterned Gallium Phosphide Waveguides at Telecom Wavelengths," *ACS Photonics*, vol. 9, no. 6, pp. 2032–2039, 2022, doi: 10.1021/acsphotonics.2c00156.

[88] R. Camacho-Morales *et al.*, "Sum-Frequency Generation in High-Q GaP Metasurfaces Driven by Leaky-Wave Guided Modes," *Nano Lett.*, vol. 22, no. 15, pp. 6141–6148, Aug. 2022, doi: 10.1021/acs.nanolett.2c01349.

[89] V. Sultanov, T. Santiago-Cruz, and M. Chekhova, "Flat-optics generation of broadband photon pairs with tunable polarization entanglement," *Opt. Lett.*, vol. 47, no. 15, pp. 3872–3875, 2022, doi: 10.1364/OL.458133.

[90] C. Son *et al.*, "Photon pairs bi-directionally emitted from a resonant metasurface," *Nanoscale*, vol. 15, no. 6, pp. 2567–2572, 2023, doi: 10.1039/d2nr05499j.

[91] K. Schneider, P. Welter, Y. Baumgartner, H. Hahn, L. Czornomaz, and P. Seidler, "Gallium Phosphide-on-Silicon Dioxide

Photonic Devices," *J. Light. Technol.*, vol. 36, no. 14, pp. 2994–3002, 2018, doi: 10.1109/JLT.2018.2829221.

[92] M. R. Shcherbakov *et al.*, "Generation of even and odd high harmonics in resonant metasurfaces using single and multiple ultra-intense laser pulses," *Nat. Commun.*, vol. 12, no. 1, p. 4185, 2021, doi: 10.1038/s41467-021-24450-9.

[93] X. Yi, Z. Li, and Z. Liu, "Underwater optical communication performance for laser beam propagation through weak oceanic turbulence," *Appl. Opt.*, vol. 54, no. 6, p. 1273, Feb. 2015, doi: 10.1364/AO.54.001273.

[94] A. Orlandi, "Silicon Photonics - Fundamentals and Devices (Deen, M.J. and Basu, P.K.; 2012) [Book review]," *IEEE Electromagn. Compat. Mag.*, vol. 5, no. 3, pp. 42–43, 2016, doi: 10.1109/MEMC.0.7764247.

[95] A. F. Benner, M. Ignatowski, J. A. Kash, D. M. Kuchta, and M. B. Ritter, "Exploitation of optical interconnects in future server architectures," *IBM J. Res. Dev.*, vol. 49, no. 4.5, pp. 755–775, 2005, doi: 10.1147/rd.494.0755.

[96] T. Barwicz *et al.*, "Silicon photonics for compact, energy-efficient interconnects \[Invited\]," *J. Opt. Netw.*, vol. 6, no. 1, pp. 63–73, 2007, doi: 10.1364/JON.6.000063.

[97] D. A. B. Miller, "Energy consumption in optical modulators for interconnects.," *Opt. Express*, vol. 20 Suppl 2, pp. A293-308, Mar. 2012, doi: 10.1364/OE.20.00A293.

[98] Y. A. Vlasov, "Silicon CMOS-integrated nano-photonics for

computer and data communications beyond 100G," *IEEE Commun. Mag.*, vol. 50, no. 2, pp. s67–s72, 2012, doi: 10.1109/MCOM.2012.6146487.

[99] I. Young *et al.*, "Optical I/O technology for tera-scale computing," in *2009 IEEE International Solid-State Circuits Conference - Digest of Technical Papers*, 2009, pp. 468-469,469a, doi: 10.1109/ISSCC.2009.4977511.

[100] J. S. Levy, A. A. Gondarenko, M. A. Foster, A. C. Turner-Foster, A. L. Gaeta, and M. Lipson, "CMOS-compatible multiple-wavelength oscillator for on-chip optical interconnects," *Nat. Photonics*, vol. 4, pp. 37–40, 2010.

[101] N. Arora, *NETWORK-ON-CHIP: A NEW PARADIGM IN CHIP INTEGRATION*. 2012.

[102] D. Pamunuwa, J. Öberg, L.-R. Zheng, M. Millberg, A. Jantsch, and H. Tenhunen, "A study on the implementation of 2-D mesh-based networks-on-chip in the nanometre regime," *Integration*, vol. 38, no. 1, pp. 3–17, 2004, doi: https://doi.org/10.1016/j.vlsi.2004.03.005.

[103] A. E. Willner, S. Khaleghi, M. R. Chitgarha, and O. F. Yilmaz, "All-Optical Signal Processing," *J. Light. Technol.*, vol. 32, no. 4, pp. 660–680, 2014, doi: 10.1109/JLT.2013.2287219.

[104] Y. Ding *et al.*, "Generation of a 640 Gbit/s NRZ OTDM signal using a silicon microring resonator," *Opt. Express*, vol. 19, pp. 6471–6477, Mar. 2011, doi: 10.1364/OE.19.006471.

[105] Y. Liu *et al.*, "Error-free all-optical wavelength conversion at 160 gb/s using a semiconductor optical amplifier and an optical bandpass

filter," *J. Light. Technol.*, vol. 24, no. 1, pp. 230–236, 2006, doi: 10.1109/JLT.2005.861136.

[106] J. Hou, L. Chen, D. Wenchan, and X. Zhang, "40 Gb/s reconfigurable Optical logic gates based on FWM in silicon waveguide," *Opt. Express*, vol. 24, p. 2701, Feb. 2016, doi: 10.1364/OE.24.002701.

[107] K. Nozaki *et al.*, "Sub-femtojoule all-optical switching using a photonic-crystal nanocavity," *Nat. Photonics*, vol. 4, no. 7, pp. 477–483, 2010, doi: 10.1038/nphoton.2010.89.

[108] Xiaofan Zhao *et al.*, "40-Gb/s all-optical 3R regeneration with semiconductor devices," in *The 19th Annual Wireless and Optical Communications Conference (WOCC 2010)*, May 2010, pp. 1–3, doi: 10.1109/WOCC.2010.5510639.

[109] M. Xiong *et al.*, "Simultaneous RZ-OOK to NRZ-OOK and RZ-DPSK to NRZ-DPSK format conversion in a silicon microring resonator," *Opt. Express*, vol. 20, pp. 27263–27272, Dec. 2012, doi: 10.1364/OE.20.027263.

[110] A. Jolly and C. Granier, "All – optical sampling with Sagnac switches using closed pump and signal wavelengths near 1μm," *Opt. Commun.*, vol. 281, no. 14, pp. 3861–3871, 2008, doi: https://doi.org/10.1016/j.optcom.2008.03.052.

[111] Y. Fukuchi and S. Tasaki, "All-optical decision gate circuit employing cascaded quasi-phase matched lithium niobate device," in *Asia Communications and Photonics Conference and Exhibition*, 2010, pp. 174–175, doi: 10.1109/ACP.2010.5682779.

[112] H. J. S. Dorren, G. D. Khoe, and D. Lenstra, “All-optical switching of an ultrashort pulse using a semiconductor optical amplifier in a Sagnac-interferometric arrangement,” *Opt. Commun.*, vol. 205, no. 4, pp. 247–252, 2002, doi: https://doi.org/10.1016/S0030-4018(02)01380-9.

[113] T. Matsumoto, “Demonstration of laser-diode-pumped ultrafast all-optical switching in a nonlinear Sagnac interferometer,” *Electron. Lett.*, vol. 27, no. 1, pp. 75-76(1), 1991, [Online]. Available: https://digital-library.theiet.org/content/journals/10.1049/el_19910048.

[114] D. Taverner, N. G. Broderick, D. J. Richardson, R. I. Laming, and M. Ibsen, “Nonlinear self-switching and multiple gap-soliton formation in a fiber Bragg grating.,” *Opt. Lett.*, vol. 23, no. 5, pp. 328–330, Mar. 1998, doi: 10.1364/ol.23.000328.

[115] N. Broderick, D. Taverner, and D. Richardson, “Nonlinear switching in fibre Bragg gratings.,” *Opt. Express*, vol. 3, no. 11, pp. 447–453, Nov. 1998, doi: 10.1364/oe.3.000447.

[116] Y. Jeong, S. Baek, and B. Lee, “All-optical signal gating in cascaded long-period fiber gratings,” *IEEE Photonics Technol. Lett.*, vol. 12, no. 9, pp. 1216–1218, 2000, doi: 10.1109/68.874240.

[117] B. J. Eggleton, R. E. Slusher, J. B. Judkins, J. B. Stark, and A. M. Vengsarkar, “All-optical switching in long-period fiber gratings.,” *Opt. Lett.*, vol. 22, no. 12, pp. 883–885, Jun. 1997, doi: 10.1364/ol.22.000883.

[118] J. E. Heebner and R. W. Boyd, “Enhanced all-optical switching by use of a nonlinear fiber ring resonator.,” *Opt. Lett.*, vol. 24 12, pp. 847–849, 1999.

[119] Z. Yu, X. Xi, J. Ma, H. K. Tsang, C.-L. Zou, and X. Sun, "Photonic integrated circuits with bound states in the continuum," *Optica*, vol. 6, no. 10, p. 1342, Oct. 2019, doi: 10.1364/OPTICA.6.001342.

[120] R. Stockill *et al.*, "Gallium Phosphide as a Piezoelectric Platform for Quantum Optomechanics," *Phys. Rev. Lett.*, vol. 123, no. 16, p. 163602, Oct. 2019, doi: 10.1103/PhysRevLett.123.163602.

[121] R. Horváth *et al.*, "Sub-Hz Closed-Loop Electro-Optomechanical Oscillator with Gallium Phosphide Photonic Crystal Integrated on SoI Circuitry," *ACS Photonics*, vol. 10, no. 8, pp. 2540–2548, 2023, doi: 10.1021/acsphotonics.3c00074.

[122] S. Hönl, Y. Popoff, D. Caimi, A. Beccari, T. J. Kippenberg, and P. Seidler, "Microwave-to-optical conversion with a gallium phosphide photonic crystal cavity," *Nat. Commun.*, vol. 13, no. 1, p. 2065, Apr. 2022, doi: 10.1038/s41467-022-28670-5.

[123] E. Maggiolini *et al.*, "Strongly enhanced light–matter coupling of monolayer WS2 from a bound state in the continuum," *Nat. Mater.*, vol. 22, no. 8, pp. 964–969, Aug. 2023, doi: 10.1038/s41563-023-01562-9.

[124] P. Hong, L. Xu, and M. Rahmani, "Dual bound states in the continuum enhanced second harmonic generation with transition metal dichalcogenides monolayer," *Opto-Electronic Adv.*, vol. 5, no. 7, pp. 200097–200097, 2022, doi: 10.29026/oea.2022.200097.

[125] M. Churaev *et al.*, "A heterogeneously integrated lithium niobate-on-silicon nitride photonic platform," *Nat. Commun.*, vol. 14, no. 1, p. 3499, Jun. 2023, doi: 10.1038/s41467-023-39047-7.

[126] N. Ding *et al.*, “Engineering extinction ratio towards higher-efficiency four-wave mixing process in GaP-OI microresonators,” *Opt. Express*, vol. 33, no. 26, p. 54022, Dec. 2025, doi: 10.1364/OE.580755.

[127] M. Sheik-Bahae, A. A. Said, T.-H. Wei, D. J. Hagan, and E. W. Van Stryland, “Sensitive measurement of optical nonlinearities using a single beam,” *IEEE J. Quantum Electron.*, vol. 26, no. 4, pp. 760–769, 1990, doi: 10.1109/3.53394.

[128] M. Sheik-Bahae, J. Wang, R. Desalvo, D. J. Hagan, and E. W. Stryland, “Measurement of nondegenerate nonlinearities using a two-color Z scan.,” *Opt. Lett.*, vol. 17, no. 4, pp. 258–260, Feb. 1992, doi: 10.1364/ol.17.000258.

[129] M. Taghinejad and W. Cai, “All-Optical Control of Light in Micro- and Nanophotonics,” *ACS Photonics*, vol. 6, no. 5, pp. 1082–1093, 2019, doi: 10.1021/acsphotonics.9b00013.

[130] J. S. Pelc, K. Rivoire, S. Vo, C. Santori, D. A. Fattal, and R. G. Beausoleil, “Picosecond all-optical switching in hydrogenated amorphous silicon microring resonators,” *Opt. Express*, vol. 22, no. 4, p. 3797, 2014, doi: 10.1364/oe.22.003797.

[131] P. Sethi and S. Roy, “All-optical ultrafast switching in 2 × 2 silicon microring resonators and its application to reconfigurable DEMUX/MUX and reversible logic gates,” *J. Light. Technol.*, vol. 32, no. 12, pp. 2173–2180, 2014, doi: 10.1109/JLT.2014.2315670.

[132] M. R. Shcherbakov *et al.*, “Ultrafast All-Optical Switching with Magnetic Resonances in Nonlinear Dielectric Nanostructures,” *Nano Lett.*,

vol. 15, no. 10, pp. 6985–6990, 2015, doi: 10.1021/acs.nanolett.5b02989.

[133] Z. Chai *et al.*, "Ultrafast on-Chip Remotely-Triggered All-Optical Switching Based on Epsilon-Near-Zero Nanocomposites," *Laser Photon. Rev.*, vol. 11, no. 5, p. 1700042, Sep. 2017, doi: 10.1002/lpor.201700042.

[134] G. Grinblat, R. Berté, M. P. Nielsen, Y. Li, R. F. Oulton, and S. A. Maier, "Sub-20 fs All-Optical Switching in a Single Au-Clad Si Nanodisk," *Nano Lett.*, vol. 18, no. 12, pp. 7896–7900, 2018, doi: 10.1021/acs.nanolett.8b03770.

[135] M. Ono *et al.*, "Ultrafast and energy-efficient all-optical switching with graphene-loaded deep-subwavelength plasmonic waveguides," *Nat. Photonics*, vol. 14, no. 1, pp. 37–43, Jan. 2020, doi: 10.1038/s41566-019-0547-7.

[136] L. Li *et al.*, "Ultrafast All-Optical Switching in the Visible Spectrum with 6H Silicon Carbide," *ACS Photonics*, vol. 8, no. 10, pp. 2940–2946, Oct. 2021, doi: 10.1021/acsphotonics.1c00605.

[137] Y. Jung, H. Han, A. Sharma, J. Jeong, S. S. P. Parkin, and J. K. S. Poon, "Integrated Hybrid VO 2 –Silicon Optical Memory," *ACS Photonics*, vol. 9, no. 1, pp. 217–223, Jan. 2022, doi: 10.1021/acsphotonics.1c01410.

[138] Q. Guo *et al.*, "Femtojoule femtosecond all-optical switching in lithium niobate nanophotonics," *Nat. Photonics*, vol. 16, no. 9, pp. 625–631, Sep. 2022, doi: 10.1038/s41566-022-01044-5.

[139] C. J. Sarabalis *et al.*, "Acousto-optic modulation of a

wavelength-scale waveguide," *Optica*, vol. 8, no. 4, p. 477, Apr. 2021, doi: 10.1364/OPTICA.413401.

[140] S. Xu, W. Liu, X. Le, and C. Lee, "Unveiling Efficient Acousto-Optic Modulation in Silicon Photonic Devices via Lithium Niobate Using Transfer Printing," *Nano Lett.*, vol. 24, no. 41, pp. 12964–12972, Sep. 2024, doi: 10.1021/acs.nanolett.4c03622.

[141] H. D. Boggiano, R. Berté, A. F. Scarpettini, E. Cortés, S. A. Maier, and A. V. Bragas, "Determination of Nanoscale Mechanical Properties of Polymers via Plasmonic Nanoantennas," *ACS Photonics*, vol. 7, no. 6, pp. 1403–1409, Jun. 2020, doi: 10.1021/acsphotonics.0c00631.

[142] K. Yu, J. E. Sader, P. Zijlstra, M. Hong, Q.-H. Xu, and M. Orrit, "Probing Silver Deposition on Single Gold Nanorods by Their Acoustic Vibrations," *Nano Lett.*, vol. 14, no. 2, pp. 915–922, Feb. 2014, doi: 10.1021/nl404304h.

[143] K. J. Satzinger *et al.*, "Quantum control of surface acoustic-wave phonons," *Nature*, vol. 563, no. 7733, pp. 661–665, Nov. 2018, doi: 10.1038/s41586-018-0719-5.

[144] H. D. Boggiano *et al.*, "Coherent Acoustic Phonons in Plasmonic Nanoparticles: Elastic Properties and Dissipation at Low Temperatures," *ACS Nano*, vol. 18, no. 46, pp. 31903–31911, Nov. 2024, doi: 10.1021/acsnano.4c09193.

[145] R. Berte *et al.*, "Acoustic Far-Field Hypersonic Surface Wave Detection with Single Plasmonic Nanoantennas," *Phys. Rev. Lett.*, vol. 121, no. 25, p. 253902, Dec. 2018, doi: 10.1103/PhysRevLett.121.253902.

[146] K. Yu and G. P. Wang, “Coherent Acoustic Vibrational Spectrum of Single and Coupled Nanoresonators,” *J. Phys. Chem. C*, vol. 128, no. 13, pp. 5394–5407, 2024, doi: 10.1021/acs.jpcc.4c00256.

[147] J. Zhang, K. Yu, and G. P. Wang, “Coherent Acoustic Phonon Dynamics and Coupling in Metal-van der Waals Heterostructure Nanocavities,” *ACS Nano*, vol. 19, no. 10, pp. 10093–10102, Mar. 2025, doi: 10.1021/acsnano.4c16912.

[148] Y. Imade, V. E. Gusev, O. Matsuda, M. Tomoda, P. H. Otsuka, and O. B. Wright, “Gigahertz Optomechanical Photon-Phonon Transduction between Nanostructure Lines,” *Nano Lett.*, vol. 21, no. 14, pp. 6261–6267, 2021, doi: 10.1021/acs.nanolett.1c02070.

[149] M. Poblet *et al.*, “Acoustic Coupling between Plasmonic Nanoantennas: Detection and Directionality of Surface Acoustic Waves,” *ACS Photonics*, vol. 8, no. 10, pp. 2846–2852, 2021, doi: 10.1021/acsphotonics.1c00741.

[150] A. V. Bragas *et al.*, “Nanomechanics with plasmonic nanoantennas: ultrafast and local exchange between electromagnetic and mechanical energy,” *J. Opt. Soc. Am. B*, vol. 40, no. 5, p. 1196, May 2023, doi: 10.1364/JOSAB.482384.

[151] H. D. Boggiano, L. Nan, G. Grinblat, S. A. Maier, E. Cortés, and A. V. Bragas, “Focusing Surface Acoustic Waves with a Plasmonic Hypersonic Lens,” *Nano Lett.*, vol. 24, no. 21, pp. 6362–6368, May 2024, doi: 10.1021/acs.nanolett.4c01251.

[152] F. Della Picca *et al.*, “Tailored Hypersound Generation in

Single Plasmonic Nanoantennas," *Nano Lett.*, vol. 16, no. 2, pp. 1428–1434, Feb. 2016, doi: 10.1021/acs.nanolett.5b04991.

[153] A. Crut, P. Maioli, N. Del Fatti, and F. Vallée, "Acoustic vibrations of metal nano-objects: Time-domain investigations," *Phys. Rep.*, vol. 549, pp. 1–43, Jan. 2015, doi: 10.1016/j.physrep.2014.09.004.

[154] M. S. Kirschner, X.-M. Lin, L. X. Chen, and R. D. Schaller, "Phase control of coherent acoustic phonons in gold bipyramids for optical memory and manipulating plasmon–exciton coupling," *Appl. Phys. Lett.*, vol. 116, no. 15, p. 153102, Apr. 2020, doi: 10.1063/5.0004209.

[155] K. O'Brien, N. D. Lanzillotti-Kimura, J. Rho, H. Suchowski, X. Yin, and X. Zhang, "Ultrafast acousto-plasmonic control and sensing in complex nanostructures," *Nat. Commun.*, vol. 5, no. 1, p. 4042, Jun. 2014, doi: 10.1038/ncomms5042.

[156] F. Medeghini *et al.*, "Controlling the Quality Factor of a Single Acoustic Nanoresonator by Tuning its Morphology," *Nano Lett.*, vol. 18, no. 8, pp. 5159–5166, 2018, doi: 10.1021/acs.nanolett.8b02096.

[157] M. Pelton, J. E. Sader, J. Burgin, M. Liu, P. Guyot-Sionnest, and D. Gosztola, "Damping of acoustic vibrations in gold nanoparticles," *Nat. Nanotechnol.*, vol. 4, no. 8, pp. 492–495, 2009, doi: 10.1038/nnano.2009.192.

[158] K. Yu, P. Zijlstra, J. E. Sader, Q. H. Xu, and M. Orrit, "Damping of acoustic vibrations of immobilized single gold nanorods in different environments," *Nano Lett.*, vol. 13, no. 6, pp. 2710–2716, 2013, doi: 10.1021/nl400876w.

[159] L. Wang, S. Takeda, R. Sato, M. Sakamoto, T. Teranishi, and N. Tamai, “Morphology-Dependent Coherent Acoustic Phonon Vibrations and Phonon Beat of Au Nanopolyhedrons,” *ACS Omega*, vol. 6, no. 8, pp. 5485–5489, 2021, doi: 10.1021/acsomega.0c05806.

[160] M. N. Su *et al.*, “Optomechanics of Single Aluminum Nanodisks,” *Nano Lett.*, vol. 17, no. 4, pp. 2575–2583, 2017, doi: 10.1021/acs.nanolett.7b00333.

[161] M.-N. Su *et al.*, “Ultrafast Electron Dynamics in Single Aluminum Nanostructures,” *Nano Lett.*, vol. 19, no. 5, pp. 3091–3097, May 2019, doi: 10.1021/acs.nanolett.9b00503.

[162] Y. Cheng *et al.*, “Size- And Surface-Dependent Photoresponses of Solution-Processed Aluminum Nanoparticles,” *ACS Photonics*, vol. 7, no. 3, pp. 637–645, 2020, doi: 10.1021/acsphotonics.9b01170.

[163] M. Hu, H. Petrova, X. Wang, and G. V. Hartland, “Time-Resolved and Steady State Spectroscopy of Polydisperse Colloidal Silver Nanoparticle Samples,” *J. Phys. Chem. B*, vol. 109, no. 30, pp. 14426–14432, Aug. 2005, doi: 10.1021/jp0516238.

[164] H. Staleva and G. V. Hartland, “Vibrational Dynamics of Silver Nanocubes and Nanowires Studied by Single-Particle Transient Absorption Spectroscopy,” *Adv. Funct. Mater.*, vol. 18, no. 23, pp. 3809–3817, Dec. 2008, doi: 10.1002/adfm.200800605.

[165] C. Jean *et al.*, “Spatiotemporal Imaging of the Acoustic Field Emitted by a Single Copper Nanowire,” *Nano Lett.*, vol. 16, no. 10, pp. 6592–6598, 2016, doi: 10.1021/acs.nanolett.6b03260.

[166] C. Yi *et al.*, "Polycrystallinity of Lithographically Fabricated Plasmonic Nanostructures Dominates Their Acoustic Vibrational Damping," *Nano Lett.*, vol. 18, no. 6, pp. 3494–3501, 2018, doi: 10.1021/acs.nanolett.8b00559.

[167] B. Ostovar *et al.*, "Acoustic Vibrations of Al Nanocrystals: Size, Shape, and Crystallinity Revealed by Single-Particle Transient Extinction Spectroscopy," *J. Phys. Chem. A*, vol. 124, no. 19, pp. 3924–3934, 2020, doi: 10.1021/acs.jpca.0c01190.

[168] M. Pelton, D. Chakraborty, E. Malachosky, P. Guyot-Sionnest, and J. E. Sader, "Viscoelastic Flows in Simple Liquids Generated by Vibrating Nanostructures," *Phys. Rev. Lett.*, vol. 111, no. 24, p. 244502, Dec. 2013, doi: 10.1103/PhysRevLett.111.244502.

[169] W.-S. Chang *et al.*, "Tuning the acoustic frequency of a gold nanodisk through its adhesion layer," *Nat. Commun.*, vol. 6, no. 1, p. 7022, May 2015, doi: 10.1038/ncomms8022.

[170] K. Yu, T. Devkota, G. Beane, G. P. Wang, and G. V. Hartland, "Brillouin Oscillations from Single Au Nanoplate Opto-Acoustic Transducers," *ACS Nano*, vol. 11, no. 8, pp. 8064–8071, 2017, doi: 10.1021/acsnano.7b02703.

[171] R. Gao *et al.*, "Gigahertz optoacoustic vibration in Sub-5 nm tip-supported nano-optomechanical metasurface," *Nat. Commun.*, vol. 14, no. 1, p. 485, Jan. 2023, doi: 10.1038/s41467-023-36127-6.

[172] N. Gross *et al.*, "Strong Substrate Binding Modulates the Acoustic Quality Factors in Gold Nanodisks," *J. Phys. Chem. C*, vol. 127,

no. 10, pp. 5054–5066, 2023, doi: 10.1021/acs.jpcc.2c09099.

[173] M. N. Su, B. Ostovar, N. Gross, J. E. Sader, W. S. Chang, and S. Link, “Acoustic Vibrations and Energy Dissipation Mechanisms for Lithographically Fabricated Plasmonic Nanostructures Revealed by Single-Particle Transient Extinction Spectroscopy,” *J. Phys. Chem. C*, vol. 125, no. 3, pp. 1621–1636, 2021, doi: 10.1021/acs.jpcc.0c09782.

[174] Y. Yan, T. Zhu, Q. Zhao, R. Berté, and Y. Li, “Launching directional hypersonic surface waves in monolithic gallium phosphide nanodisks: two holes are better than one,” *Nanoscale*, vol. 15, no. 7, pp. 3318–3325, 2023, doi: 10.1039/D2NR05729H.

[175] I. A. Ajia *et al.*, “Gigahertz Nano-Optomechanical Resonances in a Dielectric SiC-Membrane Metasurface Array,” *Nano Lett.*, vol. 21, no. 11, pp. 4563–4569, 2021, doi: 10.1021/acs.nanolett.1c00205.

[176] H. D. Boggiano *et al.*, “All-Optical Generation and Detection of Coherent Acoustic Vibrations in Single Gallium Phosphide Nanoantennas Probed near the Anapole Excitation,” *Nano Lett.*, vol. 25, no. 4, pp. 1351–1357, Jan. 2025, doi: 10.1021/acs.nanolett.4c04907.

[177] F. Noll, N. Krauß, V. Gusev, T. Dekorsy, and M. Hettich, “Surface plasmon-based detection for picosecond ultrasonics in planar gold-dielectric layer geometries,” *Photoacoustics*, vol. 30, 2023, doi: 10.1016/j.pacs.2023.100464.

[178] C. Wright and G. V. Hartland, “Mode specific dynamics for the acoustic vibrations of a gold nanoplate,” *Photoacoustics*, vol. 30, p. 100476, 2023, doi: 10.1016/j.pacs.2023.100476.

[179] R. Delalande, L. Burr, E. Charron, M. Jouini, M. E. Toimil-Molares, and L. Belliard, "Vibrational response of Au-Ag alloy and porous Au single nanowires probed by ultrafast pump-probe spectroscopy," *Appl. Phys. Lett.*, vol. 115, no. 8, p. 083103, Aug. 2019, doi: 10.1063/1.5108772.

[180] H. Staleva *et al.*, "Nanophotonics: Plasmonics and metal nanoparticles," *Phys. Chem. Chem. Phys.*, vol. 11, no. 28, pp. 5866–5866, 2009, doi: 10.1039/b911746f.

[181] L. Belliard *et al.*, "Vibrational response of free standing single copper nanowire through transient reflectivity microscopy," *J. Appl. Phys.*, vol. 114, no. 19, 2013, doi: 10.1063/1.4831957.

[182] F. Döring *et al.*, "Confinement of phonon propagation in laser deposited tungsten/polycarbonate multilayers," *New J. Phys.*, vol. 18, no. 9, p. 092002, Sep. 2016, doi: 10.1088/1367-2630/18/9/092002.

[183] J. D. G. Greener *et al.*, "High-Frequency Elastic Coupling at the Interface of van der Waals Nanolayers Imaged by Picosecond Ultrasonics," *ACS Nano*, vol. 13, no. 10, pp. 11530–11537, 2019, doi: 10.1021/acsnano.9b05052.

[184] D. Nardi *et al.*, "Probing thermomechanics at the nanoscale: Impulsively excited pseudosurface acoustic waves in hypersonic phononic crystals," *Nano Lett.*, vol. 11, no. 10, pp. 4126–4133, 2011, doi: 10.1021/nl201863n.

[185] A. Khanolkar, S. Wallen, M. Abi Ghanem, J. Jenks, N. Vogel, and N. Boechler, "A self-assembled metamaterial for Lamb waves," *Appl. Phys. Lett.*, vol. 107, no. 7, 2015, doi: 10.1063/1.4928564.

[186] A. Bruchhausen *et al.*, "Subharmonic Resonant Optical Excitation of Confined Acoustic Modes in a Free-Standing Semiconductor Membrane at GHz Frequencies with a High-Repetition-Rate Femtosecond Laser," *Phys. Rev. Lett.*, vol. 106, no. 7, p. 077401, Feb. 2011, doi: 10.1103/PhysRevLett.106.077401.

[187] S. Zanotto *et al.*, "Optomechanics of Chiral Dielectric Metasurfaces," *Adv. Opt. Mater.*, vol. 8, no. 4, p. 1901507, Feb. 2020, doi: 10.1002/adom.201901507.

[188] A. Pitanti, G. Da Prato, G. Biasiol, A. Tredicucci, and S. Zanotto, "Gigahertz Modulation of a Fully Dielectric Nonlocal Metasurface," *Adv. Opt. Mater.*, vol. 12, no. 36, p. 2401283, Dec. 2024, doi: 10.1002/adom.202401283.

[189] Y. Cang, Y. Jin, B. Djafari-Rouhani, and G. Fytas, "Fundamentals, progress and perspectives on high-frequency phononic crystals," *J. Phys. D. Appl. Phys.*, vol. 55, no. 19, 2022, doi: 10.1088/1361-6463/ac4941.

[190] R. C. Ng *et al.*, "Excitation and detection of acoustic phonons in nanoscale systems," *Nanoscale*, vol. 14, no. 37, pp. 13428–13451, 2022, doi: 10.1039/d2nr04100f.

[191] Z. Wang, K. Yao, M. Chen, H. Chen, and Y. Liu, "Manipulating Smith-Purcell Emission with Babinet Metasurfaces," *Phys. Rev. Lett.*, vol. 117, no. 15, p. 157401, Oct. 2016, doi: 10.1103/PhysRevLett.117.157401.

[192] Y. Chen, X. Yang, and J. Gao, "Spin-Selective Second-Harmonic Vortex Beam Generation with Babinet-Inverted Plasmonic

Metasurfaces," *Adv. Opt. Mater.*, vol. 6, no. 19, p. 1800646, Oct. 2018, doi: 10.1002/adom.201800646.

[193] M. Hentschel, T. Weiss, S. Bagheri, and H. Giessen, "Babinet to the half: Coupling of solid and inverse plasmonic structures," *Nano Lett.*, vol. 13, no. 9, pp. 4428–4433, 2013, doi: 10.1021/nl402269h.

[194] B. H.G., "Slot aerials and their relation to complementary wire aerials (Babinet's principle)," *J. Inst. Electr. Eng. - Part IIIA Radiolocation*, vol. 93, no. 4, pp. 620–626, Jan. 1946, doi: 10.1049/ji-3a-1.1946.0150.

[195] F. Falcone *et al.*, "Babinet Principle Applied to the Design of Metasurfaces and Metamaterials," *Phys. Rev. Lett.*, vol. 93, no. 19, p. 197401, Nov. 2004, doi: 10.1103/PhysRevLett.93.197401.

[196] J. Kim *et al.*, "Babinet-inverted optical Yagi-Uda antenna for unidirectional radiation to free space," *Nano Lett.*, vol. 14, no. 6, pp. 3072–3078, 2014, doi: 10.1021/nl500062f.

[197] J. D. Ortiz, J. P. del Risco, J. D. Baena, and R. Marqués, "Extension of Babinet's principle for plasmonic metasurfaces," *Appl. Phys. Lett.*, vol. 119, no. 16, p. 161103, Oct. 2021, doi: 10.1063/5.0065724.

[198] V. Dichtl, T. Schumacher, and M. Lippitz, "The Nonlinear Limit of Babinet's Principle," *Nano Lett.*, vol. 25, no. 28, pp. 11084–11088, Jul. 2025, doi: 10.1021/acs.nanolett.5c02210.

[199] D. E. Aspnes and A. A. Studna, "Dielectric functions and optical parameters of Si, Ge, GaP, GaAs, GaSb, InP, InAs, and InSb from 1.5 to 6.0 eV," *Phys. Rev. B*, vol. 27, no. 2, pp. 985–1009, Jan. 1983, doi:

10.1103/PhysRevB.27.985.

[200] J. Lermé, J. Margueritat, and A. Crut, “Vibrations of Dimers of Mechanically Coupled Nanostructures: Analytical and Numerical Modeling,” *J. Phys. Chem. C*, vol. 125, no. 15, pp. 8339–8348, 2021, doi: 10.1021/acs.jpcc.1c01425.

[201] Y. Wang *et al.*, “A review of gallium phosphide nanophotonics towards omnipotent nonlinear devices,” *Nanophotonics*, vol. 13, no. 18, pp. 3207–3252, Aug. 2024, doi: 10.1515/nanoph-2024-0172.

[202] T. A. Major, S. S. Lo, K. Yu, and G. V. Hartland, “Time-resolved studies of the acoustic vibrational modes of metal and semiconductor nano-objects,” *J. Phys. Chem. Lett.*, vol. 5, no. 5, pp. 866–874, 2014, doi: 10.1021/jz4027248.

[203] H. D. Boggiano *et al.*, “Optical Readout of the Mechanical Properties of Silica Mesoporous Thin Films Using Plasmonic Nanoantennas,” *ACS Photonics*, vol. 10, no. 11, pp. 3998–4005, 2023, doi: 10.1021/acsphotonics.3c00874.